



University
of Stavanger

Faculty of Science
and Technology

MASTER'S THESIS

| | |
|--|-----------------------------|
| Study program / Specialization: Offshore Technology Marine and Subsea Technology | Spring semester, 2016 |
| Writer: Mamikon Pogosov | Writer's signature |
| Faculty supervisors: professor Muk Chen Ong (University of Stavanger), External supervisor: professor Anatoly B. Zolotukhin (Gubkin University) | |
| Title of Thesis Computational Fluid Dynamics of Flow around Tandem Cylinders close to the Seabed | |
| Credits (ECTS): 30 | |
| Key Words: CFD, cylinder, tandem cylinders, vortex, upper-transition regime | Pages: 103 |
| Stavanger, 2016 | |

Abstract.

CFD is a useful tool for understanding continuum mechanics and analyzing flows, both disturbed and undisturbed. When we analyze flow around cylinders with CFD, we can get numerical results. We have the opportunity to see how the flow actually will distribute around cylinders. Pressure and Velocity can be obtained and measured in all points of the simulation field and the valid forces imposed on the cylinder can be obtained too. Computational Fluid Dynamics is cheaper and accessible to get results than doing experiments CFD simulation is also cheaper than making tests, and at present, CFD can substitute or enhance many experiments. On streamlined over sea or river underwater pipeline affect the horizontal force of viscous resistance, which is proportional to the square of the flow rate.

Of course, this configuration and analysis of a cylinder with a subsequent analysis of the two, taken with an ulterior motive. Most probably a good example of a joint international project "Nord Stream" and "Nord Stream-2". The first project is a branch of gas pipeline laid on the bottom of the Baltic Sea. The second, in turn, will be the second branch of the main gas pipeline, which will run in tandem with the first. In other words, the relevance of this issue is in demand, especially when it comes to a marine pipeline, with energy consumption increasing, and therefore requires payment and the amount of product are being pumped. Just offshore field development infrastructure is not in place and is developing dynamically. Due to the daily production of gas, there is growing demand for the expansion of the oil and gas transportation. Subsea pipelines, get the constant influence of regular and irregular waves due to the influence of underwater currents in certain areas. Depending on the nature of the flow, it can

influence the vortex formation, which can erode the soil directly beneath the pipe and because of this certain parts of the pipeline can be formed free-spans. They can occur during the vortex formation and as a consequence of vortex induced vibrations. To prevent such situations and the effects of the design of pipelines, it is necessary to simulate the flow around the planned pipeline.

In this paper, calculated the flow impact on a subsea pipeline, which is associated with the formation of internal waves in a stratified flow based on the results of simulation models, which made in OpenFOAM software.

The present study has been done for both the single cylinder and the tandem cylinder arrangements scenarios. All simulation model is evaluated for a steady flow with the parameters such as Reynolds number $Re = 3.6 \times 10^6$, a roughness of the plane bottom and cylinder's surface $z_w = 1 \times 10^{-6}$ and boundary layer thickness $\delta/D = 0.5$.

The pre-processing software as GMESH was used to perform all grids for the CFD simulation model. Also, a size of the computational domains arrangements of the single case cylinder and the tandem cylinders case has been accomplished in this software. Tecplot360 was chosen in the post-processing step to get visualization for all cases, and to plot graphs; two programs were used such as Wolfram Matematica 10.0 and Matlab.

By using the supercomputers Gorina1 and Gorina 2 at UIS, It is possible to get a model of the flow around the tandem cylinder, which would be impossible with a personal computer.

Content.

| | |
|--|-----------|
| List of Abbreviations..... | 9 |
| List Of Symbols | 10 |
| Introduction. | 13 |
| Chapter 1 | |
| Theory | 14 |
| 1.2 Flow regime | 14 |
| 1.2 Vortex shedding..... | 15 |
| 1.3 Vortex shedding frequency | 17 |
| 1.4 Forces acting on a cylinder | 18 |
| 1.5 Force coefficients..... | 19 |
| 1.6 Interference regions..... | 20 |
| 1.7 Flow pattern | 22 |
| 1.8 Pressure distributions and fluctuations | 24 |
| Outline of the thesis..... | 29 |
| Chapter 2 | |
| 2.1 OpenFOAM..... | 31 |
| 2.2 Courant number..... | 33 |
| 2.3 Turbulence..... | 33 |
| 2.4 RANS | 34 |
| 2.5 k - ϵ model | 35 |
| 2.6 Characteristics of the flow around a circular cylinder near a plane boundary..... | 36 |
| Chapter 3 | |
| Computational Fluid Dynamics..... | 43 |
| 3.1 Introduction..... | 43 |
| 3.2 Mathematical formulation and Standard High Reynolds number κ - ϵ Model. | 43 |
| 3.4 Mesh..... | 44 |
| Chapter 4 | |
| Numerical setup | 47 |
| 4.1 Numerical solution procedure, computational domain and boundary conditions | 47 |
| 4.2 Convergence studies | 52 |
| 4.3 Results and discussion..... | 55 |
| 4.4 Vorticity contours. | 61 |
| 4.5 Streamlines | 65 |
| Chapter 5 | |
| Conclusion for flow around the single cylinder. | 68 |

Chapter 6

| | |
|--|-----------|
| Numerical set-up | 70 |
| 6.1 Numerical solution procedure, computational domain and boundary conditions | 70 |
| 6.2 Mesh | 73 |
| 6.3 Convergence studies | 78 |

Chapter 7

| | |
|---------------------------------|----|
| 7.1 Results and discussion..... | 83 |
| 7.2 Vorticity contours. | 91 |
| 7.6 Streamlines | 95 |

Chapter 8

| | |
|--|-----|
| 8.1 Conclusion for the tandem cylinders case | 99 |
| 8.2 Recommendations for Further Work..... | 100 |

| | |
|-------------------------|------------|
| References | 102 |
|-------------------------|------------|

List of Figures

| | |
|---|-----------|
| Figure 1.1: <i>Regimes of flow around a smooth, circular cylinder in steady current</i> | 15 |
| Figure 1.2: <i>The shear layers on both sides roll up to form the lee-wake vortices, vortices</i> | 16 |
| Figure 1.3: <i>The alternative manner of the vortex shedding</i> | 17 |
| Figure 1.4 <i>Drag and lift traces obtained from the measured pressure distributions</i> | 19 |
| Figure 1.5 <i>Regions of interference around a circular cylinder.</i> | 20 |
| Figure 1.6. <i>Critical spacing between two tandem cylinders and vortex formation length for a single cylinder as a function of Reynolds number.</i> | 21 |
| Figure 1.7. <i>Classification of flow patterns for different spacings and Reynolds numbers</i> | 22 |
| Figure 1.8. <i>Different flow patterns for tandem cylinders</i> | 23 |
| Figure 1.9. <i>Pressure distribution at different Re numbers for a smooth cylinder</i> | 25 |
| Figure 1.10: <i>Pressure distribution around tandem cylinders.</i> | 27 |
| Figure 1.11. <i>Pressure fluctuations around tandem cylinders.</i> | 28 |
| Figure 2.1 <i>Structure of OpenFOAM</i> | 32 |
| Figure 2.2. <i>Sketch of the flow geometry for a cylinder close to the seabed</i> | 36 |
| Figure 2.3 <i>Developing boundary layer on a horizontal plate</i> | 39 |
| Figure 2.4. <i>Non-dimensional velocity distribution near a smooth wall</i> | 42 |
| Figure 3.1 <i>Structured and unstructured quadrilateral grid</i> | 45 |
| Figure 4.1 <i>Determination sketch for flow around a circular cylinder close to the plane wall</i> | 48 |
| Figure 4.2 <i>Mesh close to a wall with illustration of h_p</i> | 50 |
| Figure 4.3 <i>Global mesh for a single cylinder case at $G/D = 1$</i> | 51 |
| Figures 4.4 <i>Transaction between geometries elements</i> | 51 |
| Figure 4.5 <i>Local mesh for single cylinder case</i> | 52 |
| Figure 4.6 <i>Grid convergence for C_D and C_L with respect to the number of elements in the computational domain for $Re = 3.6 \times 10^6$ with $\delta/D = 0.5$ and $z_w = 1 \times 10^{-6}$</i> | 53 |
| Figure 4.7. <i>Time-averaged drag coefficient versus gap-to-diameter ratio</i> | 56 |
| Figure 4.8. <i>Time-averaged lift coefficient versus gap-to-diameter ratio</i> | 57 |
| Figure 4.9. <i>Srouhal number versus gap-to-diameter ratio</i> | 58 |
| Figure 4.10 <i>Mean pressure coefficient around the cylinder body $G/D = 1$</i> | 59 |
| Figure 4.11 <i>Mean pressure coefficient around the cylinder body $G/D = 1$</i> | 59 |
| Figure 4.12 <i>Mean pressure coefficient around the cylinder body $G/D = 0.8$</i> | 60 |
| Figure 4.13 <i>Mean pressure coefficients around the cylinder for $Re = 3.6 \times 10^6$ with $\delta/D = 0.5$ for $z_w = 1 \times 10^{-6}$ and $G/D = (0.5; 0.8; 1)$</i> | 61 |
| Figure 4.14. <i>The development of vortex shedding shown by instantaneous non-dimensional vorticity counter plots for $Re = 3.6 \times 10^6$, $\delta/D = 0.5$ for $z_w = 1 \times 10^{-6}$ at non-dimensional time of $200D/U_\infty$</i> | 64 |
| Figure 4.15. <i>Schematic overview of mean flows structure for a case $G/D = 1$</i> | 65 |
| Figure 4.16. <i>Symmetry in vortices around cylinder for $G/D = 1$</i> | 66 |
| Figure 4.17. <i>Instantaneous streamlines at $200D/U_\infty$ for circular cylinder with gap-to-diameter ratios $G/D = 0.5; 0.8; 1$</i> | 68 |
| Figure 6.1. <i>Definition sketch for the tandem cylinders in the vicinity of a plane wall; in the present study $L/D = 2, 3, 3.5$; $G/D = 1, 0.8, 0.5$</i> | 71 |
| Figure 6.2. <i>Meshes for cases with $G/D = 1$.</i> | 74 |
| Figure 6.3. <i>Meshes for cases with $G/D = 0.8$.</i> | 75 |

| | |
|---|-----------|
| Figure 6.4. <i>Demonstration of an additional line on example of case $L/D=3$</i> | 76 |
| Figure 6.6. <i>Global mesh for a single cylinder case at $G/D=0.5$ and $L/D=3$</i> | 77 |
| Figure 6.7. <i>Local mesh for tandem cylinders at $G/D=0.5$ and $L/D=3$</i> | 77 |
| Figure 6.8 <i>Meshes for cases with $G/D = 0.5$</i> | 78 |
| Figure 6.9. <i>The grid convergence study $G/D = 1, L/D = (2; 3; 3.5)$</i> | 80 |
| Figure 6.10. <i>The grid convergence study $G/D = 0.8, L/D = (2; 3; 3.5)$</i> | 80 |
| Figure 6.11. <i>The grid convergence study $G/D = 0.5, L/D = (2; 3; 3.5)$</i> | 81 |
| Figure 7.1 <i>Time-averaged drag coefficients versus G/D and L/D</i> | 84 |
| Figure 7.2 <i>Time-averaged lift coefficients versus G/D and L/D</i> | 85 |
| Figure 7.3 <i>Time-averaged Strouhal numbers versus G/D and L/D</i> | 87 |
| Figure 7.4 <i>Mean pressure coefficients around the tandem cylinders at $G/D = 1$</i> | 88 |
| Figure 7.5 <i>Mean pressure coefficients around the tandem cylinders at $G/D = 0.8$</i> | 89 |
| Figure 7.6. <i>Mean pressure coefficients around the tandem cylinders at $G/D = 0.5$</i> | 90 |
| Figure 7.8. <i>Instantaneous vorticity contours for $G/D = 1.5$</i> | 92 |
| Figure 7.9. <i>Instantaneous vorticity contours for $G/D = 0.8$</i> | 93 |
| Figure 7.10. <i>Instantaneous vorticity contours for $G/D = 0.5$</i> | 94 |
| Figure 7.11. <i>Instantaneous streamlines for $G/D = 1$</i> | 96 |
| Figure 7.12. <i>Instantaneous streamlines for $G/D = 0.8$</i> | 97 |
| Figure 7.13. <i>Instantaneous streamlines for $G/D = 0.5$</i> | 98 |

List of tables

| | |
|---|-----------|
| Table 1. Results from grid covergence study for circular cylinder with gap-to-diameter ratio [0.5; 0.8; 1]..... | 54 |
| Table 2. Numerical results and experimental data at $Re = 3.6 \times 10^6$ | 56 |
| Table 3. Results from grid covergence study for the tandem cylinders with gap-to-diameter ratios [0.5; 0.8; 1] and pitch distance [1; 2; 2.5]..... | 82 |

List of Abbreviations

| | |
|--------|--|
| 2D: | Two dimensional |
| CFD: | Computational Fluid Dynamics |
| DNS: | Direct Numerical Simulation |
| PISO: | Pressure Implicit with Splitting Operators |
| RANS: | Reynolds-Averaged Navier-Stokes |
| URANS: | Unsteady Reynolds-averaged Navier-Stokes |
| RMS: | Root mean square |
| LES: | Large Eddy Simulation |
| DNS: | Direct Numerical Simulation |
| DES: | Detached Eddie Simulation |

List Of Symbols

| | |
|------------------------|--|
| δ_{ij} : | Kronecker delta |
| ε : | Rate of turbulent kinetic energy |
| κ : | von Karmans constant |
| μ : | Dynamic viscosity |
| ν : | Kinematic viscosity |
| ν_t : | Turbulent viscosity of fluid |
| ω : | Instantaneous vorticity |
| φ : | Angular coordinate |
| ρ : | Density of fluid |
| σ_k : | Turbulent Prandtl number for kinetic energy |
| σ_ε : | Turbulent Prandtl number for dissipation |
| τ_{ij} : | Stress tensor |
| τ_ω : | Wall shear stress |
| C_D : | Drag coefficient |
| $\overline{C_D}$: | Mean drag coefficient |
| C_L : | Instantaneous lift coefficient |
| C_{max} : | Maximum Courant number |
| C_μ : | Turbulent-viscosity constant in κ - ε model |
| $\overline{C_p}$: | Average pressure coefficient over cylinder surface |

| | |
|------------------------|---|
| E : | Log law constant |
| F_D : | Instantaneous drag force |
| $\overline{F_D}$: | Mean drag force |
| F_L | Instantaneous lift force |
| $\overline{F_L}$: | Mean lift force |
| f_v : | Vortex shedding frequency |
| g : | Gravitational acceleration |
| h_p : | Normal distance between first node and the wall |
| I_u : | Turbulence frequency |
| k : | Turbulent kinetic energy |
| p : | Static pressure |
| p_0 : | Hydrostatic pressure |
| p_0 : | Inlet pressure |
| \bar{p} : | Mean pressure |
| Re : | Reynolds number |
| S : | Coordinate along cylinder surface |
| St : | Strouhal number |
| t : | Time |
| Δt : | Time step |
| T_v : | Vortex shedding period |
| U : | Fluid velocity |
| U_i : | Cartesian component of the velocity vector |
| \bar{U} : | Mean velocity |
| U_∞ : | Incident velocity |
| u^+ : | Dimensionless velocity |
| $\overline{u_i u_j}$: | Reynolds stress component |
| u_τ : | Friction velocity |

| | |
|--------------|---|
| Δx : | Element length |
| X : | Horizontal axis in coordinate system |
| Y : | Vertical axis in coordinate system |
| x_i : | Cartesian coordinates |
| y : | Distance from the wall |
| y^+ : | Dimensionless distance from the wall |
| ℓ : | Turbulent length scale |
| θ : | Momentum thickness |
| θ_n : | Angle that the outer normal of dA on the structure makes with the positive flow direction |

Introduction.

Circular cylinders are often found in the marine offshore industry. Examples of these circular cylinders are risers used for drilling and bringing hydrocarbons to the surface, the hull of a SPAR platform, pipelines on the seabed, fish nets in fish farms, and the columns of a semi-submersible. All of them represent different types of circular cylinders. Examples of use with two or more circular cylinders are multiple risers expanded from the side of a rig, the legs of an offshore platform and dual pipelines. The tandem cylinders arrangement is the basis of the multiple cylinder cases and all of these different configurations of circular cylinders will bring flows behind them that will be different to each other. It is very interesting to observe how fluid flow is influenced by the change in the arrangement of the cylinders. Any type of blockage or change in geometry will lead to changes in the flow, which can result in an unexpected response of the constructions.

It is not only in the offshore industry we find circular cylinders in diverse configurations. Most of the research done on the topic is based on the aviation industry where airflow over components on airplanes was investigated and controlled. Chimneys, TV towers, wind turbines as well as nuclear power plants are some other examples of circular cylinder application in engineering technology. It is crucial to understand the flow around tandem cylinders to be able to optimize designs and to avoid large movements of the downstream cylinder.

Chapter 1.

Theory

The aim of this chapter is to describe the basic principles of the mechanism of the vortex shedding and the computation of hydro dynamical forces. While the flows around circular cylinders are the most well documented phenomena in the literature. The general knowledge for flow around blue bodies is represented by the formation of the vortex shedding mechanism and the force calculation procedure. For a more thorough review of flows around circular cylinders, the reader is referred to [1].

1.2 Flow regime

The Reynolds number is used to describe the flow around a smooth circular cylinder:

$$Re = \frac{U_{\infty} D}{\nu} \quad (1.1)$$

where U_{∞} is the incident velocity, D is the diameter of the cylinder, and ν is the kinematic viscosity of the fluid.

The regimes of flow around a smooth, circular cylinder in steady current are shown in Figure 1.1. The separation of the fluid stream from the surface of the body at begins at sufficiently high Reynolds numbers. Instead, no separation occurs for $Re < 5$, and for $Re > 40$ a vortex street downstream of the cylinder is present. For $200 < Re < 300$ the transition from laminar to turbulent wake occurs.

For $Re > 300$, the wake is completely turbulent, while as the Reynolds number gets increased from $Re = 3.5 \times 10^5$ the boundary layer itself gradually becomes turbulent.










| | | | |
|----|---|---|---|
| a) |  | No separation. Creeping flow | $Re < 5$ |
| b) |  | A fixed pair of symmetric vortices | $5 < Re < 40$ |
| c) |  | Laminar vortex street | $40 < Re < 200$ |
| d) |  | Transition to turbulence in the wake | $200 < Re < 300$ |
| e) |  | Wake completely turbulent. A: Laminar boundary layer separation | $300 < Re < 3 \times 10^5$ Subcritical |
| f) |  | A: Laminar boundary layer separation B: Turbulent boundary layer separation; but boundary layer laminar | $3 \times 10^5 < Re < 3.5 \times 10^5$ Critical (Lower transition) |
| g) |  | B: Turbulent boundary layer separation; the boundary layer partly laminar partly turbulent | $3.5 \times 10^5 < Re < 1.5 \times 10^6$ Supercritical |
| h) |  | C: Boundary layer completely turbulent at one side | $1.5 \times 10^6 < Re < 4 \times 10^6$ Upper transition |
| i) |  | C: Boundary layer completely turbulent at two sides | $4 \times 10^6 < Re$ Transcritical |

Figure 1.1. Regimes of flow around a smooth, circular cylinder in steady current [2].

1.2 Vortex shedding

The geometry configuration imposes a pressure gradient, which causes the separation around the cylinder. The vorticity is created along the cylinder boundary layer as a result of the no-slip condition. The separation of the layer from the

cylinder surface forms a free shear layer in the wake, which contains the vorticity which shall, in turn, causes the shear layer to roll up into a vortex (see Figure 1.2). This vortex formation simultaneously happens on both sides of the cylinder. The instability of the pair of vortices cause on one of the vortices to pulled across the wake, cutting off the other. For the next shedding cycle, a vortex is cut off at the other side of the cylinder, rotating in the opposite direction. This alternative manner continues throughout the vortex shedding process, as illustrated in Figure 1.3.

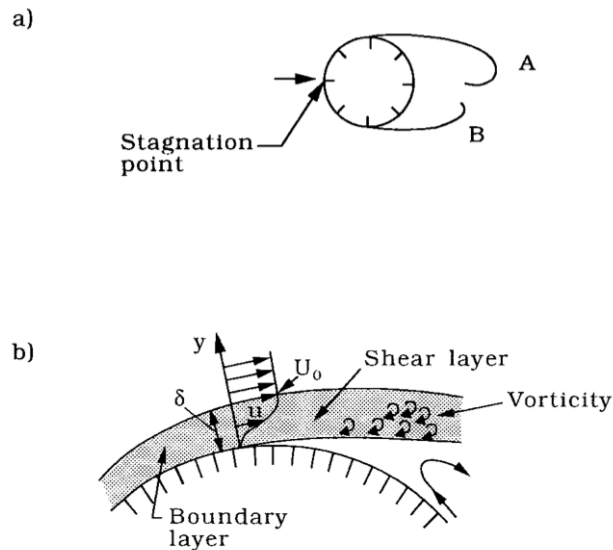


Figure 1.2: The shear layers on both sides roll up to form the lee-wake vortices, vortices A and B [1].

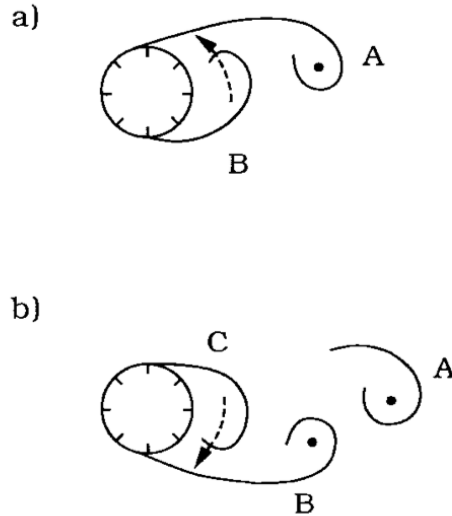


Figure 1.3: The alternative manner of the vortex shedding [1].

1.3 Vortex shedding frequency

Strouhal number measures the vortex shedding frequency. The Strouhal number is defined as

$$St = \frac{f_v D}{U_\infty} \quad (1.2)$$

where $f_v = \frac{1}{T_v}$ is the vortex shedding frequency and T_v the vortex shedding period.

The Strouhal number can be seen to be a function of the Reynolds number by dimensional ground. For a laminar vortex street, the Strouhal number is increasing up to the value of 0.2. It stays near to constant in the subcritical domain but rapidly increases in the critical regime as soon as one of the separation points starts to become turbulent. The change of position for the separation points determines the decreasing in the supercritical regime while a drop occurs when it reaches the upper transition (as the boundary layer is completely turbulent at the one side). Figure 2.4 illustrates how the Strouhal number varies with Re.

1.4 Forces acting on a cylinder

The effects of the impact between the fluid and the structure depend on pressure and friction. The in-line, mean components of the pressure force and the friction forces are denoted F_p and F_f , respectively. The total in-line force, the mean drag force, is given by the sum of these forces:

$$F_D = F_p + F_f \quad (1.3)$$

The changing of the pressure distribution around the object is due to the vortex shedding. This results in a cross-stream force and due to symmetry in the flow; the mean lift force will be zero.

Due to the vortex-shedding phenomenon, the pressure distribution depends on by time and for this reason, the distribution undergoes a periodic change as the shedding process progresses. This results in a periodic variation in the force components on the cylinder. Figure 1.4 shows how the forces are changing throughout a time-series. The lift force oscillates around zero at the vortex-shedding period, T_v , while the drag force oscillates around the mean drag at

$$\frac{1}{2} T_v.$$

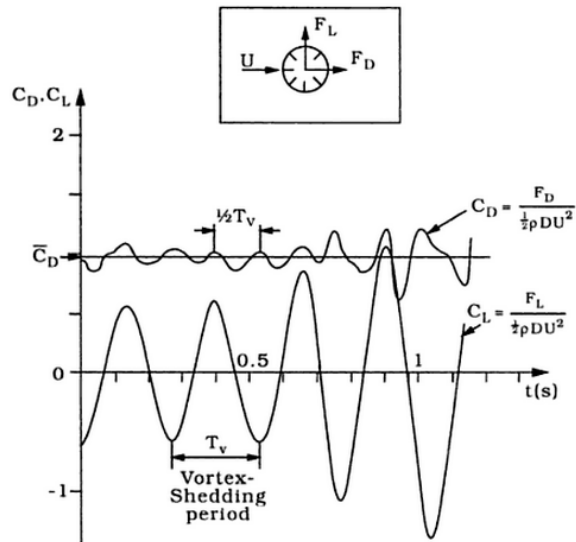


Figure 1.4 Drag and lift traces obtained from the measured pressure distributions [1].

1.5 Force coefficients

The instantaneous drag and lift forces coefficients are defined as follows:

$$C_D = \frac{F_D}{\frac{1}{2}\rho U_\infty^2 D}, \quad (1.4)$$

$$C_L = \frac{F_L}{\frac{1}{2}\rho U_\infty^2 D} \quad (1.5)$$

where ρ is the density of the fluid, F_D is the drag force and F_L the lift force.

Figure 1.4 illustrates the coefficients for a time series.

1.6 Interference regions

There are several different ways to arrange cylinders but only three categories of arrangements are identified; side-by-side arrangement, tandem arrangement, and staggered arrangement. Hence with the different arrangement of the cylinders, there are many different kinds of flow interference. The different interference regions are shown in figure 1.5.

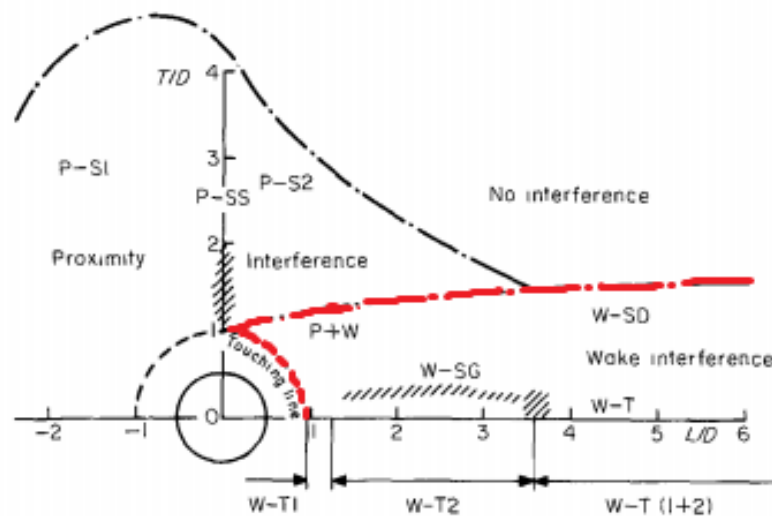


Figure 1.5 Regions of interference around a circular cylinder. [3].

At the present study the tandem arrangement is considered. The figure 1.5 shows region for upstream and downstream cylinders marked by the red dotted line. According to [3] the tandem cylinders experience two types of wake interference; with or without vortex shedding from the upstream cylinder, but there are also subdivisions and from this the following classification:

- W-T1. A regime with no reattachment of the separated shear layer from the upstream cylinder onto the downstream cylinder. This happens for pitch distances $1 < L/D < 1.1 - 1.3$. The free shear layers from the upstream cylinder form the eddy street behind the cylinders. It is often said that the two cylinders

act as a single body in this regime.

- W-T2. In this region the free shear layer from the upstream cylinder reattaches onto the downstream cylinder alternately, permanently or intermittently. Now, the vortex shedding only takes place behind the downstream cylinder. $1.1 - 1.3 < L/D < 3.5 - 3.8$
- W-T (1+2) is the coupled vortex shedding regime. $3.8 < L/D < 5 - 6$. There are two vortex streets that are synchronized in phase and frequency. The vortices shed from the upstream cylinder pair with the vortices behind the downstream one.
- W-T (1 or 2). This is a bi-stable regime. $3.0 < L/D < 4.0$. An intermittent changeover takes place with and without vortex shedding from the upstream cylinder.
- WT (1,2). Here we see uncoupled vortex shedding, which happens for pitch distances $L/D > 5-6$.

All pitch distances are dependent on the Reynolds number. [4]. Figure 1.6 shows varying the critical spacing between two tandem cylinders independent with varying Re .

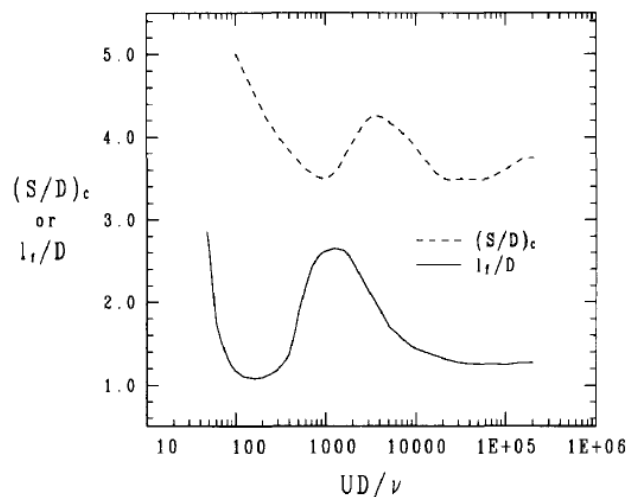


Figure 1.6. Critical spacing between two tandem cylinders and vortex formation length for a single cylinder as a function of Reynolds number [4].

1.7 Flow pattern

According to [5], the different types of interference will naturally induce different flow patterns around the tandem cylinders. These flow patterns will vary with pitch distances and Reynolds number. According to [5] classified different flow patterns for various pitch distances and various Reynolds numbers can be represented by figures 1.7 and 1.8.

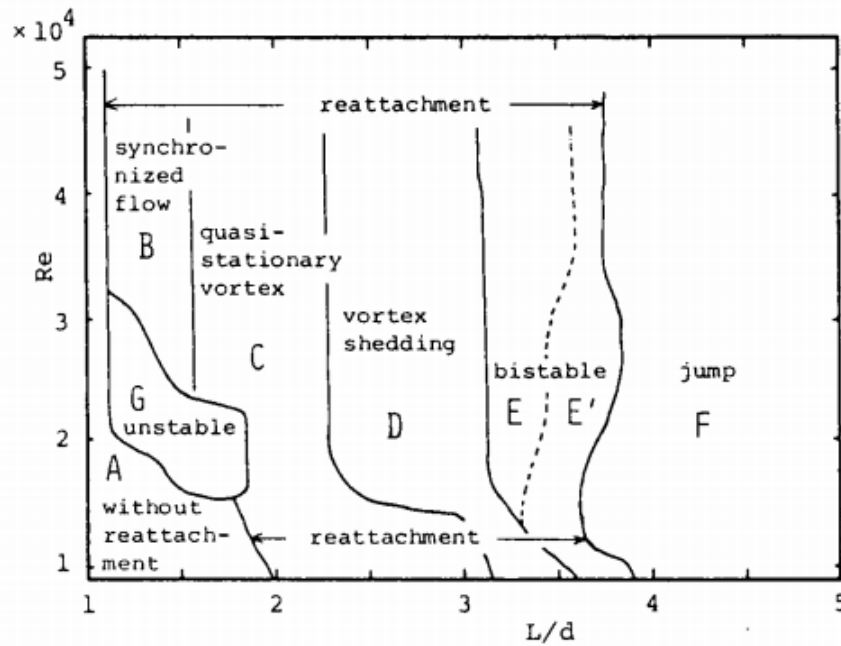


Figure 1.7. Classification of flow patterns for different pitch distances and Reynolds numbers [5].

Pattern

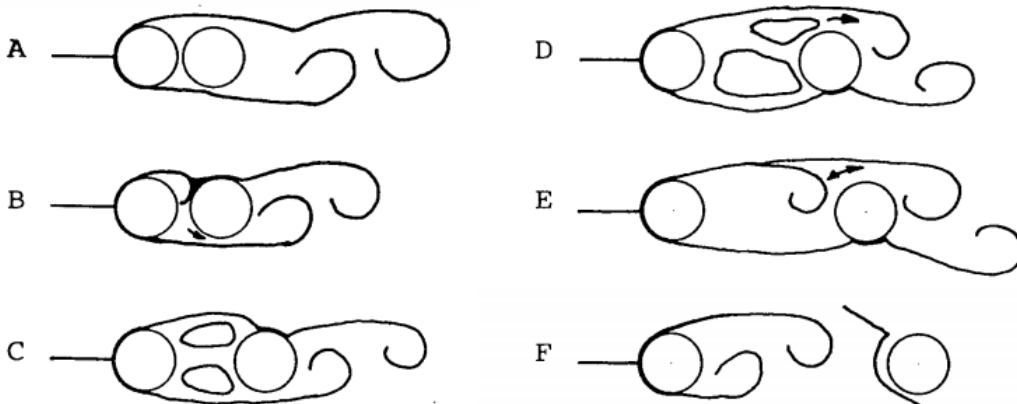


Figure 1.8. Different flow patterns for tandem cylinders [18].

These models are reported as follows [5]:

- The separated shear layer from the upstream cylinder does not reattach onto the downstream cylinder. The two cylinders act like a single body.
- Vortex formation of the shear layer and vortex shedding in the near wake of the downstream cylinder and reattachment of the other shear layer onto the downstream cylinder are synchronized. The frequency of the vortex shedding is nearly constant irrespective of the free stream velocity.
- Quasi-stationary vortices are formed between the cylinders.
- The quasi-stationary vortices become unstable and the vortex shedding is detected intermittently.
- The separated shear layer from the upstream cylinder rolls up intermittently for a moment in front of the downstream cylinder. This is a bi-stable flow between D and F .
- A bi-stable flow whose one model continues for a long time is predominant.
- The separated shear layer from the upstream cylinder rolls up in front to the downstream cylinder.
- Unstable flow in the transition region between models A , B and C .

In the present study both models C and D are considered.

1.8 Pressure distributions and fluctuations

For $Re > 10^4$, the contribution of the friction drag to the total drag force is less than 2 - 3% [1]. At the present study, the total mean drag force F_D might be supposed to that be composed of the form drag

$$\overline{F_D} \cong \overline{F_p} \quad (1.6)$$

The measured pressure distributions for different values of Re are shown on figure 1.9. The following formula explains the pressure distribution obtained from the potential flow theory

$$\bar{p} - p_0 = \frac{1}{2} \rho U_\infty^2 (1 - 4 \sin^2 \phi) \quad (1.7)$$

where p is the mean pressure, p_0 is the hydrostatic pressure and ϕ is the angular coordinate. Between the measured pressure distribution and the potential theory there are two main differences: the pressure at the rear side is negative and near to constant condition. The negative pressure at the rear side is due to separation. The wake region is weak compared to the outer-flow, resulting in a near-to constant value.

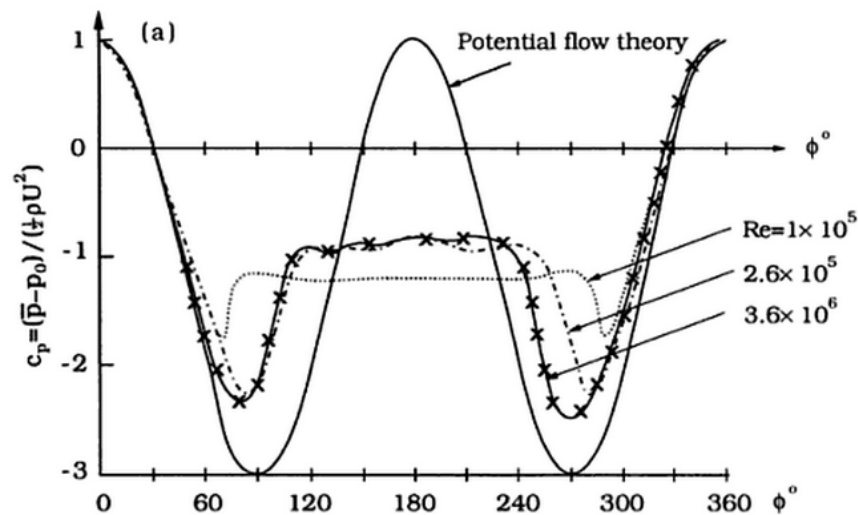


Figure 1.9. Pressure distribution at different Re numbers for a smooth cylinder [1].

The pressure distributions around tandem circular cylinders better describe what happens concerning the flow image. The pressure is a primary output from numerical simulations, then, for this reason, data gives us the most accurate information since it has not been subjected to manipulation in the software. Understanding the most prominent characteristics of the pressure distribution profiles, it allows identifying flow patterns.

The different varieties of C_p arrangements for the upstream and downstream cylinders are given by [3] as:

Upstream cylinder:

1. A positive pressure coefficient, C_p , in the stagnation point region
2. Favorable and adverse pressure gradients along the surface
3. Almost constant base pressure coefficient for upstream cylinder, C_{pb1} .

Where the base pressure is the pressure at $\theta = 180$ degrees.

Downstream cylinder:

- The base pressure behind the upstream cylinder, C_{pb1} faces the upstream side of the gap and the gap pressure on the downstream cylinder, C_{pg2} is exerted along the front side of the downstream cylinder. $C_{pb1} = C_{pg2}$ indicates that there is a lack of flow in the gap.
- If $C_{pg2} < C_{pb1}$, C_{D2} is negative and the drag force acts as a thrust
- There are two symmetric peaks in the pressure at the sides of the downstream cylinder for $L/D \sim 2$. This indicates reattachment of the shear layers from the upstream cylinder onto the downstream cylinder. These peaks are not seen for very small and very large pitch distance.
- These types of pressure distributions were based on the results of experiments done by [6]. These experiments were done for spacing ratio of $L/D = 1.2; 2; 3$. And Reynolds number $Re = 8 \times 10^3$.
- Later, [5] did extensive research on the pressure distribution around tandem cylinders in the subcritical flow regime. Figure 1.10 is taken from his experiments. They show the pressure distribution around the upstream and downstream cylinder for $Re = 3.5 \times 10^4$ and spacing varying from $L/D = 1.03 - 3.97$.

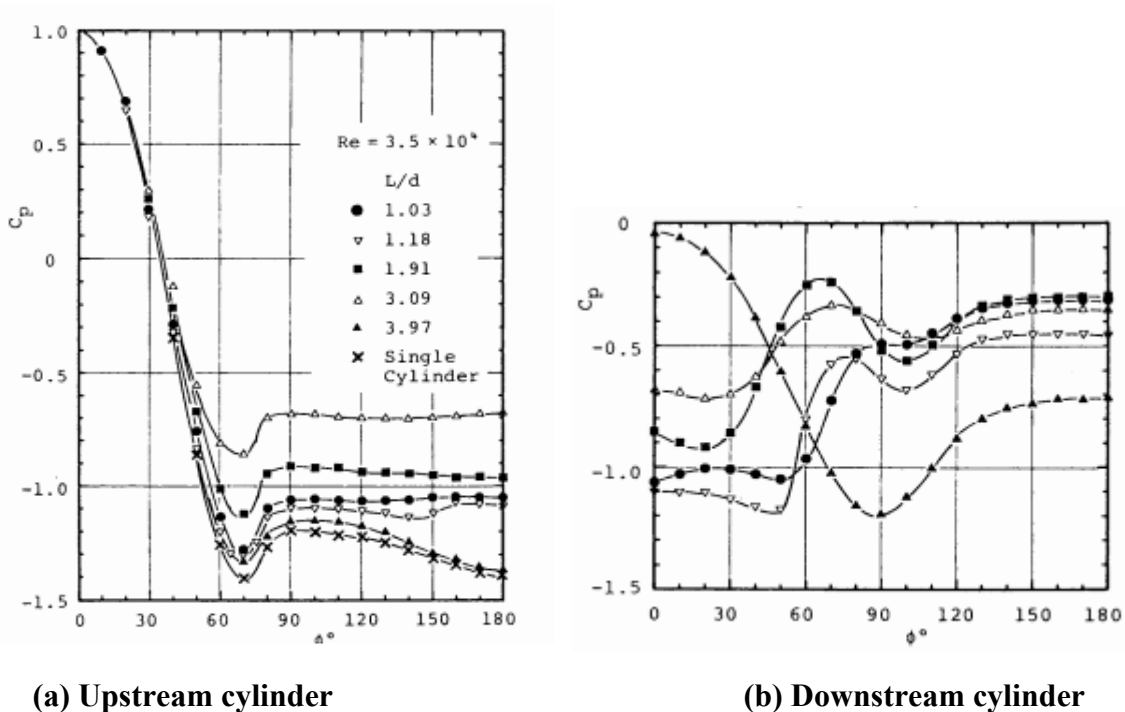


Figure 1.10: Pressure distribution around tandem cylinders. [5].

In figure 1.10(a) the C_p characteristics listed above. In the stagnation point (at 0 degrees) there is a positive pressure coefficient. After this point, we see a favorable pressure gradient. The pressure gradient switches at about 70 degrees and then it changes. For small pitch distance, the base pressure coefficient for the upstream cylinder shows a rather flat curve. The base pressures are almost the same as the gap pressure coefficients of the downstream cylinder shown in figure 1.10(b), which indicates quasi-stationary vortices in the gap region, [5]. The spacing $L/D = 3.97$ is larger than the critical spacing for this Reynolds number, and the pressure distribution of the upstream cylinder shows a profile similar to the one of a single cylinder. The separated shear layers now roll up in front of the downstream cylinder.

The C_p characteristics of the downstream cylinder can be recognized in figure 1.10(b). For spacing up to the critical spacing, the pressure coefficient shows a negative value in the gap and maximum at the reattachment and separation

points. For the smallest spacing, there is no reattachment peak and the two cylinders act as a single body where the shear layers of the upstream cylinder wrap around the downstream one without reattaching. For the largest pitch distances, the pressure distribution shows a similar profile as for a single cylinder with turbulent separation, [5]. This is coherent with vortices shed from the upstream cylinder impinging the downstream cylinder, creating a more turbulent flow. Figure 1.11 shows the pressure fluctuations around tandem cylinders for the same Reynolds number and pitch distance range as figure 1.11. The figure is taken from the same research.

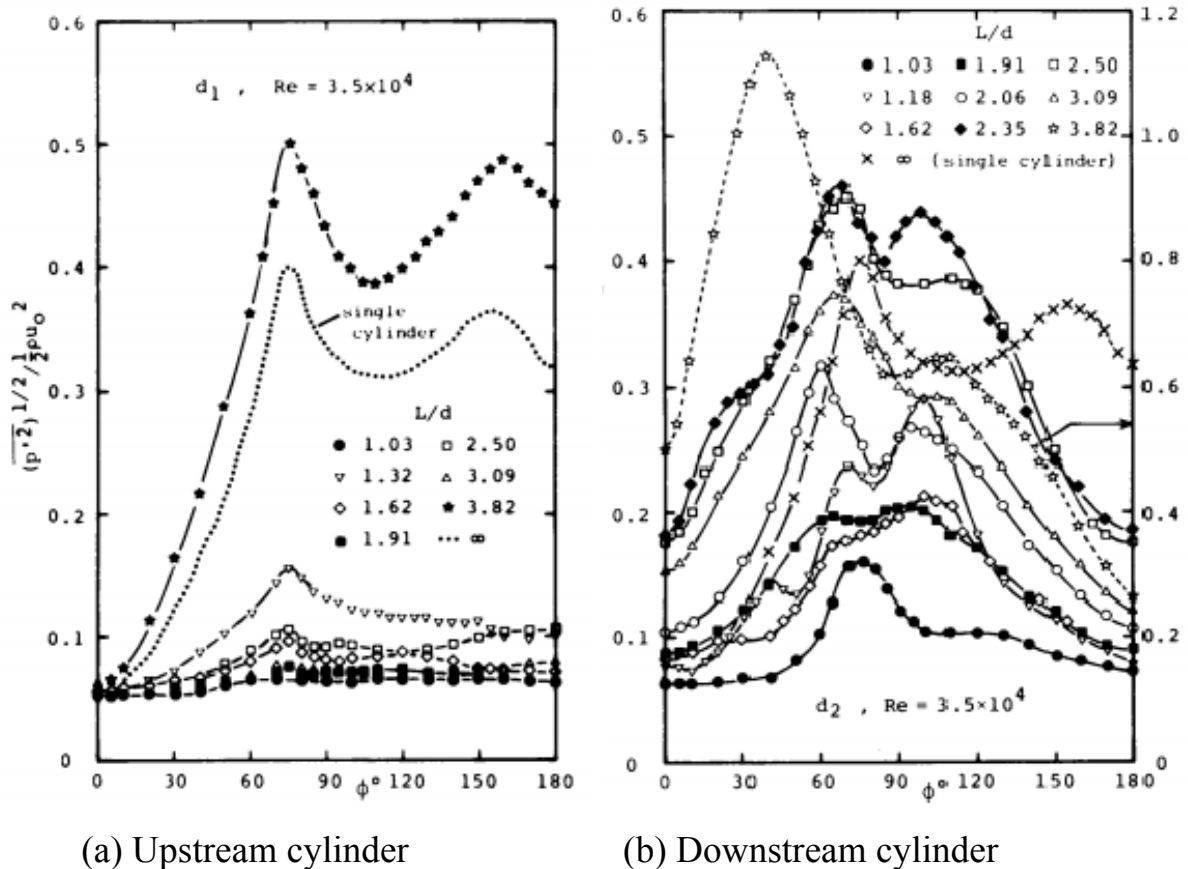


Figure 1.11. Pressure fluctuations around tandem cylinders. [5].

In figure 1.11(a), the peaks in the RMS are located at the separation point.

For spacing up to the critical pitch distance, these values are small, [5]. Beyond the critical pitch distance, the profile is similar to the one of a single cylinder but the magnitudes of the maxima are the larger. The second maximum at this curve is due to the vortex formation, which happens after the separation point. The reversed flow of the separated shear layer attaches onto the rear part of the cylinder and separates again at the position of the second peak in the RMS profile.

Along the downstream cylinder, the RMS distributions show more chaotic profiles. There are two peaks in the RMS profiles for pitch distance up to the critical pitch distance and larger than the pitch distance of single body behavior. One is due to the reattachment point whereas the other is due to the separation point. The fluid flow is more active in the gap as the pitch distance increases, and this has been shown by the increase in RMS at the front part of the downstream cylinder with increased pitch distance. The largest value of the RMS is seen for the pitch distance greater than the critical pitch distance. Here, the downstream cylinder sees a chaotic inflow. Instead, the RMS profile shows only one peak for the smallest pitch distance, and this is the separation peak, due to the two cylinders acting as a single body.

Outline of the thesis

The rest of the thesis is as follows:

Chapter 2 gives an overview of the theory behind flow over circular cylinders.

Chapter 3 gives an introduction to the numerical schemes in OpenFOAM, which is applied in this work.

Part I single cylinder case:

Chapter 4 describes the numerical setup. Boundary conditions, grid verification and post processing tools and methods will be assessed for single cylinder case. Also gives a validation of the numerical model and presents and discusses the results from the study.

Chapter 5 gives conclusion for single cylinder case.

Part II tandem cylinders case:

Chapter 6 Boundary conditions, grid verification and post processing tools and methods will be assessed for tandem cylinder case.

Chapter 7 provides the results and discussion of numerical simulation of boundary layer flow around tandem cylinders close to the seabed

Chapter 8 gives a final conclusion of the work carried out in the thesis, and recommendations for further work.

Chapter 2.

2.1 OpenFOAM

In the present time applied Computing packages are powerful and well-developed apparatus for solving a wide range of physical problems. It is no secret that the world's leading engineering companies, in the creation and testing of a variety of high-tech products, actively use them. They allow you to save money and time by replacing a lot of costly stages of development and testing of numerical experiments. However, the application of these packages in the academic scientific research, until recently has been limited by the following factors. As it is known, the majorities of computer packages are proprietary software and require large financial investments at the stage of purchase. But more important is the fact they contain proprietary software code and thus represents the "black box" for the researcher. This limits the possibilities for the creation, modification, and verification of new numerical models, interfere with the evaluation of the accuracy of the results, and so on. The appearance on the market of free software OpenFOAM package, in the last few years, has allowed changing this situation. Wide tools to formalize the problem, the high efficiency of the implementation, as well as good scalability of the architecture of computer systems, make it easy to construct a numerical model in the package. Open sources, in turn, make it possible to monitor in detail the course of solutions, ranging from the construction of the grid, to select the terms of approximation schemes of the control system and numerical solution methods. The only noticeable drawback of the package is its scanty documentation, which, despite the active development of the package, just recently updated researchers. In this task, the use of OpenFOAM package is considered to solve the problem of Computational fluid dynamics incompressible fluid around cylinders in tandem of.

In connection with this study, we will find much-accompanied information about the numerical scheme and peculiarities of its implementation in the resulting accuracy of the methods. The problem of computational fluid dynamics in an incompressible fluid belongs to the category of promising areas of research of classical fluid mechanics. The challenge keeps large untapped theoretical and practical problems with potentiality. Marine and civil engineering, aerospace engineering and robotics - these are just some of the areas in which the problem has a practical application. From a theoretical perspective, the study uses complex physical interaction mechanisms, structural features of the course, analysis of the integral characteristics. Last not least, the study of issues of stability and too complicated. Another important factor, which attracts modern researchers to the investigated issue, is an extensive base of experimental results, which have been accumulated over the last few decades. This study provides the opportunity for validation of numerical models and also serves as a good starting point for exploring diversified problems.

All simulations procedures based on OpenFOAM CFD simulations comprise of three general steps:

- Pre-processing
- Processing
- Post-processing

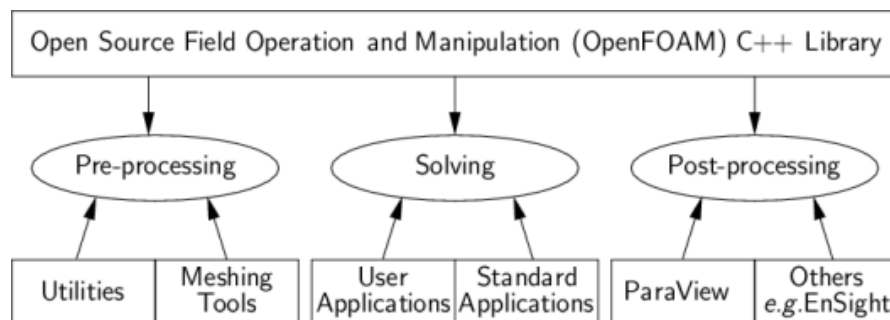


Figure 2.1 Structure of OpenFOAM [7].

2.2 Courant number

The Courant number describes the stability when solving hyperbolic partial differential equations numerically by the method of finite differences. The number indicates the convergence of an analysis. The Courant number is

$$C = U \frac{\Delta t}{\Delta x} \leq C_{max} \quad (2.1)$$

here U is the fluid velocity, Δt is the time step, Δx is the element length and C_{max} is typically equal to 1 [8]

For the Courant number to be less than 1, the time step must be smaller than $\Delta x/U$.

2.3 Turbulence

In practical applications the flow is turbulent. In a turbulent flow, the fluid velocity field varies irregularly in both position and time. The fluctuation of the fluid velocity field takes place in all three dimensions. The result of the turbulence is the more viscosity of the fluid because the flows contain a high amount of vorticity, which increases the ability to transport and mixing the fluid.

The turbulent flows can be predicted by using different approaches. The methods can be grouped into four main categories:

Direct Numerical Simulation (DNS) method

Large Eddy Simulation (LES) method

Reynolds-averaged Navier-Stokes (RANS) method

Hybrid methods, e.g. the Detached Eddy Simulation (DES) method.

These methods are briefly introduced in the following text. For a more thorough review the reader is referred to [8], [9], [10].

2.4 RANS

The Reynolds-averaged Navier-Stokes (RANS) equations are time-averaged Navier-Stokes equations. The RANS method involves solving the RANS equations to determine the mean velocity field and consequently the average values and how the turbulent fluctuations influence these values. When time is averaging the Navier-Stokes equations, additional terms identified by the turbulent fluctuations appear. Including these other terms, more unknowns than equations appear. To solve the system, additional equations are required. These are model equations which model the enhanced stirring caused by turbulent eddies. This results in a considerable reduction of computational cost. The equations to be solved are given by

$$\frac{\partial u_i}{\partial x_i} = 0 \quad (2.2)$$

$$\frac{\partial U_i}{\partial t} + \frac{\partial U_j U_i}{\partial x_j} = -\frac{1}{\rho} \left(\frac{\partial p}{\partial x_j} \right) + \nu \frac{\partial^2 U_i}{\partial x_j^2} - \frac{\partial \overline{u_i u_j}}{\partial x_j} \quad (2.3)$$

where $I, j = 1, 2$ and $\overline{u_i u_j}$ is the Reynolds stress component.

$$-\overline{u_i u_j} = \nu_T \left(\frac{\partial U_i}{\partial x_j} + \frac{\partial U_j}{\partial x_i} \right) - \frac{2}{3} k \delta_{ij} \quad (2.4)$$

where $I, j = 1, 2$, ν_t is the turbulent kinematic viscosity, k is the turbulent kinetic energy and δ_{ij} is the Kronecker delta.

2.5 k - ε model

A turbulence model determines the Reynolds stresses and in the present study, the k -epsilon model is used. This model is the simplest and the most widely used complete turbulence model. It is incorporated in most commercial CFD codes, and can be applied to any turbulent flow. The model belongs to the class of two-equation models.

In this model, two more transport equations are added which must be solved simultaneously with the RANS equations. One equation is used for the turbulent kinetic energy, and one is used for the rate of dissipation of the turbulent kinetic energy. These variables approximate the eddy viscosity and the Reynolds stresses.

The k equation is given by the following formula:

$$\frac{\partial k}{\partial t} + \frac{\partial k U_j}{\partial x_j} = \frac{\partial}{\partial x_j} \left(\frac{\nu_T}{\sigma_k} \frac{\partial k}{\partial x_j} \right) + \nu_T \left(\frac{\partial U_i}{\partial x_i} + \frac{\partial U_j}{\partial x_i} \right) \frac{\partial U_j}{\partial x_j} - \varepsilon \quad (2.5)$$

here $i, j = 1, 2$, σ_k is the turbulent Prandtl number for kinetic energy and ε is the rate of dissipation of turbulent kinetic energy.

The following formula explains the standard model equation for ε :

$$\frac{\partial \varepsilon}{\partial t} + \frac{\partial \varepsilon U_j}{\partial x_j} = \frac{\partial}{\partial x_j} \left(\frac{\nu_T}{\sigma_\varepsilon} \frac{\partial \varepsilon}{\partial x_j} \right) C_{\varepsilon 1} \frac{\varepsilon}{k} \nu_T \left(\frac{\partial U_i}{\partial x_j} + \frac{\partial U_j}{\partial x_i} \right) \frac{\partial U_j}{\partial x_j} - C_{\varepsilon 2} \frac{\varepsilon^2}{k} \quad (2.6)$$

here $i, j = 1, 2$, σ_k is the turbulent Prandtl number for dissipation, $C_{\varepsilon 1}$ and $C_{\varepsilon 2}$ are modal equation's constants for ε . [11]

2.6 Characteristics of the flow around a circular cylinder near a plane boundary.

The flow around circular cylinder and forces, which affected by the by the proximity of the seabed are shown in figure 2.2. The flows illustrated by considering the sea bottom such as a flat and stiff wall. Several types of researchers have explored the flow around circular body close to the seabed. This flow configuration is a big challenge for coastal and offshore engineers and represents a high scientific interest, and has a series of others, practical researchers. In other words, those interested in a construction of bridges, pipeline installation and windmills in the open sea respectively. [12].

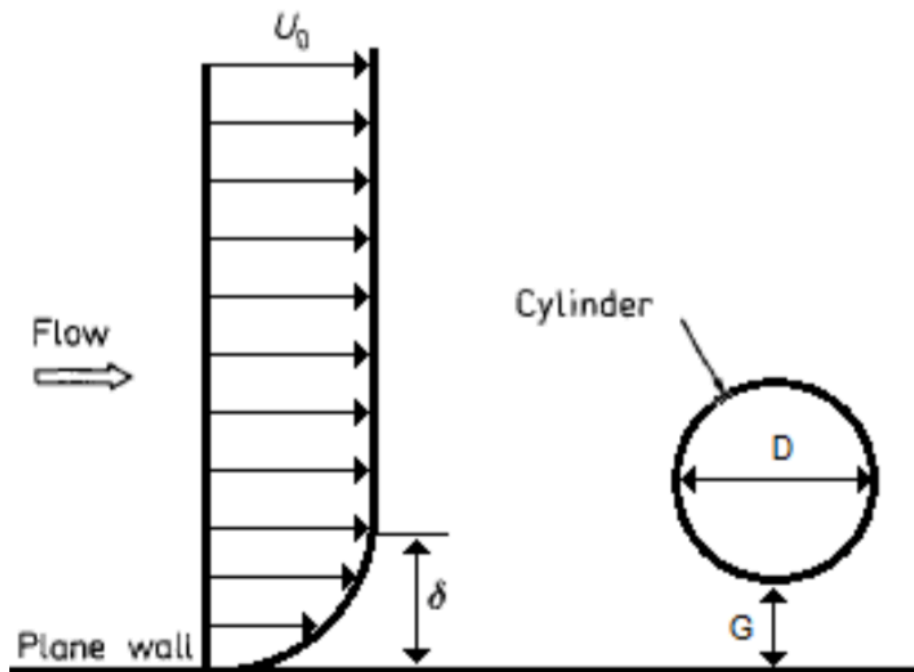


Figure 2.2. Sketch of the flow geometry for a cylinder close to the seabed

U_∞ is the free stream velocity in the horizontal axis outside the boundary layer. U_∞ is distant from the structure where the existence of the circular body does

not affect the velocity; hence, the symbol ∞ is used. The boundary layer thickness δ is defined as the length of the wall to where the velocity in x-direction reaches 99% of U_∞ [13]. A gap G separates the circular body and the plane wall and on the whole, a boundary layer creates on the wall. D is a diameter of the cylinder. Also in this paper to determine the distance between a circular body and a plane wall used gap-to-diameter ratio G/D . Previous surveys were done by [14] with high Reynolds numbers $Re = 1 \times 10^6$; $Re = 2 \times 10^6$; $Re = 4 \times 10^6$ with different gap ratios. He was researched cases with $G/D = 1$; 0.8; 0.6; 0.4; 0.3; 0.2; 0.1 respectively. According to his study in cases where gap ratios lower than 0.3 vortices formation are not detected.

[15] claim that the vortex street has formed by concentration of vorticity by roll-up of separated shear layers originating from both sides of the cylinder; the free-stream side shear layer contains clockwise vorticity, while the wall side shear layer contains anticlockwise vorticity. Therefore, the boundary layer formed at the wall has clockwise vorticity. The free flow excludes big-size vortex formation on the cylinder surface wake region. Furthermore, the abolition of opposite vorticity wake in the wall boundary layer and both shear layers on the cylinder surface is observed as the reason of vortex shedding suppression.

Flow separation of the wall boundary layer is observed, at gaps smaller than the critical gap for vortex suppression to overlap with the outer deflection of the wall side shear layer. Observations clearly point to the interaction between the wall shear layer and the wall boundary layer: each (counterclockwise) vortex shed from the wall side of the cylinder has followed by a clockwise vortex in the near-wall region. As a consequence, the wall boundary layer is damaged, and the flow detaches from the wall and emits upwards. Contrary to previous opinions [16] and [12] find that the two shear layers do not cancel each other.

Lin et al. present a summary of past experimental studies of a circular cylinder near a plane boundary. Explains, that the flow phenomena in the wake can be roughly classified into three regions due to the influence of the gap:

- The characteristics of vortex shedding is similar to that of an isolated cylinder,
- The plane boundary influence the vortex shedding and the periodic shedding of the upper shear layer is evident,
- Periodic vortex shedding is suppressed.

Lei et al. executed 2D numerical simulations in the range $Re = 80-1000$ and report the strength of vorticity in the shear layers to decrease and the thickness of the shear layers to increase with decreasing Re . The consequence is suppression of vortex shedding at larger gap ratios for lower Re . For high Re , the critical value approaches $G/D \simeq 0.2$.

Altogether the drag coefficient increases when gap ratio decreases [17]. At low gap ratios, a stable mean lift in the direction away from the wall is observed by [18], notwithstanding dependent on the boundary layer some incidents of lift in the opposite direction are written [17].

At figure 2.3 illustrated uniform going and hitting a horizontal flat wall and how the wall of plate created the boundary layer. At the high Reynolds numbers during the growth of a boundary layer along a surface, turbulence will crop up.

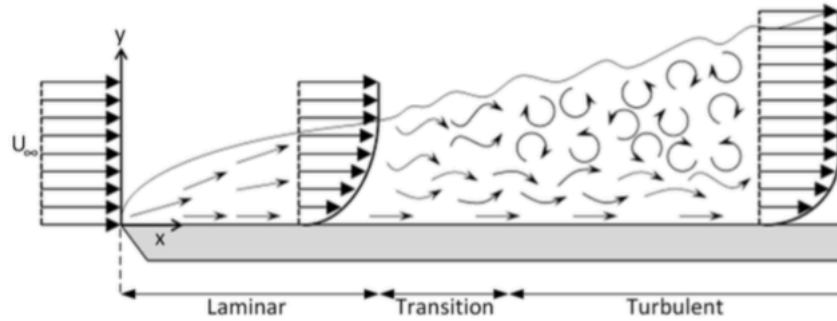


Figure 2.3 Developing boundary layer on a horizontal plate [19].

One more important thing there are some important parameters are must be described the boundary layer profile and its characteristics such as θ , δ and displacement thickness δ^* . Describe formulas θ and δ^* .

$$\theta = \int_0^{\infty} \frac{U}{U_{\infty}} \left(1 - \frac{U}{U_{\infty}}\right) dy \quad (2.7)$$

and

$$\delta^* = \int_0^{\infty} \left(1 - \frac{U}{U_{\infty}}\right) dy \quad (2.8)$$

In both equations dy is the differential vertical distance.

According to [20] can be made an assumption that the turbulent flow along a smooth wall can be considered to consist of multiple layers with different properties.

[20] wrote that two non-dimensional variables could characterize the boundary layer properties for vertical distance and velocity. From the velocity, there is u^+ , from distance y^+ , hence.

$$u^+ = \frac{U}{u_\tau} \quad (2.9)$$

$$y^+ = \frac{\rho y u_\tau}{\mu} \quad (3.0)$$

These formulas included shear velocity $u_\tau = \sqrt{\frac{\tau_\omega}{\rho}}$, τ_ω is surface shear stress and distance from the wall is y . From another word y^+ is the first node thickness and there is a critical parameter to calculate and thereafter obtain correct data.

While whole calculation first node thickness for cylinder wall and sea bottom should be in the range 30-40.

The following equation shows, the dependence between u^+ and y^+ or law of the wall.

$$u^+ = f\left(\frac{\rho u_\tau y}{\mu}\right) = f(y^+) \quad (2.11)$$

In a distance from the wall, in the external domain of the boundary layer, the velocity at a some period described by the velocity defect law,

$$\frac{U_\infty - U}{u_\tau} = g\left(\frac{y}{\delta}\right) \quad (2.12)$$

$g\left(\frac{y}{\delta}\right)$ is a function of given variables.

The laminar sub-layer nearest to the plane wall is the viscous sub-layer; at this region viscous stresses dominate. This layer characterizes as nearly linear; thickness is too small, actually much less than 1% of high of structure h or dimensionless distance from the wall y^+ less than 5. The flow velocity only relies on dimensionless distance from the wall inside the layer, and the velocity profile in

the viscous sub-layer keeps almost constant. Hence, the linear relationship between dimensionless velocity from the viscous sub-layer on a smooth wall can be shown as

$$u^+ = y^+ \quad (2.13)$$

Let us consider an expression for non-dimensional velocity for smooth wall within buffer layer:

$$u^+ = \frac{1}{k} \ln (E y^+) \quad (2.14)$$

where the log-law constant is $E = 9.793$ for smooth walls and $k = 0.41$ is the von Karman constant. The formula 2.14 called as the log-law. The reason of decrease in the log-law constant is the wall roughness it also causes a velocity magnification with the higher value of y^+ compared to a smooth wall, and as a consequence, this results in a thicker boundary layer. At figure 2.4 shown a good correlation between equation 2.13; 2.14, and experimental data for boundary layer over a smooth wall.

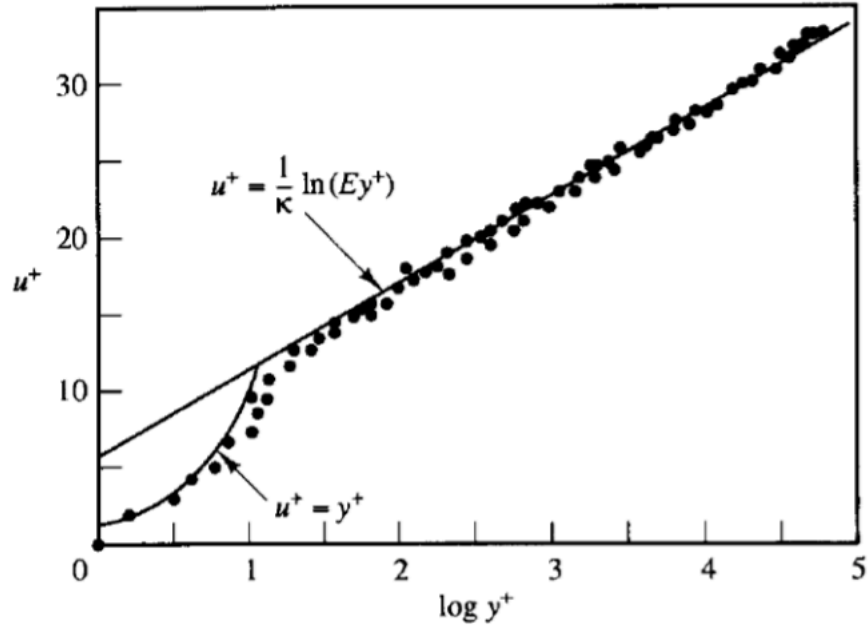


Figure 2.4. Non-dimensional velocity distribution near a smooth wall [20].

Further turn to the outer layer where viscous effects are insignificant and inertial effects predominate. The non-dimensional velocity profile could be expressed as equation 2.15:

$$\frac{U_{\infty} - U}{u_{\tau}} = \frac{1}{k} \ln \left(\frac{y}{\delta} \right) + A^* \quad (2.16)$$

where A^* is a constant.

Chapter 3.

Computational Fluid Dynamics.

3.1 Introduction.

Computational Fluid Dynamics is a necessary tool for analyzing flows around a marine structure. In a real condition such as an open sea, marine structures are often subjected to flows with high Reynolds numbers conditions. Classification of flows divided by three flows: laminar, transition and turbulent flows respectively. A Reynolds number characterizes all three flows. Flows turbulent at high Reynolds numbers. In turbulent flow can be identified that these are so irregular. Nevertheless, they are governed by the extract Navier-Stokes equations.

3.2 Mathematical formulation and Standard High Reynolds number κ - ϵ Model.

The Reynolds-averaged equations for conservation of momentum and mass can be shown as

$$\frac{\partial u_i}{\partial x_i} = 0 \quad (3.1)$$

$$\frac{\partial y_i}{\partial t} = u_j \frac{\partial u_i}{\partial x_i} = \frac{1}{\rho} \left(\frac{\partial P}{\partial x_i} \right) + \nu \frac{\partial^2 u_i}{\partial x_j^2} - \frac{\partial \overline{u_i u_j}}{\partial x_j} \quad (3.2)$$

where i and j variables, which equal 1, 2. Hence u_1 and u_2 constituent element corresponding mean velocity, respectively; x_1 and x_2 denote the vertical and

horizontal directions, respectively; $\overline{u_i u_j}$ is the Reynolds stress components where u_i means the fluctuating part of the velocity; p is the dynamic pressure and ν is the kinematic viscosity. [21].

From turbulent viscosity ν_T and the mean gradient, there is component of Boussinesq approximation can extract the next component is Reynolds stress $\overline{u_i u_j}$

In the present study, κ - ε turbulence model with high Reynold number has been used. [22] described κ - ε model on vortex shedding flow previously. Following by them paper the k and ε equations given by:

$$\frac{\partial k}{\partial t} + u_j \frac{\partial k}{\partial x_j} = \frac{\partial}{\partial x_j} \left(\frac{\nu_T}{\sigma_k} \frac{\partial k}{\partial x_j} \right) + \nu_T \left(\frac{\partial u_i}{\partial x_j} \frac{\partial u_j}{\partial x_i} \right) \frac{\partial u_i}{\partial x_j} - \varepsilon \quad (3.3)$$

$$\frac{\partial \varepsilon}{\partial t} + u_j \frac{\partial \varepsilon}{\partial x_j} = \frac{\partial}{\partial x_j} \left(\frac{\nu_T}{\sigma_\varepsilon} \frac{\partial \varepsilon}{\partial x_j} \right) + C_1 \frac{\varepsilon}{k} \nu_T \left(\frac{\partial u_i}{\partial x_j} + \frac{\partial u_j}{\partial x_i} \right) \frac{\partial u_i}{\partial x_j} - C_2 \frac{\varepsilon^2}{k} \quad (3.4)$$

where ε is the rate of viscous dissipation and $\nu_T = C_\mu \frac{k^2}{\varepsilon}$. In this paper were used standard model coefficients ($C_1 = 1.44$; $C_2 = 1.92$; $C_\mu = 0.09$; $\sigma_k = 1.0$; $\sigma_\varepsilon = 1.3$).

3.4 Mesh

While a simulation process values of pressure and velocity are computed and the flow is determined for each element of the grid. For three-dimensional mesh, the cells are enclosed volumes. The mesh has a considerable influence on the rapidity of convergence, solution precision and CPU time required. During the construction of the grid, it is necessary to pay attention to the factors that affect the accuracy of the solution of the problem, namely: skewness, aspect

ratio, non-orthogonally, cell growth rate and grid density [25].

In constructing the grid for solving scientific and industrial problems triangular elements and a rectangular elements can be used. In solving CFD problems grid with a rectangular elements gives more precise results with fewer elements compared to triangular elements and is practically always used to calculate turbulence models. For the present analysis, rectangular grid is used.

There are two types of grids, structured elements, and unstructured elements of the grid. A structured grid can be numbered according to indices i^* and j^* that does not necessarily correspond to coordinates x_1 and x_2 [24].

Figure 3.1 shows a structured and unstructured grid for rectangular cells.

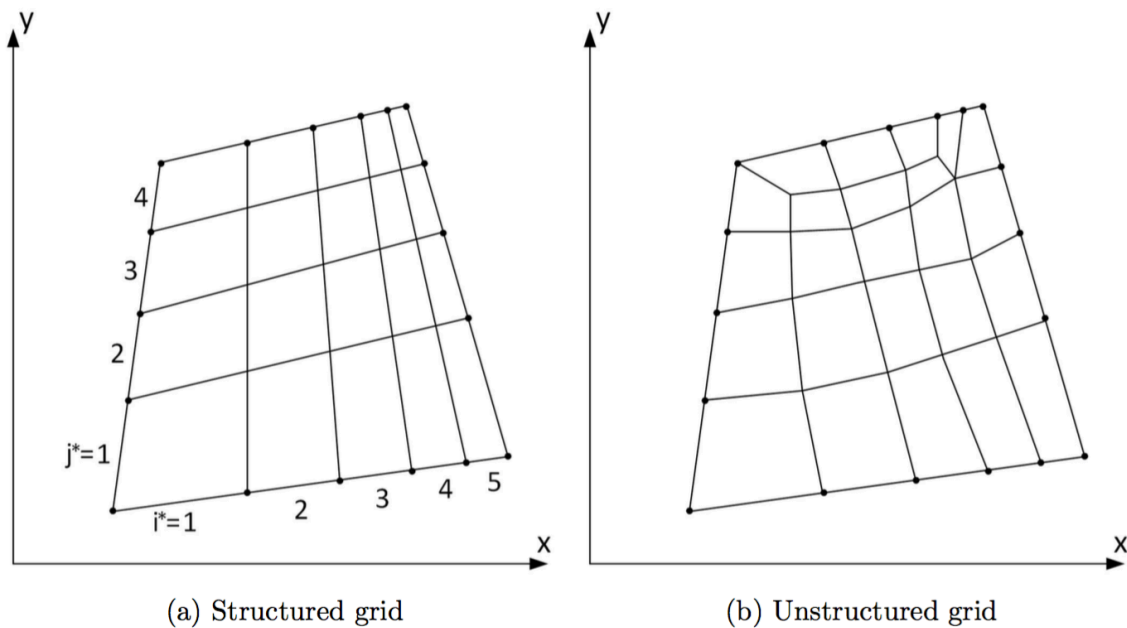


Figure 3.1 Structured and unstructured quadrilateral grid [24].

An unstructured grid represents cells of different shapes which have established in a randomly. Usually, a grid constructed indicating areas, where a minimum and maximum cell size will be constructed, further the generator auto-generates the grid. In contradistinction to the structured mesh, the cells in a grid through of indices cannot be uniquely identified by the indices i^* and j^* . The correctly constructed structured grid includes a minimal number of cells in compared to unstructured, which in turn, reduces the calculation time. Also, structured mesh gives more accurate results.

Chapter 4

Numerical setup

This chapter explains the domain, mesh, boundary conditions and numerical boundary layer used. The same domain and boundary conditions are applied for all simulations while gap-to-diameter ratios for the single cylinder case are changed to get different results. At a same time ye results from single cylinder case will compare with results, which were obtained by [21] from numerical simulations.

4.1 Numerical solution procedure, computational domain and boundary conditions

A computational domain is determined for all CFD problems, and the size of the computational domain is of significant importance when it comes to precision of the solution and computational spending for external flows. If the computational domain is made overly small, the elements of the domain may impact the numerical results such as the hydrodynamic quantities C_D and C_L on a structure. The outcome of an enormously large computational domain is extra cells and superfluous computational costs. Through the optimal selection of a computational domain, it is necessary to employ a domain size, such as examined domain on similar flow tasks or fulfill a domain size convergence test.

A domain size convergence study is where different domain size parameters are varied to view how greatly it influences the numerical results. The parameters may be the high of the computational domain, the length from inlet to the impediment of circulars bodies, and distance of an impediment of circulars bodies to the outlet. The computational domain size is chosen based on the size of

experimental setup that numerical results are compared with, previous numerical results and experiments.

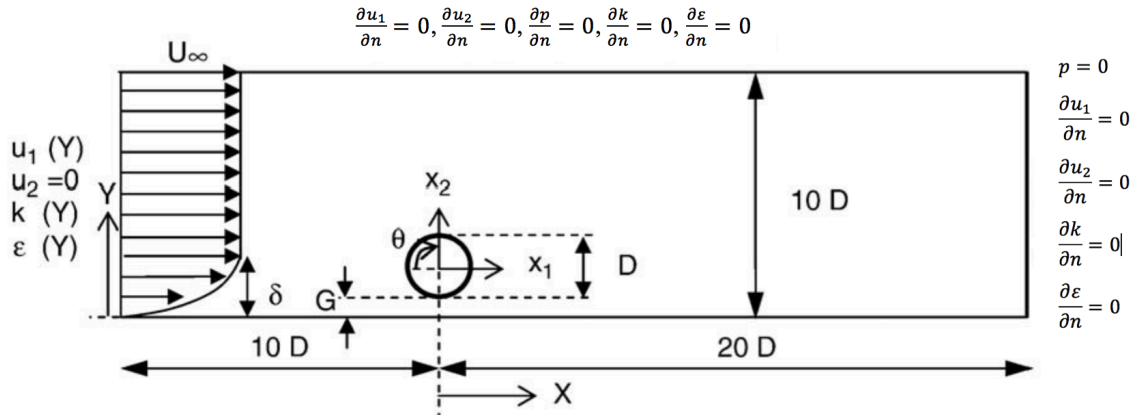


Figure 4.1 Determination sketch for flow around a circular cylinder close to the plane wall.

The size of domain horizontally is $30D$ vertically is $10D$. The cylinder has a diameter of $D = 1$ meter. The previous numerical simulations have been done by [21]. All simulations at the present study have performed with same sizes of computational domain as [21] because all subsequent results will be compared with his results. He set that the distance between the upper boundary and center of the circular cylinder should be varied in the interval from $8.5D$ to $9.4D$ depending on the corresponding gap to diameter ratio. Also in upstream region where is flow inlet situated $10D$ from the center of the cylinder, and in the flow outlet is situated $20D$ downstream from the center of the cylinder. According to [21], this distance is chosen to protect far field effect from the upstream flow to downstream flow of the body. At this stage let us examine the boundary conditions of the computational domain.

(1) A boundary layer flow for inlet figure 4.1

$$u_1(Y) = \min \left\{ \frac{u_*}{k} \ln \left(\frac{Y}{z_w} \right), U_\infty \right\} \quad (4.1)$$

$$u_2(Y) = 0 \quad (4.2)$$

$$k(Y) = \max \left\{ C_\mu^{-1/2} \left(1 - \frac{Y}{\delta} \right)^2 u_*^2, 0.0001 U_\infty^2 \right\} \quad (4.3)$$

$$\varepsilon(Y) = \frac{C_\mu^{3/4} k(Y)^{3/2}}{\ell} \quad (4.4)$$

$$\ell = \min \left\{ kY \left(1 + 3.5 \frac{Y}{\delta} \right)^{-1}, C_\mu \delta \right\} \quad (4.5)$$

Where Y is the wall normal direction beginning from the plane wall (see figure 4.1) and ℓ is an estimate of the turbulent length scale. $u_* = \frac{kU_\infty}{\ln(\delta/z_w)}$ is the friction velocity and $k = 0.41$ is the von Karman constant.

(2) Boundary near-wall conditions are included k and ε values. It should be applied for both plane bottom (sea bottom) and cylinder wall [27] as

$$k = \frac{u_*^2}{\sqrt{C_\mu}} \quad , \quad \varepsilon = C_\mu^{\frac{3}{4}} \frac{k^{\frac{2}{3}}}{kh_p} \quad (4.6)$$

Here h_p denotes is the radial distance between the wall to the first node (see figure 4.2) and u_* means the wall friction velocity received from the logarithmic law [14]

$$\frac{u_{tan}}{u_*} = \frac{1}{k} \ln \left(\frac{h_p}{z_*} \right) \quad (4.7)$$

Where the tangential velocity is u_{tan} , $z_* = (z_0, z_w)$ where z_0 the roughness parameter

of the cylinder surface and z^* is a switch parameter for the wall roughness according to the [14]. In the present study, a small roughness $z_w = 1 \times 10^{-6}$ was used for the cylinder. The Reynolds number for all simulations is equal $Re = 3.6 \times 10^6$.

- (3) In the outlet boundary conditions static pressure $p = 0$.
- (4) No slip boundary conditions on the plane wall and on the cylinder, this means $u_1 = u_2 = 0$.
- (5) The top of computational domain has to have a slip boundary conditions where $u_1 = U_\infty$ and $u_2 = 0$ since the top wall located sufficiently far away from the cylinder and the plane bottom
- (6) Front and back surfaces are empty to convert our computational domain from 3D model to 2D.

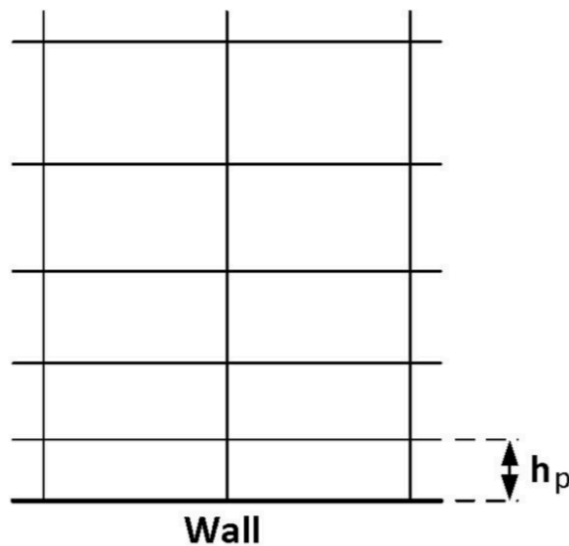


Figure 4.2 Mesh close to a wall with illustration of h_p

As previously reported the mesh should have on both cylinder and bottom wall boundary y^+ in an interval from 30 to 45 because this parameter may occur on drag and lift coefficient while calculation of simulation model. And another important factor is a good transaction between geometry objects on the

computational domain (see figures 4.3, 4.4, 4.5).

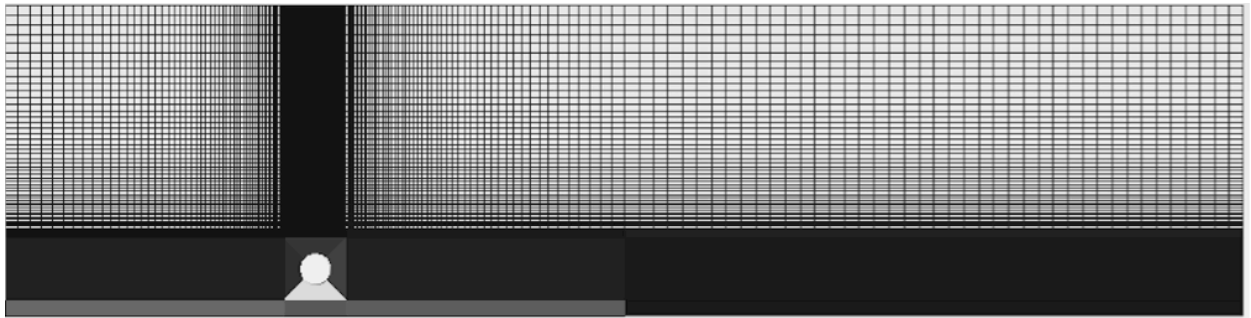
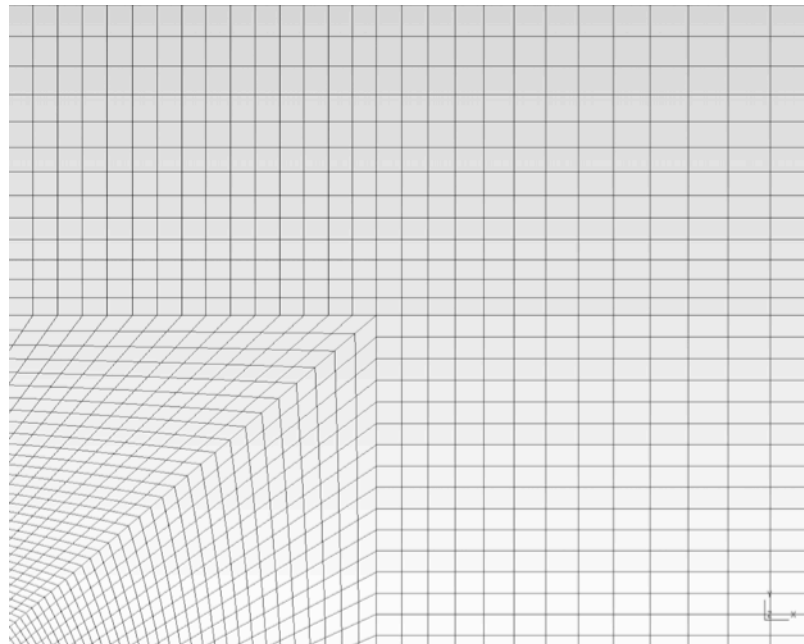


Figure 4.3 Global mesh for a single cylinder case at $G/D = 1$



Figures 4.4 Transition between geometries elements

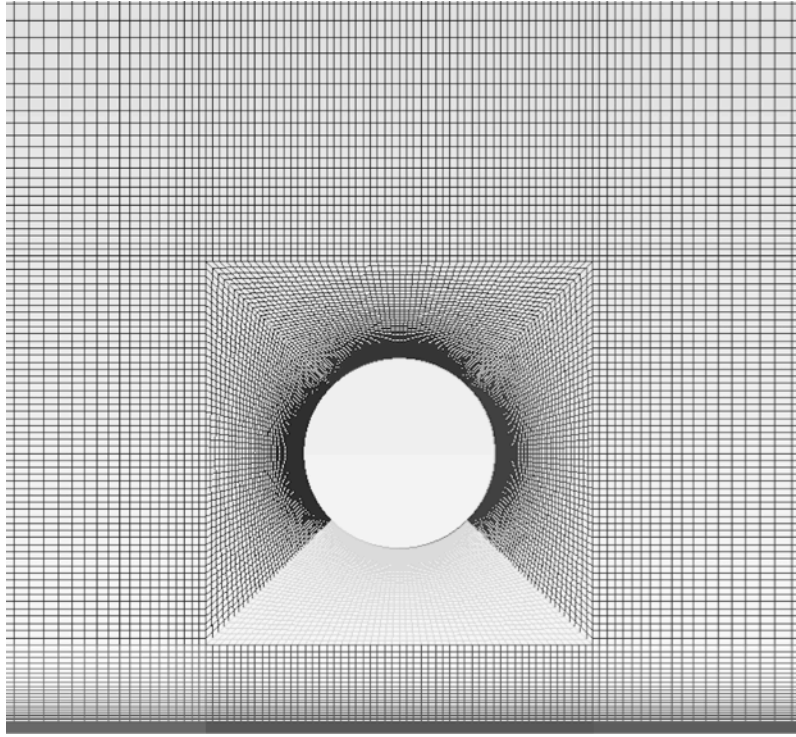


Figure 4.5 Local mesh for single cylinder case $G/D = 1$

At the present study, three cases with different gap-to-diameter ratios were considered: $G/D = 1$; $G/D = 0.8$; $G/D = 0.5$, at the different numbers of cells 20×10^3 ; 30×10^3 and 40×10^3 are reviewed.

4.2 Convergence studies

As previously reported, the present study the upper-transition flow regime ($Re = 3.6 \times 10^6$) was used for all cases of $\delta/D = 0.5$ and $G/D = \{0.5; 0.8; 1\}$. The drag and lift coefficients (C_D and C_L) based on time-averaged integrated horizontal and vertical forces, respectively, which acting on the cylinder. The definitions of both forces give the next equations:

$$F_D = 0.5 \rho D C_D U_\infty^2 \quad (4.8)$$

$$F_L = 0.5\rho DC_L U_\infty^2 \quad (4.9)$$

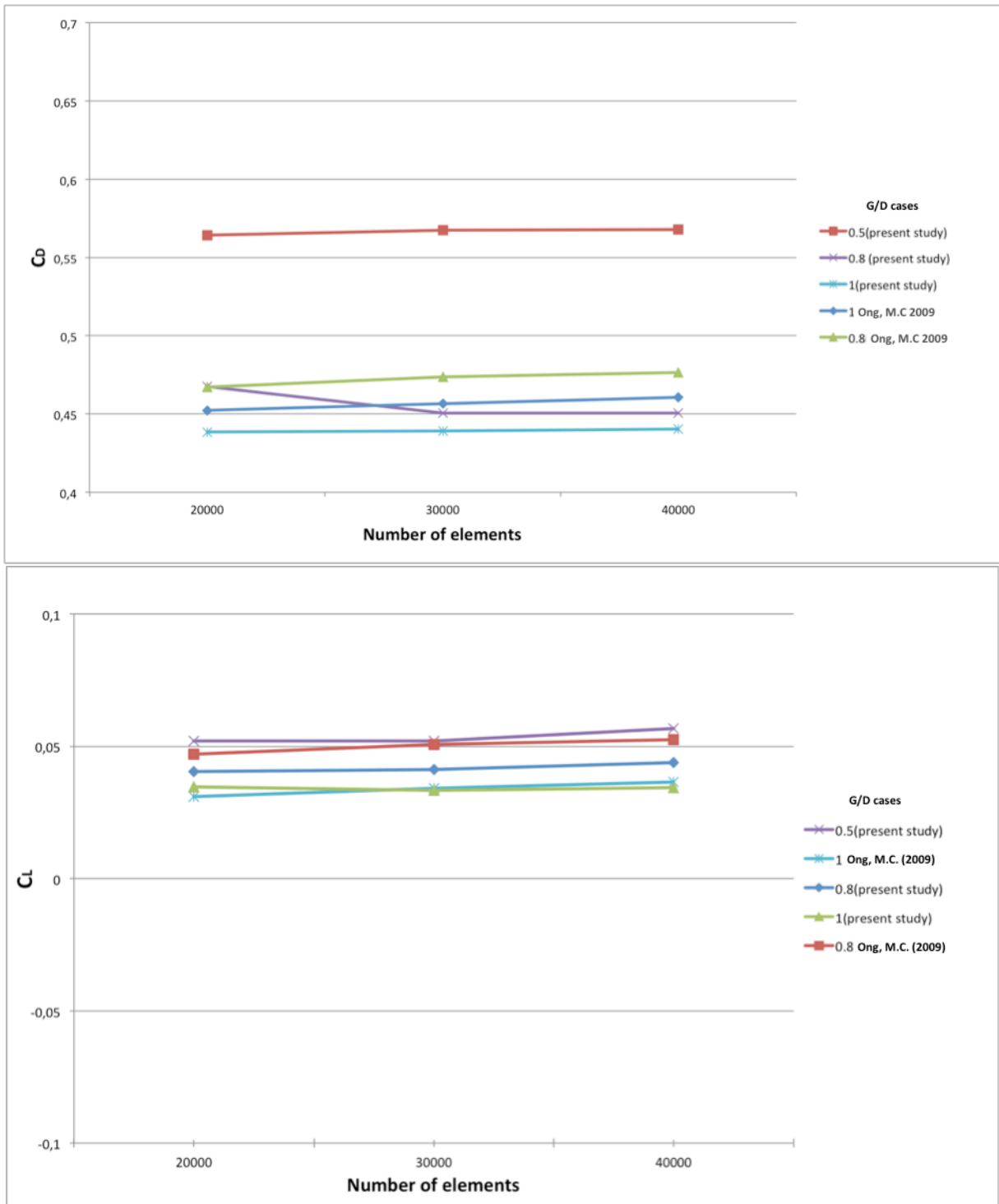


Figure 4.6 Grid convergence for C_D and C_L with respect to the number of elements in the computational domain for $Re = 3.6 \times 10^6$ with $\delta/D = 0.5$ and $z_w = 1 \times 10^{-6}$

For this case, three meshes with approximately 20000, 30000 and 40000 elements are utilized to fulfill the grid convergence studies. By comparing results with different numbers of cells, namely C_D and C_L (drag and lift coefficients, respectively), results vary depending on the number of cells in each mesh. At this stage, the select the optimal number of cells is going for a simulation. The logic is simple. First of all, we used to mesh with a lower number of cell then with a larger number of cell and compare these results, if they are differ we run simulations one more time with a larger number of cells, and as long as the results will not be a small difference approximately 5% between each other. It gives more accuracy results. In as much, in case $G/D = 1$ C_D varies from 0.114% to 0.27% and C_L varies from 2.90% to 4.02%. Therefore, 40000 cells grid was chosen. See table 1

Table 1. Results from grid convergence study for circular cylinder with gat-to-diameter ratio [0.5; 0.8; 1]

| G/D | Elements | Δt | C_D | % | C_L | % | St |
|------|----------|------------|--------|-------|--------|------|--------|
| 1 | 20831 | 0.002 | 0.4385 | | 0.0348 | | 0.2712 |
| 1 | 31040 | 0.002 | 0.4390 | 0.114 | 0.0334 | 4.02 | 0.2712 |
| 1* | 40532 | 0.001 | 0.4402 | 0.27 | 0.0344 | 2.90 | 0.2712 |
| 0.8 | 20831 | 0.002 | 0.4677 | | 0.0403 | | 0.2712 |
| 0.8 | 31040 | 0.002 | 0.4503 | 3.72 | 0.0414 | 2.66 | 0.2712 |
| 0.8* | 40504 | 0.001 | 0.4504 | 0.023 | 0.0437 | 5.26 | 0.2712 |
| 0.5 | 20324 | 0.002 | 0.5644 | | 0.0519 | | 0.2709 |
| 0.5 | 30704 | 0.002 | 0.5675 | 0.55 | 0.0519 | 0 | 0.2709 |
| 0.5* | 40501 | 0.001 | 0.5681 | 0.10 | 0.0567 | 8.47 | 0.2710 |

* The final case for analyses.

4.3 Results and discussion

Numerical simulations of flow around a single circular cylinder with gap-to-diameter ratio $G/D = \{0.5; 0.8; 1\}$ have been performed. And the discussion will be focused on upper transition regime with high Reynolds number flows at $Re = 3.6 \times 10^6$ with $z_w = 1 \times 10^{-6}$ and $\delta/D = 0.5$. The present result will be confirmed by comparing the present results with published numerical results for single cylinder body to a steady flow in the same flow regime, in particular with results of [14][21].

The average value of a distance between the first node and wall (bottom and cylinder), y^+ in the present study was equal in range $30 < y^+ < 40$ to perform the log-law demands.

At figure 4.7 values of C_D versus G/D are demonstrated. As we can see when G/D increase C_D decrease, approaching a constant. This means that the impact from the bottom becomes negligible. According to [14] it is correct for cases with $G/D > 0.3$. In table 2, C_D results from the present study comparing with published experimental data of [18] and numerical results of [14] are shown, for the case with $G/D = 1$.

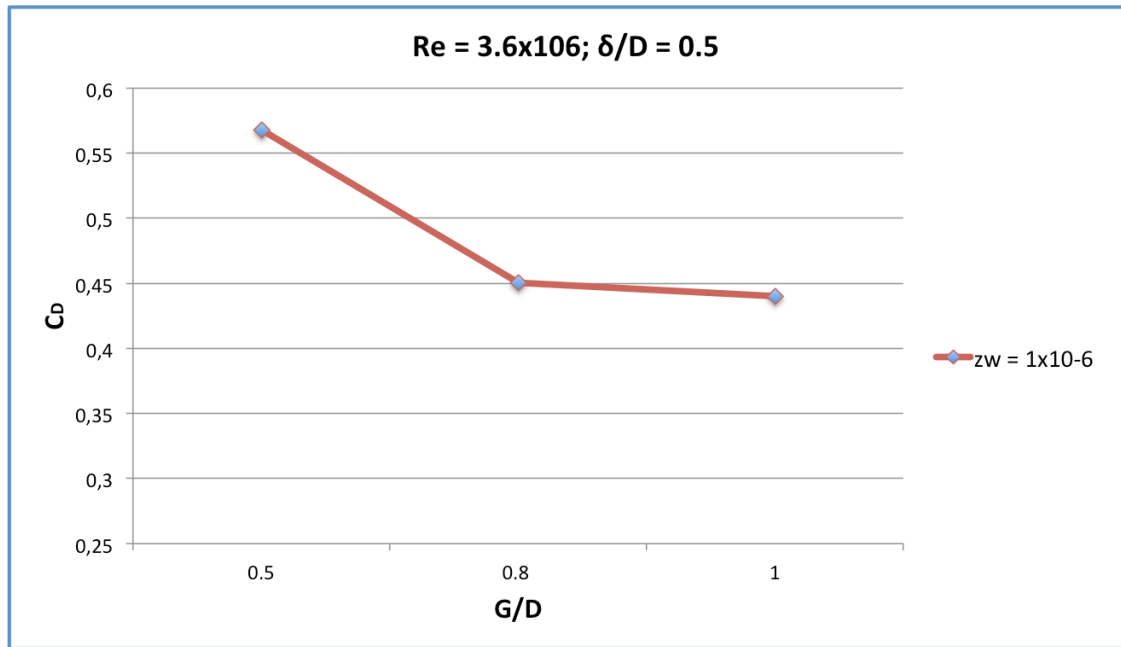


Figure 4.7. Time-averaged drag coefficient versus gap-to-diameter ratio

Table 2. Numerical results and experimental data at $Re = 3.6 \times 10^6$

| Re | Description | | C_D | C_L | St |
|--|-------------------------------|--|-----------|-----------|-----------|
| 3.6×10^6 (Upper-transition regime) | G/D=1 | Present numerical simulation | 0.4402 | 0.0344 | 0.2712 |
| | Flow around circular cylinder | Ong, M.C. (2009)[21] | 0.4573 | 0,0364 | 0.3052 |
| | | Ong, M.C at al. (2010)[14] | 0.4608 | 0.0342 | 0.3052 |
| | | Published experimental data (Zdravkovich 1997)[18] | 0.36-0.75 | 0.06-0.14 | 0.17-0.29 |

The lift coefficients C_L versus G/D at $Re = 3.6 \times 10^6$ with $\delta/D = 0.5$ are depicted on figure 4.8. At this graph we can see a same dependence as C_D , G/D increase C_L decrease.

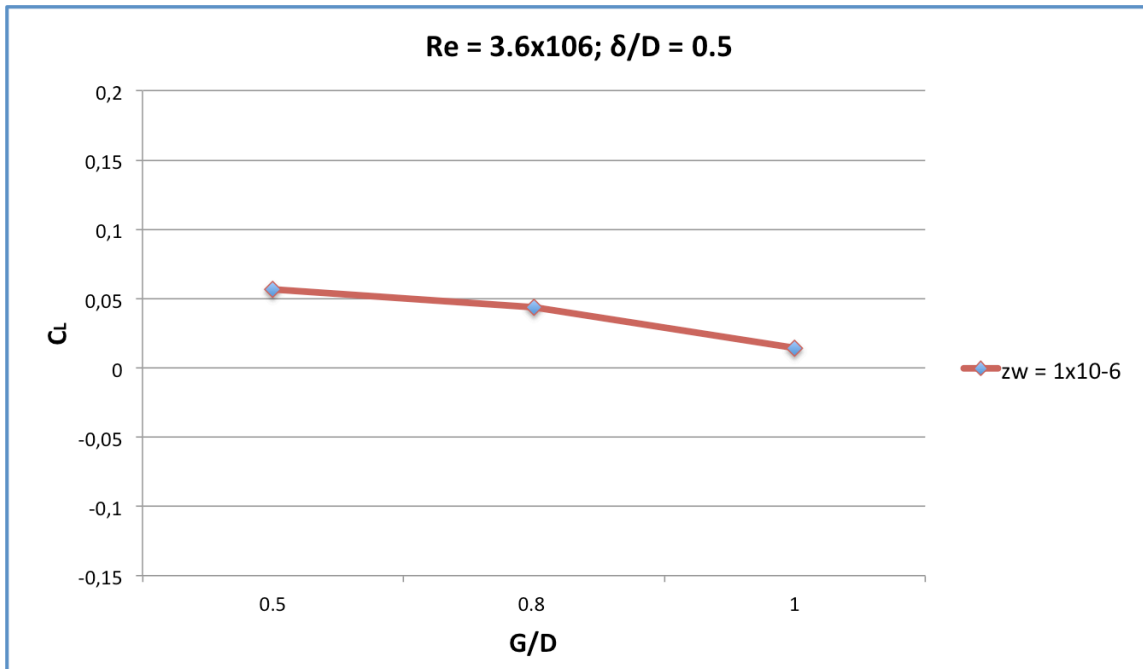


Figure 4.8. Time-averaged lift coefficient versus gap-to-diameter ratio

On the next step let us analyze the Strouhal number St versus G/D at $Re = 3.6 \times 10^6$ with $\delta/D = 0.5$ for $z_w = 1 \times 10^{-6}$. At figure 4.9 values of St versus G/D are demonstrated. At first sight that plane wall roughness does not have influence St . To observe any effects from plane wall roughness on the Strouhal number, the first one has to be high [14]. As we can see the Strouhal number for cases $G/D = \{0.5; 0.8; 1\}$ increases lightly as G/D increases. Assuming the vortex shedding is developing from a repressed phase to a completely developed phase as the impact of the plane bottom is decreasing. It seems that the pressure coefficient around the cylinder body symmetrical about the horizontal axis of the body. The numerical results quite similar with [21] results, however, there are slight differences in some parts of the cylinder.

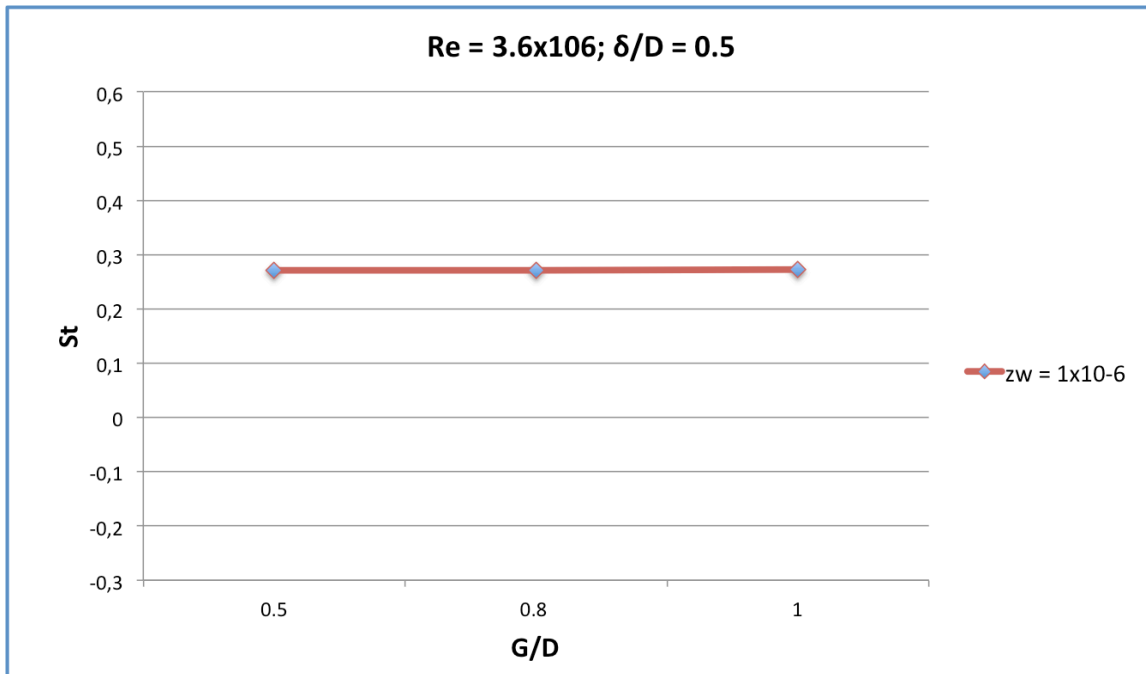


Figure 4.9. Srouhal number versus gap-to-diameter ratio

Therefore, the pressure distribution ($C_p = \frac{p_c - p_\infty}{0.5\rho U_\infty^2}$) around cylinder body close to the plane wall with same values of Reynolds number, roughness and δ/D for the case $G/D = 1$ are demonstrated on a figure 4.10. Where p_c is the pressure at the circumferential angle of the cylinder. The angle Θ was measured by clockwise from the front point on a horizontal axis of the cylinder. The results of a case $G/D = 1$ on this figure compare with numerical results of [21]. This error can be explained by the fact that in the present study and in the results of [21],[14] were used different geometry of grids and boundary layer thickness to diameter ratio ($\delta/D = 0.48$ – [21]; $\delta/D = 0.5$ – present study). This creates difficulties in modeling the strong pressure gradient accurately as [21] has done it. All following pressure distribution will show for lower shear layer only because observation from [14] registered that pressure in the upper shear layer vicinity changes slightly.

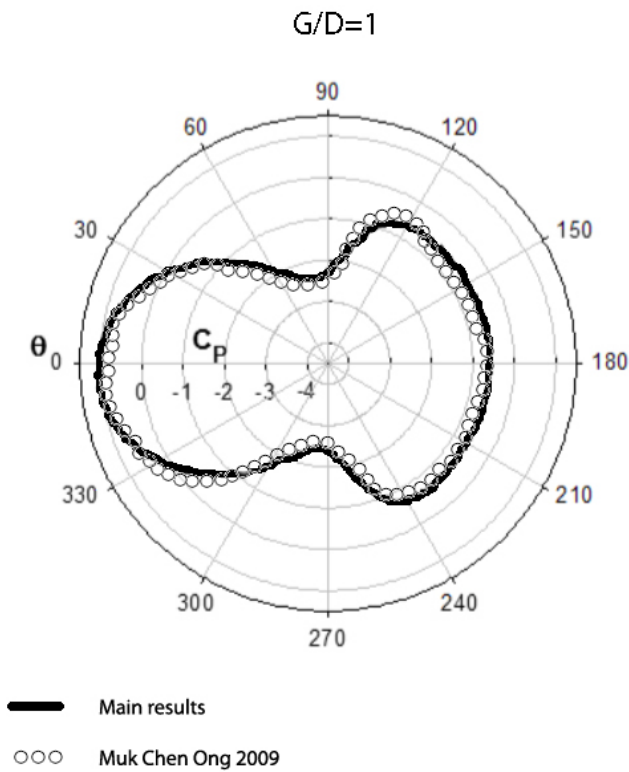


Figure 4.10 Mean pressure coefficient around the cylinder body $G/D = 1$

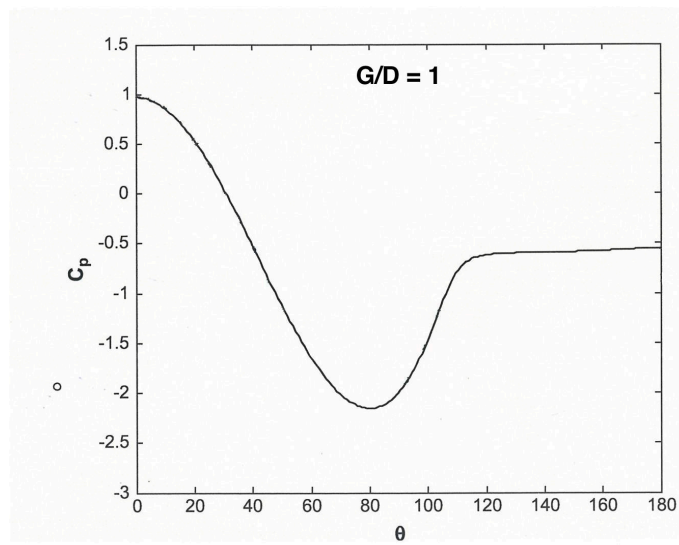


Figure 4.11 Mean pressure coefficient around the cylinder body $G/D = 1$

Figure 4.11 gives overview of the pressure distribution for lower shear layer only. The following analyses will present in 180° coordinate system.

The pressure distribution in case $G/D = 0.8$ close to the plane wall with $z_w = 1 \times 10^6$ for lower shear layer is shown in figure 4.12. We can see a small difference comparisons with the numerical results for $G/D = 1$. It appears that here is a small magnitude negative C_p at $\theta = 80^\circ$. This is explained the fact that with decreasing distance between the bottom wall of the cylinder and the plane wall pressure in the space is increased, which created by the fluid flow.

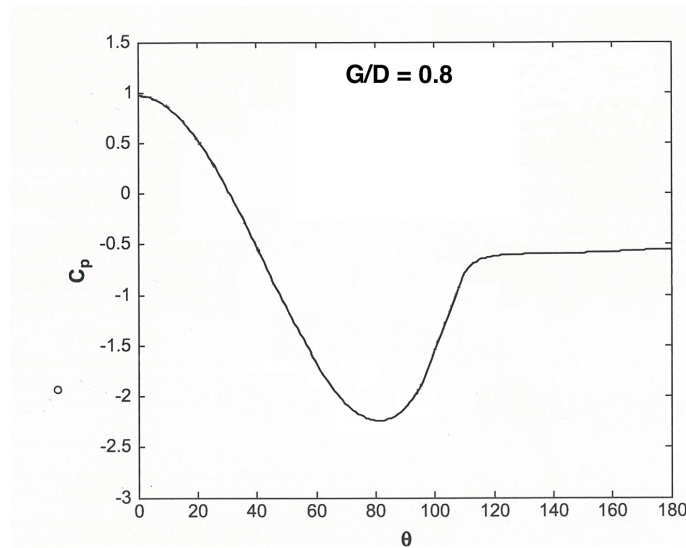


Figure 4.12 Mean pressure coefficient around the cylinder body $G/D = 0.8$

At the figure 4.13 the pressure coefficient for a case $G/D = 0.5$ for $Re = 3.6 \times 10^6$ with $\delta/D = 0.5$ for $z_w = 1 \times 10^6$ is depicted. The negative C_p (suction) at the gap ($\theta = 80^\circ$) keeps significant, and finally induces the downward force acting on the cylinder larger, the velocity at the gap slows down, and the intake at the gap

becomes less negative. As G/D increases, the impact of the bed reduce, and consequently C_p gets symmetric as shown in Fig. 4.10 for $G/D = 1$. The strength of the net upward lift force is decreased and approaches zero as G/D approaches infinity.

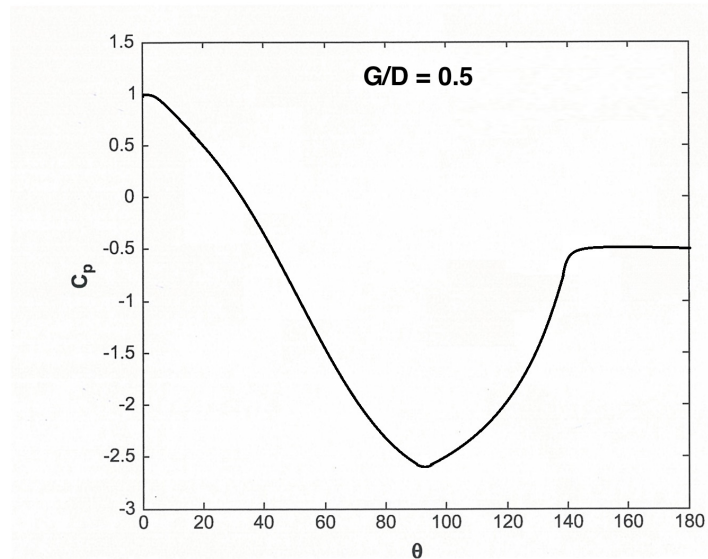


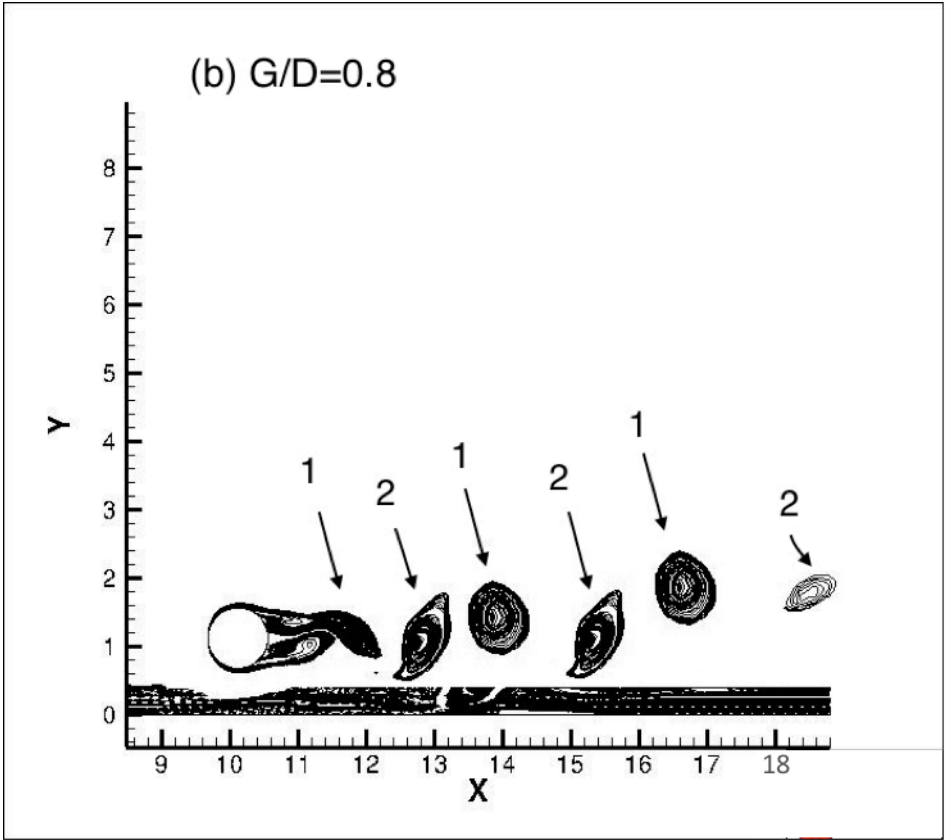
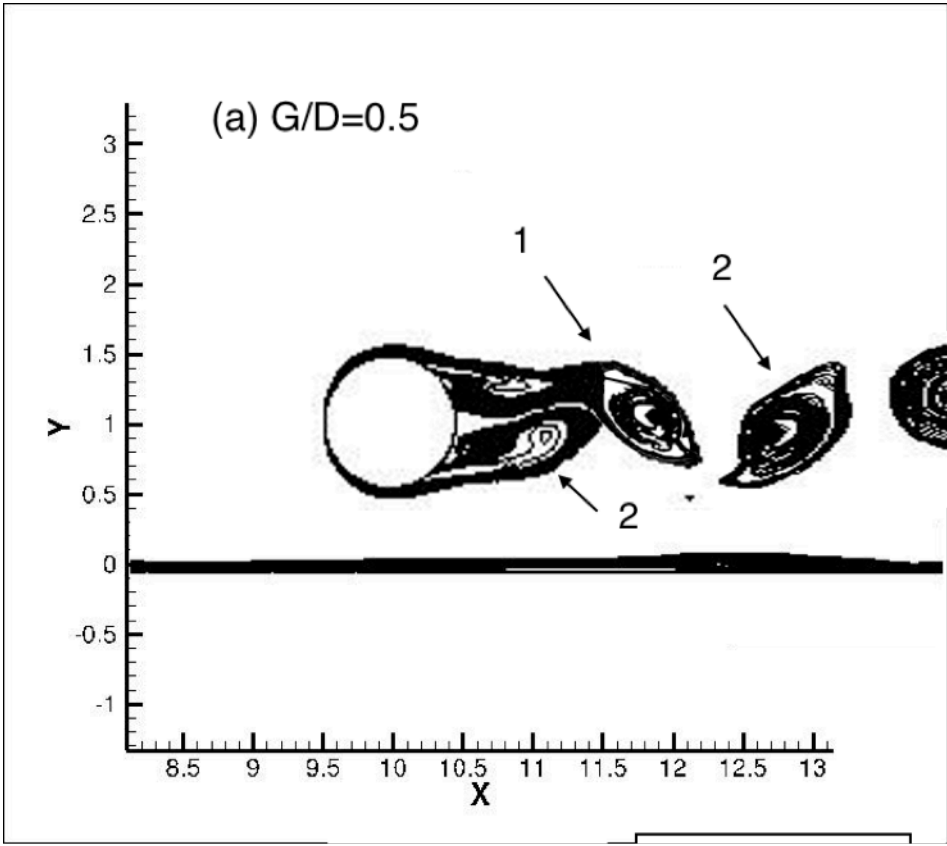
Figure 4.13 Mean pressure coefficients around the cylinder for $Re = 3.6 \times 10^6$ with $\delta/D = 0.5$ for $z_w = 1 \times 10^{-6}$ and $G/D = (0.5; 0.8; 1)$

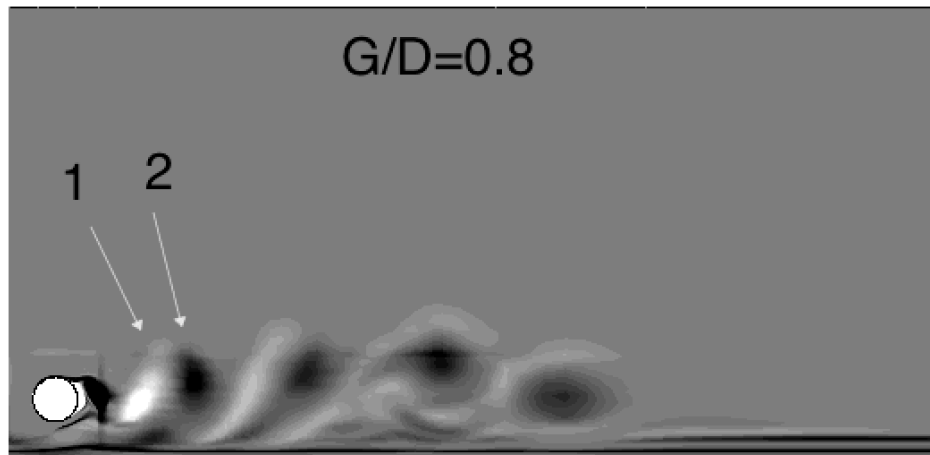
4.4 Vorticity contours.

Figure 4.13 gives visualization of instantaneous vorticity contours of flow around cylinder bodies for flow at $Re = 3.6 \times 10^6$ with $\delta/D = 0.5$ and $G/D = [0.5; 0.8; 1]$ close to the plane wall with $z_w = 1 \times 10^{-6}$ for non-dimensional time $200D/U_\infty$. Number 1 indicates on positive vorticity (counter-clockwise) and number 2 indicates negative vorticity (clockwise). There are two shear layers of the

vicinity of the circular body.

For $G/D = 0.5$ which is showed in figure 4.14(A) the trailing wake encounters with the front wall of the cylinder, then this flow goes around the cylinder and behind the cylinder vortex shedding continues to develop. The vortices with positive vorticity evolve from the lower friction layer and the lower friction layer the vortices with negative vorticity evolve too. For $G/D = 0.8$ and $G/D = 1$ (figures 4.14 (B) and 4.14(C) respectively) the vortex shedding is similar to each other, behind from high gap-to-diameter ratio. For all complexion gap-to-diameter ratios, the strongest vortices are detected in the separated shear layer and along the cylinder sides. Non-slip conditions of the cylinder walls influence vortices development. The vortex flow is similar to the Numerical simulation of flow around a circular cylinder close to a flat seabed and flows around isolated circular cylinder (see [14],[21]) on three occasions the vortex shedding is generated identically.





(c) $D/G=1$

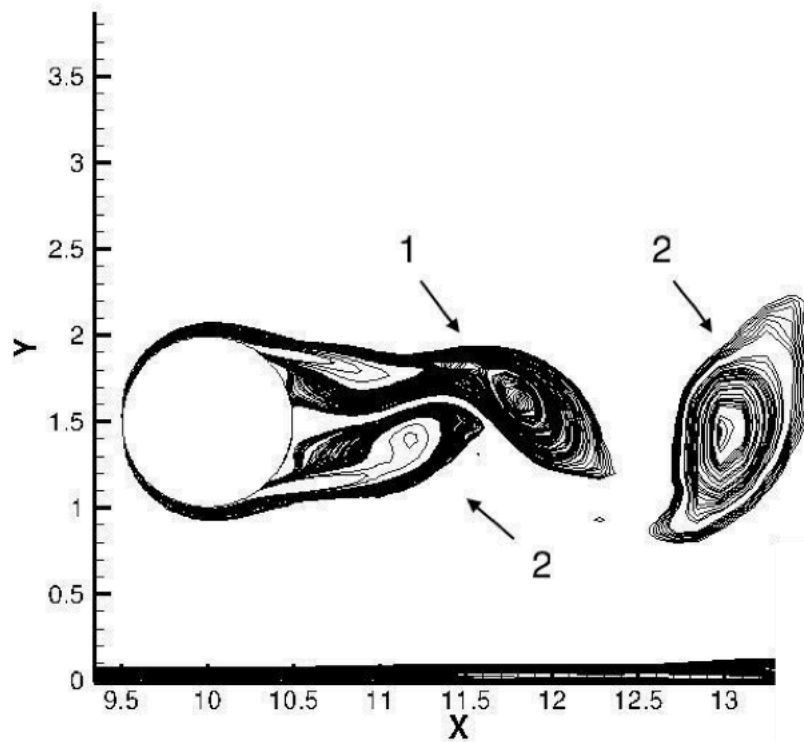


Figure 4.14. The development of vortex shedding shown by instantaneous non-dimensional vorticity counter plots for $Re = 3.6 \times 10^6$, $\delta/D = 0.5$ for $z_w = 1 \times 10^{-6}$ at non-dimensional time of $200D/U_\infty$.

4.5 Streamlines

Instantaneous streamlines over the single cylinder with a schematic overview of the mean flow structures are shown in figure 5.10. As the shear layer gets separated at the upper shear layer and lower shear layer respectively, the main vortex is formed past the cylinder. Reattachment occurs behind the cylinder from both shear layers upper and lower, respectively, and reversed flow in the wake is generated.

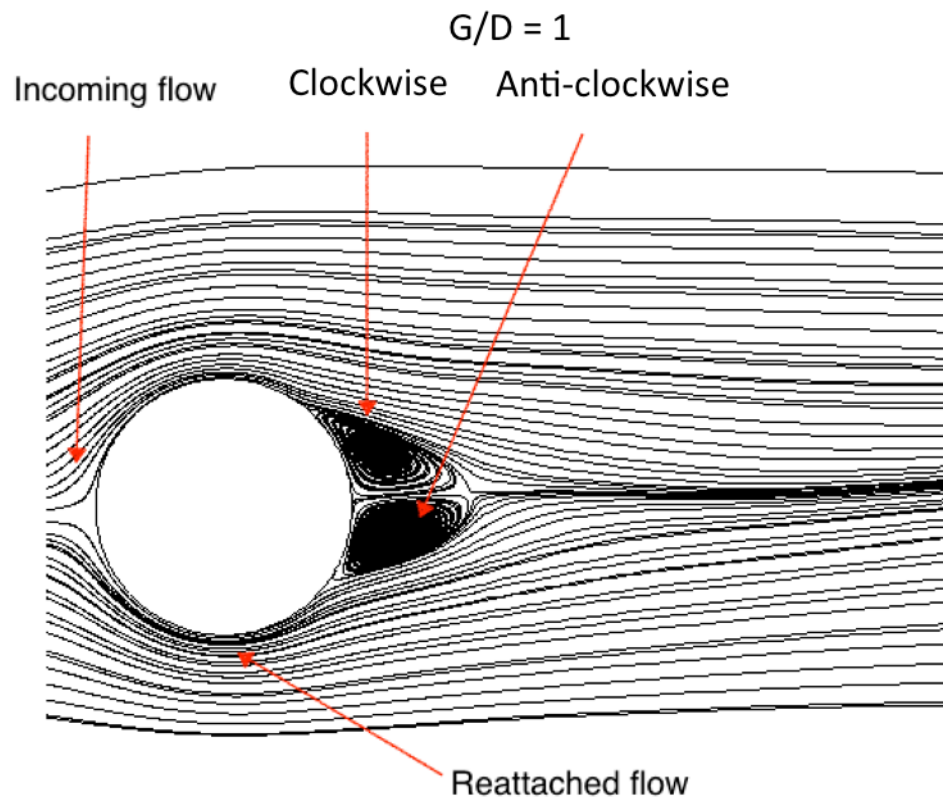


Figure 4.15. Schematic overview of mean flows structure for a case $G/D = 1$

The streamlines from each cylinder are taken at the time moment $200D/U_\infty$, as for the vorticity contours in figure 4.14. The distance from the cylinder to the end of the figure is $10D$.

Both negative and positive vortices acting on the circular body extend downstream and upstream of the circular body sides, respectively. Consequently, no reattachment is present. While an asymmetry of the vertices around the cylinder is present for the $G/D = 0.5$ case, but for others, both cases symmetry is present for both negative and positive vorticity. These vortices are covering behind the cylinder, on the rear side of the circular body. The vortices are cut at the end of the cylinder, as illustrated by the black line in figure 4.16. Consequently of the symmetry and both vortices length, the lift force acting on the cylinders is canceled out.

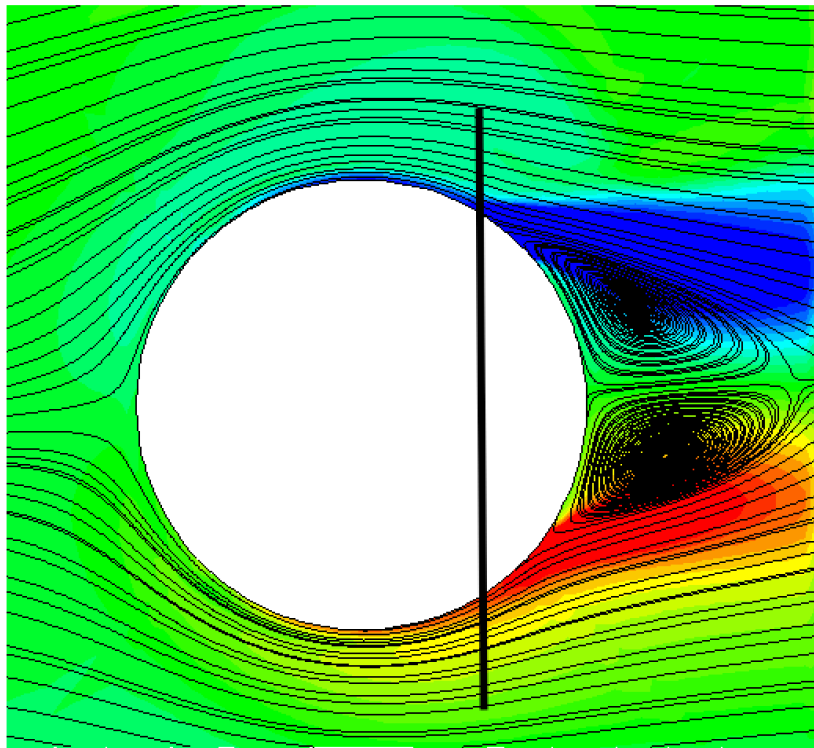
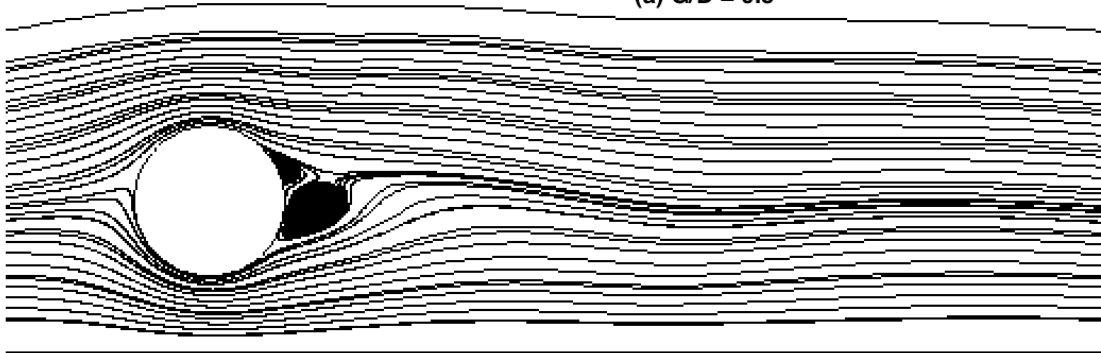


Figure 4.16. Symmetry in vortices around cylinder for $G/D = 1$

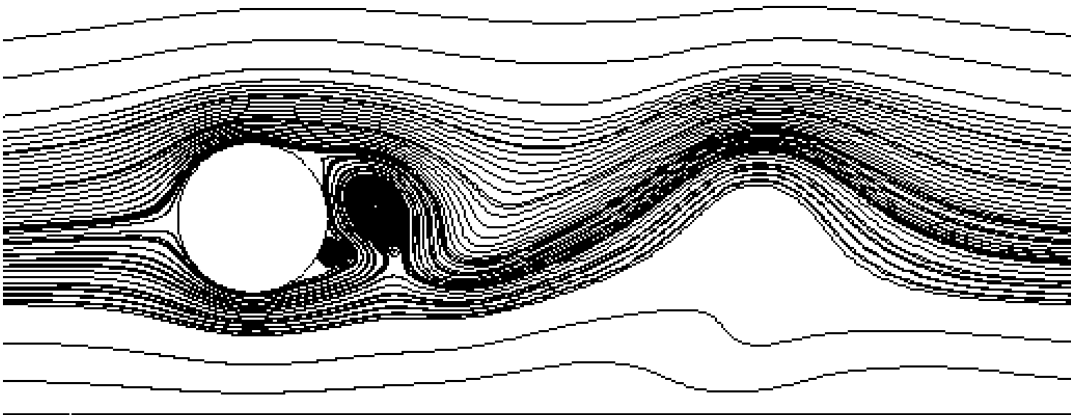
At the figure 4.17 are shown instantaneous streamlines for three cases $G/D = 0.5; 0.8; 1$. The fluctuation of the vortex wake is highest for the gap-to-diameter ratios 1 and 0.8. As the gap-to-diameter ratio decrease, the vortex wake gets flattered. This agrees with the length of the vortex wake seen in figure 4.17.

As reported earlier different behavior is observed for the Strouhal number. This is induced by the reattachment of the separated shear layer. The remaining length or diameter of the cylinder downstream of the location of reattachment is not an identical to the diameter of the cylinder. Both cases $G/D = 1$ and 0.8 have similarity in instantaneous streamlines. But for $G/D = 0.5$ by the action of the plane wall on the lower shear layer, vortex formation can be traced not so clearly.

(a) $G/D = 0.5$



(b) $G/D = 0.8$



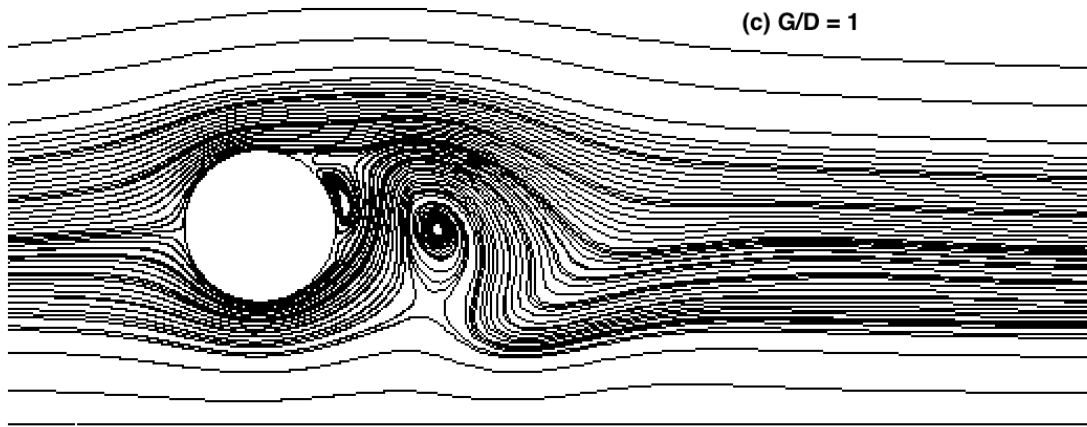


Figure 4.17. Instantaneous streamlines at $200D/U_\infty$ for circular cylinder with gap-to-diameter ratios $G/D = 0.5; 0.8; 1$.

Chapter 5

Conclusion for flow around the single cylinder.

The flow with high Reynolds number around a two-dimensional smooth circular cylinder close to the plane wall ($Re = 3.6 \times 10^6$ for $\delta/D = 0.5$ $z_w = 1 \times 10^{-6}$) has been calculated using two-dimensional Reynolds-Averaged Navier-Stokes equations. This Reynolds number covering the supercritical to upper-transition flow regime. Three different gap-to-diameter ratios $G/D = 0.5; 0.8; 1$ are applied. The main results have been compared with [21] and [14] numerical simulations. At the present study, vortices are observed in three cases. The vortices with positive vorticity evolve from the upper friction layer and the lower friction layer the vortices with negative vorticity evolve too.

The main results are the drag coefficient C_D increases with decreasing a gap,

the lift coefficient C_L increases with decreasing a gap and distinct mean lift, clearly seen in a direction away from the plane bottom at $G/D = 0.5$. The Strouhal number does not change for all cases, this is observed as long as vortex shedding occurs. The drag and lift coefficients different between the biggest and the lowest gap-to-diameter ratios in the present study are 22.51%, 39.32% respectively. There is abundant evidence that with decreasing gap-to-diameter ratios both drag and lift coefficient increase and if we observed a pressure distribution around cylinder while numerical simulations the pressure coefficient increase with decreasing gap-to-diameter ratios too.

The number of cells in computational domain is of fundamental importance for numerical simulations. Different numbers of cells of the grid could be given a different result. The grid has to include a sufficient number of cells, because we can compute our models only in large grids, but to get the same results, in comparison with small grids, but spend more time.

Chapter 6

Numerical set-up

This chapter explains the domain, mesh, boundary conditions and numerical boundary layer used. The same domain and boundary conditions are applied for all simulations while gap-to-diameter ratios and length-to-diameter ratios for the tandem cylinders are changed to get different results.

6.1 Numerical solution procedure, computational domain and boundary conditions

The RANS simulations are performed on the two-dimensional quadrangle computational domain extending from 10D in front of the upstream cylinder center to 30D behind to the downstream cylinder. The height of the domain is 10D extending from a bottom to a top. Both cylinders have diameters of $D = 1$ meter. The top inlet and outlet of the domain are boundaries that shall represent an infinite fluid domain. The present boundary conditions have a similarity with boundary in the first part of the present study. At figure 6.1 is shown the 2D slice of the computational domain with boundary conditions and parameters. The velocity is given as vector $U = (U_1 \text{ and } U_2)$. In inlet region velocity vector is a fixed value, but velocity vector $U = (U_1(Y), U_2(\theta))$ it means that there is only flow in the x-direction. The pressure is a scalar value and has no specific direction. In inlet region pressure is equal to zero. This satisfies the requirement that there should be no drastic changes close to the inlet (or any other boundaries) such that the boundary will affect the flow parameters considerably.

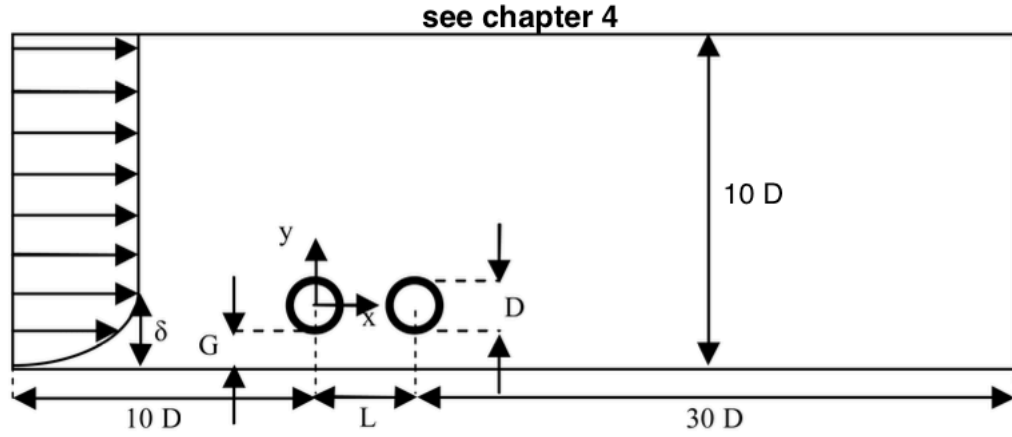


Figure 6.1. Definition sketch for the tandem cylinders in the vicinity of a plane wall; in the present study $L/D = 2, 3, 3.5$; $G/D = 1, 0.8, 0.5$

In outlet region all parameters marked as free, it means these unknowns will be computed while simulation is going

The boundary conditions of the computational domain a follow as:

A boundary layer flow for inlet figure 13

$$u_1(Y) = \min \left\{ \frac{u_*}{k} \ln \left(\frac{Y}{z_w} \right), U_\infty \right\} \quad (6.1)$$

$$u_2(Y) = 0 \quad (6.2)$$

$$k(Y) = \max \left\{ C_\mu^{-1/2} \left(1 - \frac{Y}{\delta} \right)^2 u_*^2, 0.0001 U_\infty^2 \right\} \quad (6.3)$$

$$\varepsilon(Y) = \frac{C_\mu^{3/4} k(Y)^{3/2}}{\ell} \quad (6.4)$$

$$\ell = \min \left\{ kY \left(1 + 3.5 \frac{Y}{\delta} \right)^{-1}, C_\mu \delta \right\} \quad (6.5)$$

Where Y is the wall normal direction beginning from the plane wall (see figure

2.2) and ℓ is an estimate of the turbulent length scale. $u_* = \frac{kU_\infty}{\ln(\delta/z_w)}$ is the friction velocity and $k = 0.41$ is the von Karman constant.

- Boundary near-wall conditions are included k and ε values. It should be applied for both plane bottom (sea bottom) and both cylinders walls [27] as

$$k = \frac{u_*^2}{\sqrt{C_\mu}} \quad , \quad \varepsilon = C_\mu^{\frac{3}{4}} \frac{k^{\frac{2}{3}}}{kh_p} \quad (6.6)$$

Here h_p denotes is the radial distance between the wall to the first node (see figure 4.2) and u_* means the wall friction velocity received from the logarithmic law.

$$\frac{u_{tan}}{u_*} = \frac{1}{k} \ln\left(\frac{h_p}{z_*}\right) \quad (6.7)$$

Where the tangential velocity is u_{tan} , $z_* = (z_0, z_w)$ where z_0 the roughness parameter of the cylinder surface and z_w is a switch parameter for the wall roughness. In the present study, a small roughness $z_w = 1 \times 10^{-6}$ was used for the cylinder. The Reynolds number for all simulations is equal $Re = 3.6 \times 10^6$.

- In the outlet boundary conditions static pressure $p = 0$.
- No-slip boundary conditions on the plane wall and the cylinder, this means $u_1 = u_2 = 0$.
- The top of computational domain has to have a slip boundary conditions where $u_1 = U_\infty$ and $u_2 = 0$ since the top wall located sufficiently far away from the cylinder and the plane bottom
- Front and back surfaces are empty to convert our computational domain from 3D model to 2D.

6.2 Mesh

The domain is discretized in structured blocks mesh with of a body fitted square mesh around both cylinders and rectangular mesh outer parts of the domain. The mesh consists of quadrangle elements. For manipulate and controls of sizes of the circulars cylinders throughout the domain, squares (cylinder`s boxes) have been chosen. As mentioned earlier the first node thickness has to be in range 30-45. A grid should be structured with a good transaction between each element; it is important to have a gradual transition of the size to avoid numerical instabilities. There are not significant differences in the construction of grids for cases with $G/D = 1$ and 0.8 (see Figures 8.2 and 8.3). The additional block between cylinder`s boxes and a plane wall make gap-to-diameter ratios for these cases. As is evident from Figures 8.2 and 8.3 the main difference between meshes for cases $G/D = 1$ and $G/D = 0.8$ is high of the additional block.

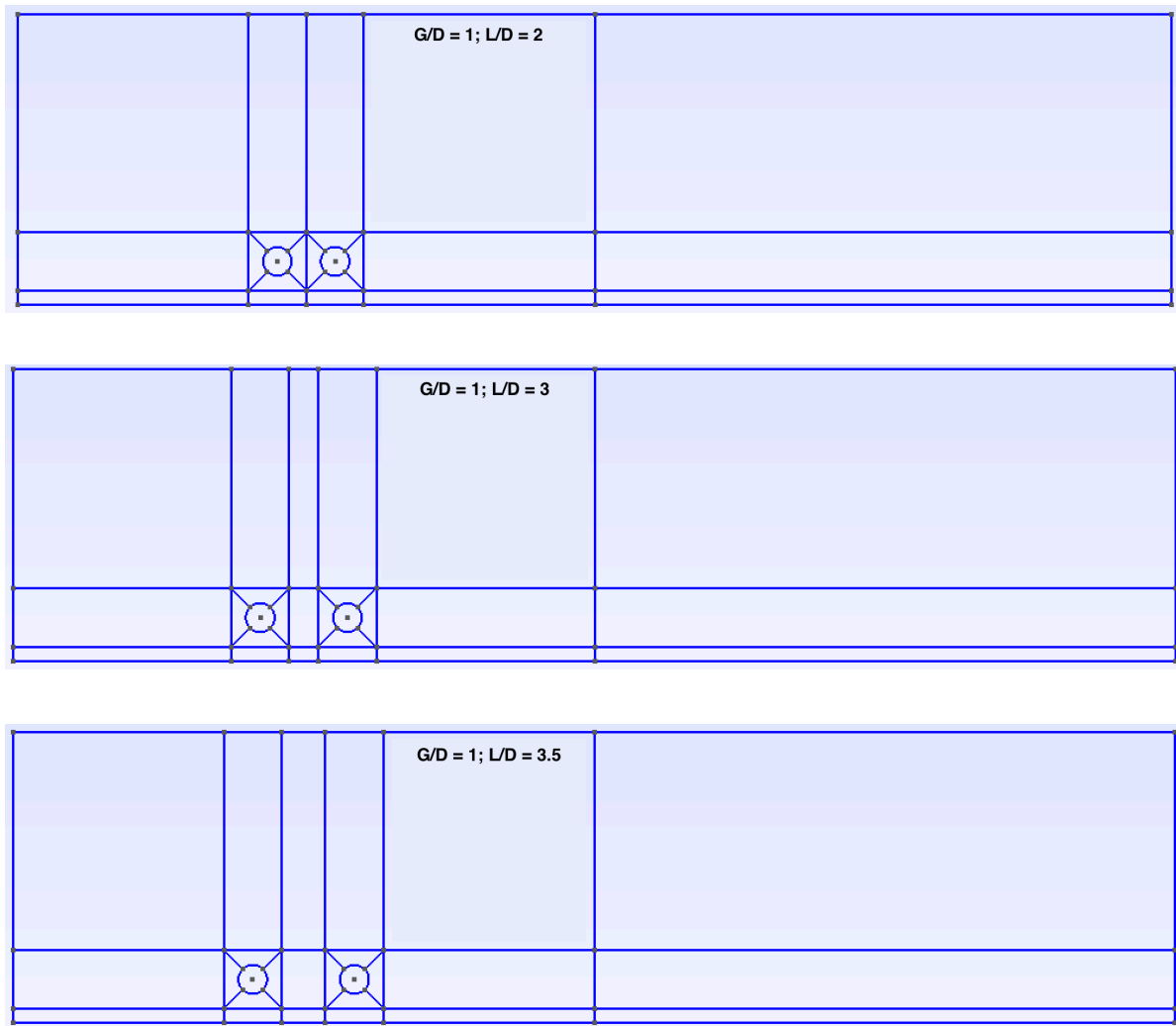


Figure 6.2. Meshes for cases with $G/D = 1$.

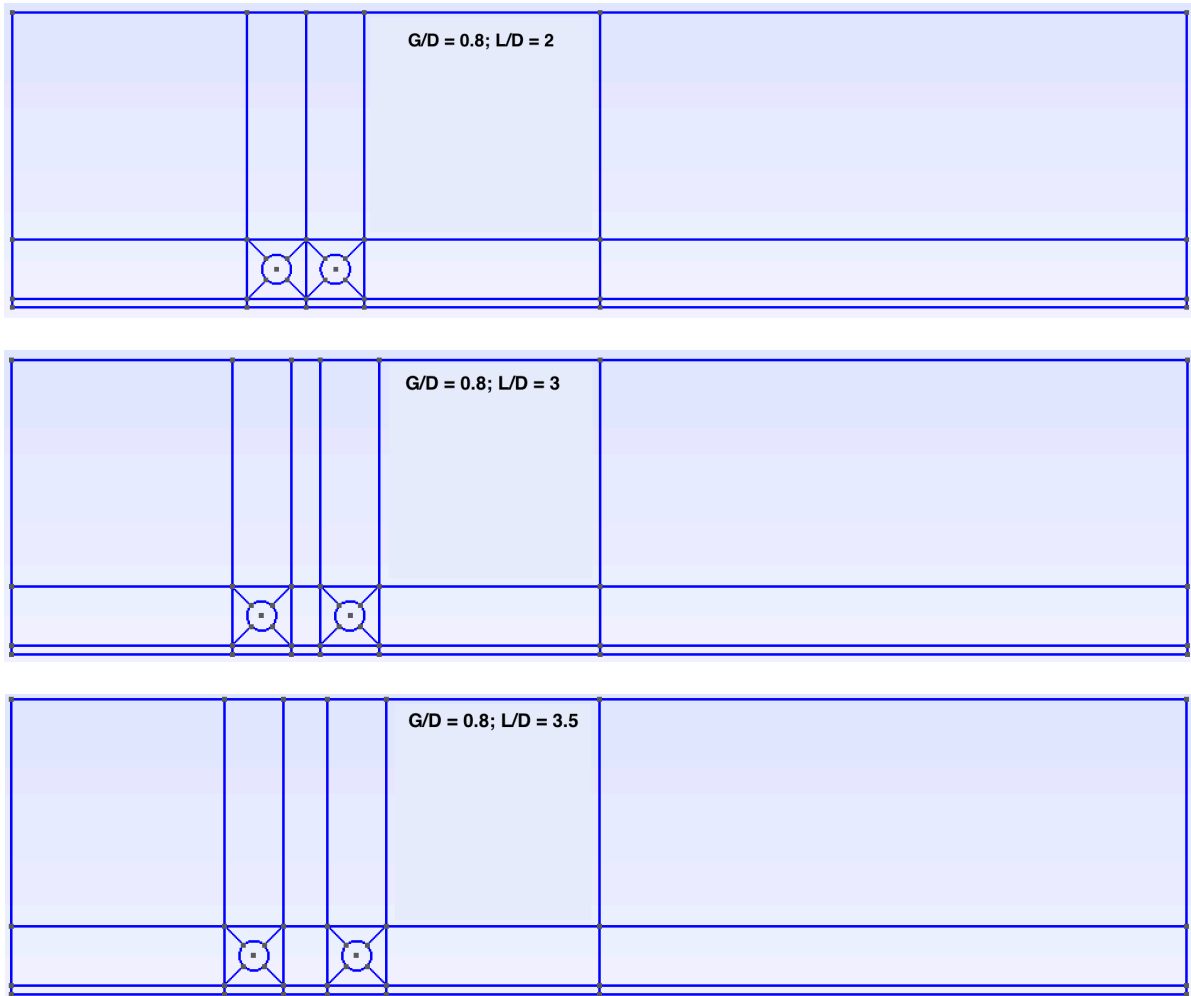


Figure 6.3. Meshes for cases with $G/D = 0.8$.

As concerning case with par-to-diameter ratio $G/D=0.5$, there is a slight difference in mesh construction. The main different is the absence of an additional block below cylinder's boxes, but an absence of the additional block, a direct impact on first node thickness. Creating a line between the plane bottom and a cylinder box solved this problem as an example $L/D = 3$ is shown (see figure 6.4). It constructed and shown for three cases respectively (see figure 6.5)

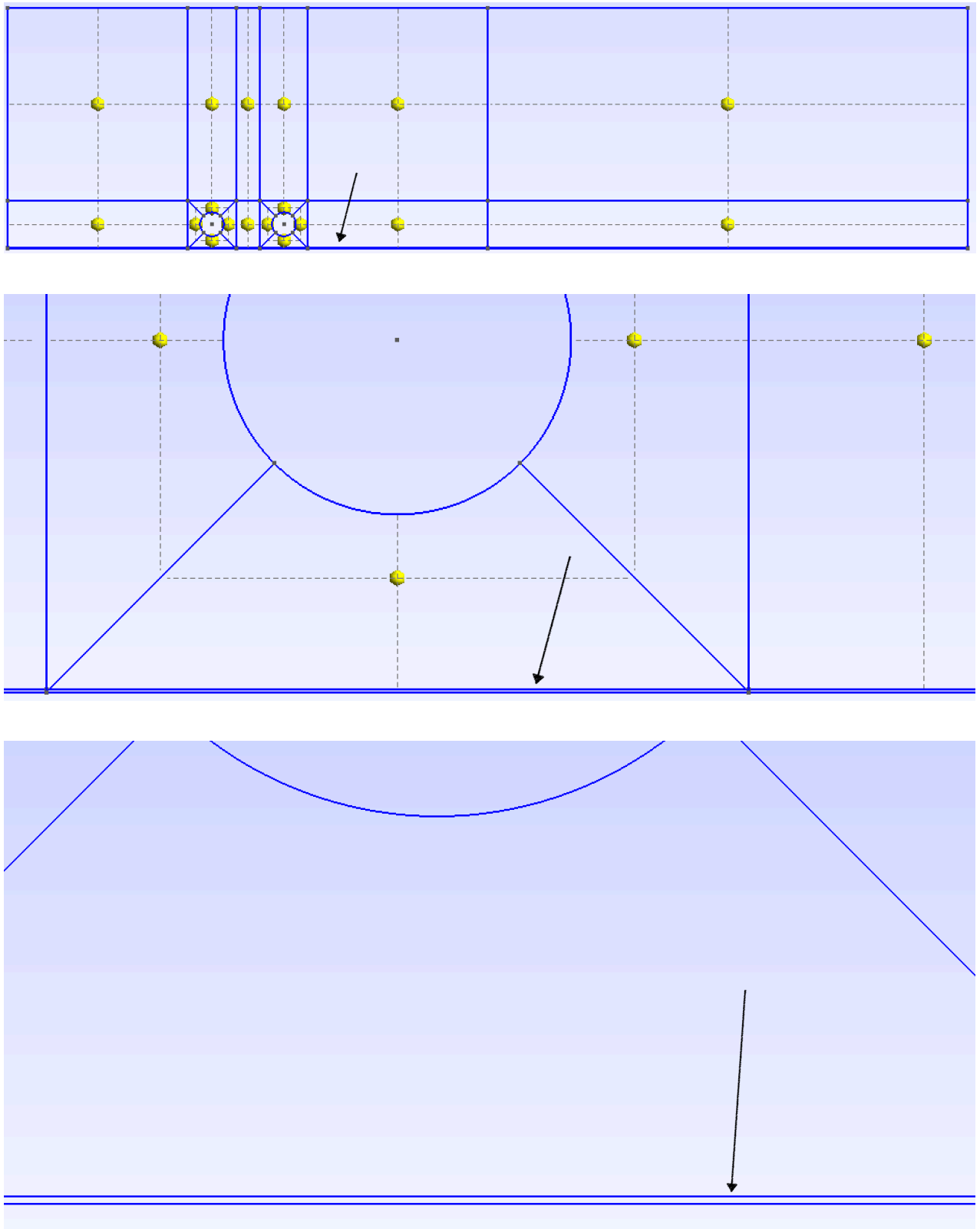


Figure 6.4. Demonstration of an additional line on example of case $L/D=3$

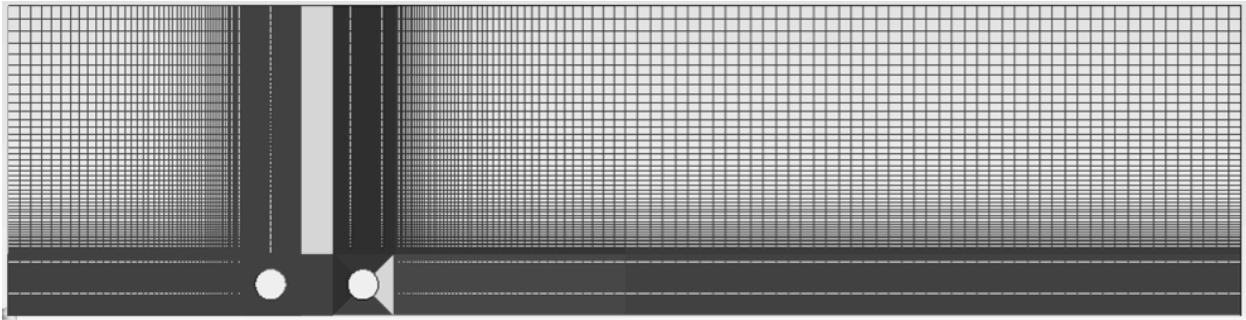


Figure 6.6. Global mesh for a single cylinder case at $G/D=0.5$ and $L/D=3$.

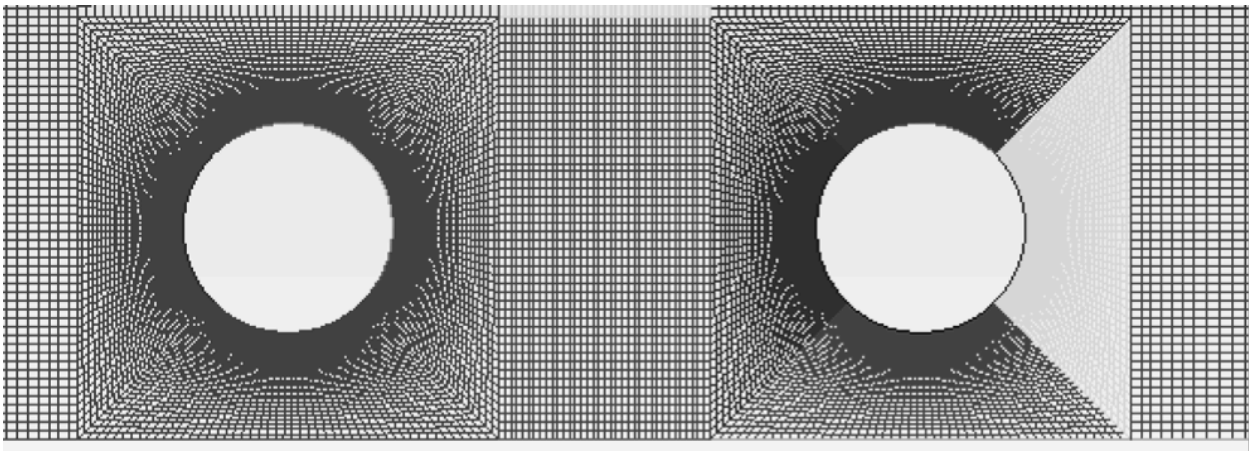


Figure 6.7. Local mesh for tandem cylinders at $G/D=0.5$ and $L/D=3$.

The figures 6.6 and 6.6 show the final grid for tandem cylinders at $G/D = 0.5$ $L/D = 3$. As shown on both figures, this grid has a good transaction between each element of the grid and well structured, especially the plane wall and around both cylinders walls. Figure 6.5 gives three meshes for full $G/D = 0.5$ cases.

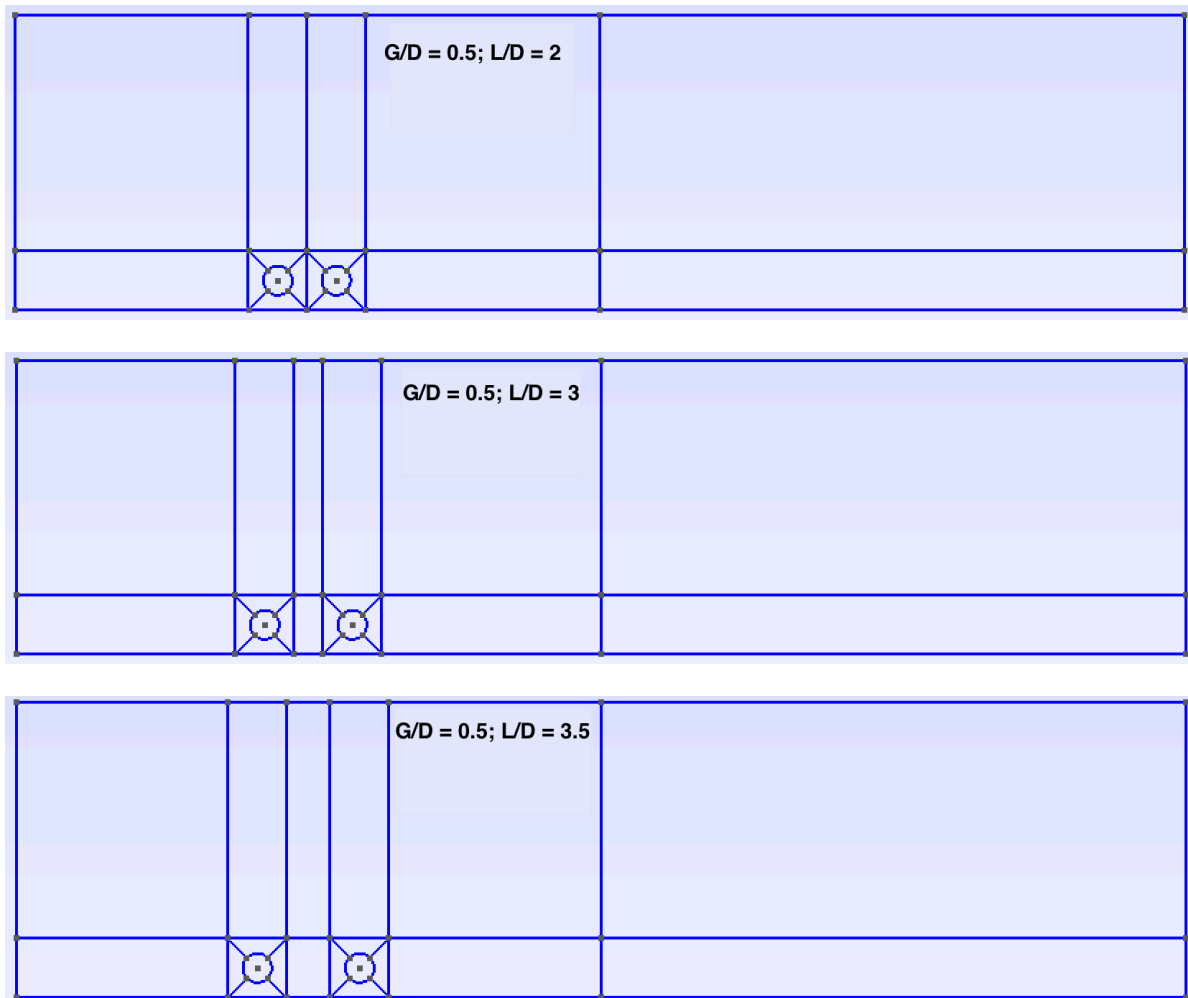


Figure 6.8 Meshes for cases with $G/D = 0.5$.

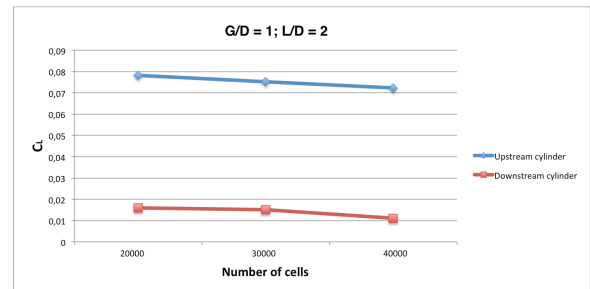
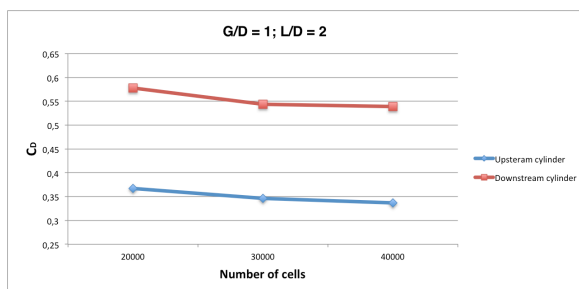
6.3 Convergence studies

As mentioned in chapter 4 for selecting the optimal number of cells in each grid model must first count in small quantities in cells, then incrementally increased each identical grid and until a difference between the computed results at

a higher grid and small grid will be note more than 5%. It has been done for both single cylinder cases and tandem cylinders cases by the same way.

Both mesh and time-step convergence studies have been fulfilled for flow at $Re = 3.6 \times 10^6$ (upper-transition flow regime) for cases of $\delta/D = 0.5$, $G/D = (0.5; 0.8; 1)$ and $L/D = (2; 3; 3.5)$. The fluctuations of drag and lift coefficients are obtained in both mesh and time-step convergence studies. Here C_D and C_L are computed based on determinations $F_D = 0.5DC_D U_\infty^2$ and $F_L = 0.5\rho DC_L U_\infty^2$, here F_D and F_L are the time-averaged integrated horizontal and vertical forces per unit length, respectively, acting on the both cylinders upstream and downstream. F_D and F_L are obtained directly from the pressure distribution and shear stress distribution around both cylinders. The fluctuation of F_D and F_L between two successive grids might be kept within 5%. At the figures 6.9, 6.10 and 6.11 - convergence study for all tandem cases are depicted. Detailed results of the grid convergence studies are enumerated in table 3.

Three grids with approximately 20000, 30000 and 40000 elements are used to perform the grid convergence study. All results, which obtained from three grids, were compared between each other for each case. For example, by comparing the numerical results of the grids with approximately 30000 and 40000 cells C_D varies from 0.94% to 2.53% and C_L varies from 0.88% to 4.35%. (see figures 6.9; 6.10; 6.11 and table 3)



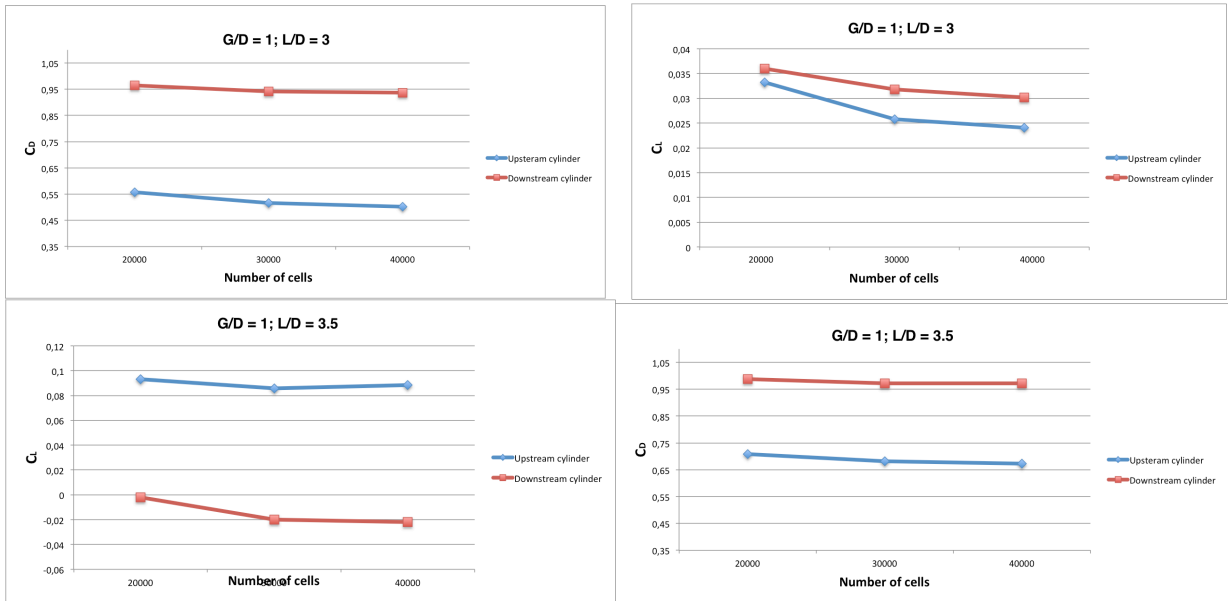


Figure 6.9. The grid convergence study $G/D = 1, L/D = (2; 3; 3.5)$

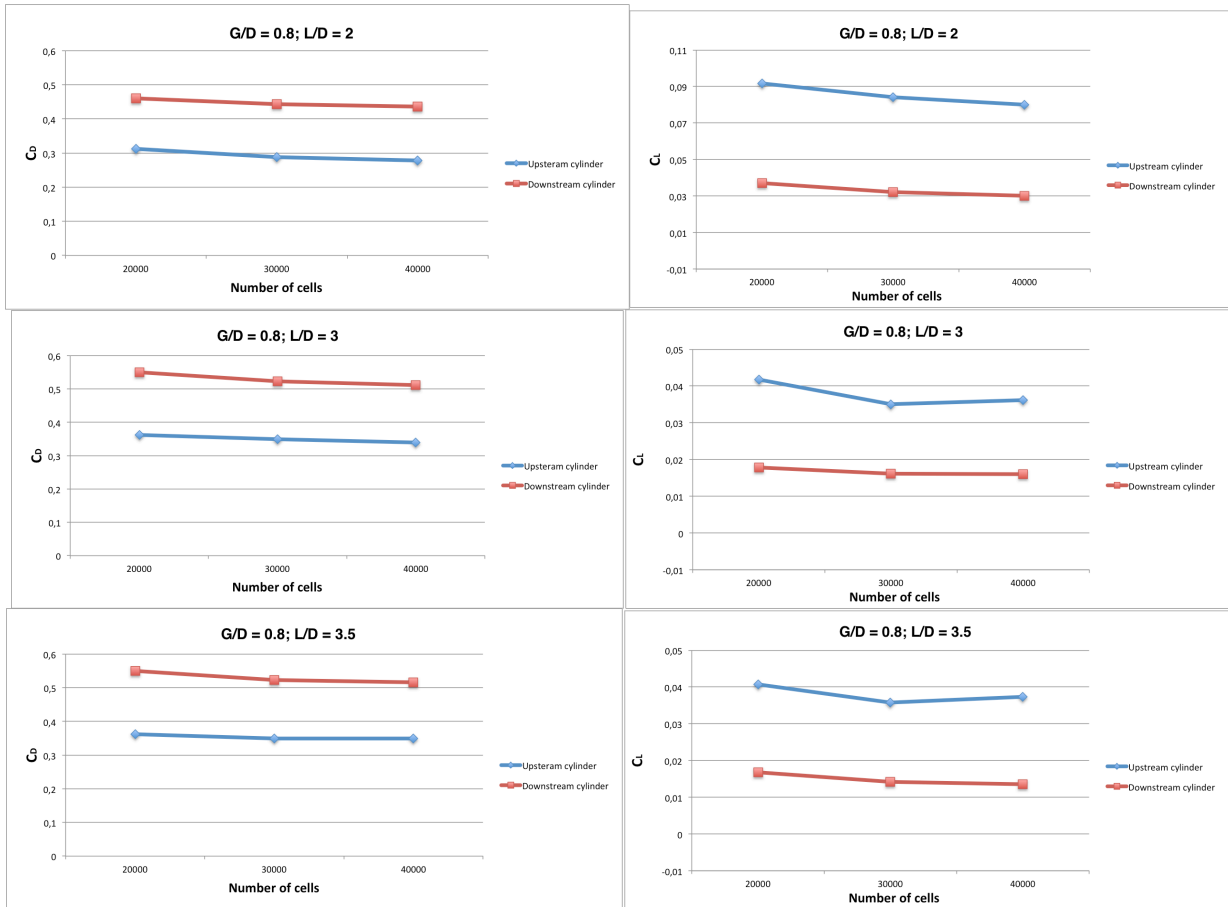


Figure 6.10. The grid convergence study $G/D = 0.8, L/D = (2; 3; 3.5)$

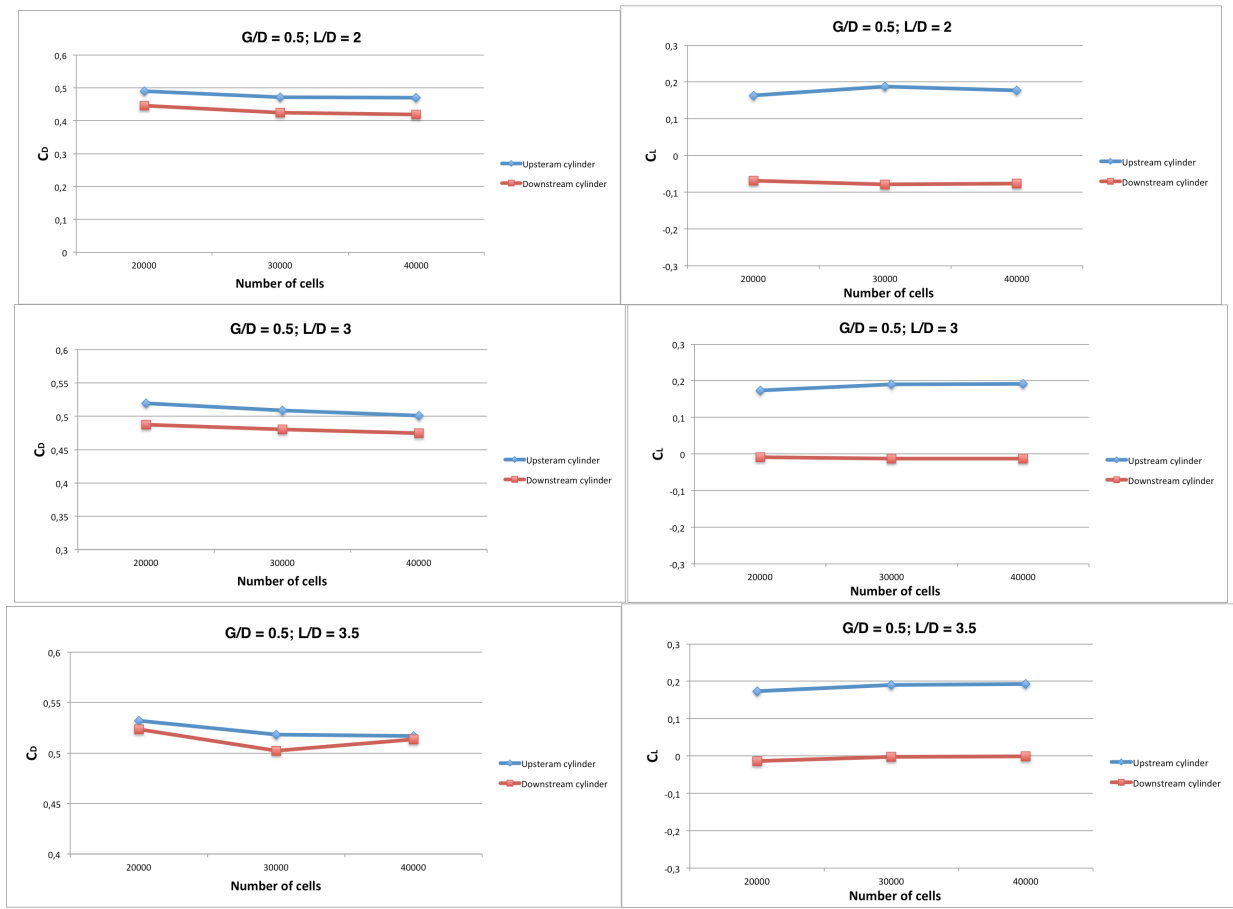


Figure 6.11. The grid convergence study $G/D = 0.5$, $L/D = (2; 3; 3.5)$

Consequently, the grids with relatively 40000 cells are considered to give an adequate mesh determination. The radial distance to the first node from the cylinder surface and plane bottom is $0.0005D$. The present study has been performed with non-dimensional time step (Δt) of $0.0002D/U_\infty$ and simulations have run at 200 non-dimensional time units (D/U_∞). But when a number of cells increase it could be a cause of decreasing of time-step, therefore these cases have been calculated with a reduced time-step (Δt) of $0.0001D/U_\infty$ using the mesh from the grid convergence studies. The final results were taken from numerical results computed on grids with 40000 cells. As reported before these grids give more accuracy results.

Table 3. Results from grid convergence study for the tandem cylinders with gap-to-diameter ratio [0.5; 0.8; 1] and pitch distance [1; 2; 2.5].

| <i>G/D</i> | <i>L/D</i> | Number of elements | Time step | C_{D1} | C_{D2} | C_{L1} | C_{L2} | St_1 | St_2 | |
|------------|------------|--------------------|-----------|----------|----------|----------|----------|--------|--------|--------|
| 1 | 2 | 20000 | 0.0002 | 0.3012 | 0.5161 | 0.0747 | 0.0124 | 0.2894 | 0.2684 | |
| | | 30000 | 0.0002 | 0.3293 | 0.5304 | 0.0731 | 0.0113 | 0.2894 | 0.2684 | |
| | | 40000* | 0.0001 | 0.3363 | 0.5387 | 0.0723 | 0.0111 | 0.2894 | 0.2684 | |
| | 3 | 20000 | 0.0002 | 0.4824 | 0.9190 | 0.0810 | 0.0389 | 0.2894 | 0.2531 | |
| | | 30000 | 0.0002 | 0.4989 | 0.9293 | 0.0767 | 0.0314 | 0.2895 | 0.2535 | |
| | | 40000* | 0.0001 | 0.5020 | 0.9369 | 0.0760 | 0.0301 | 0.2895 | 0.2536 | |
| | 3.5 | 20000 | 0.0002 | 0.6503 | 0.9432 | 0.9033 | 0.0255 | 0.3160 | 0.1939 | |
| | | 30000 | 0.0002 | 0.6694 | 0.9678 | 0.0895 | 0.0228 | 0.3163 | 0.1937 | |
| | | 40000* | 0.0001 | 0.6719 | 0.9720 | 0.0882 | 0.0220 | 0.3163 | 0.1938 | |
| | 2 | 2 | 20000 | 0.0002 | 0.2611 | 0.4229 | 0.0521 | 0.0349 | 0.2894 | 0.1984 |
| | | | 30000 | 0.0002 | 0.2702 | 0.4318 | 0.0493 | 0.0331 | 0.2894 | 0.1984 |
| | | | 40000* | 0.0001 | 0.2782 | 0.4360 | 0.0471 | 0.0320 | 0.2894 | 0.1984 |
| 3 | | 20000 | 0.0002 | 0.3238 | 0.4914 | 0.0374 | 0.0243 | 0.3371 | 0.2136 | |
| | | 30000 | 0.0002 | 0.3313 | 0.5084 | 0.0367 | 0.0235 | 0.3370 | 0.2135 | |
| | | 40000* | 0.0001 | 0.3390 | 0.5114 | 0.0362 | 0.0232 | 0.3370 | 0.2136 | |
| 3.5 | | 20000 | 0.0002 | 0.3332 | 0.4963 | 0.0389 | 0.0145 | 0.3409 | 0.1977 | |
| | | 30000 | 0.0002 | 0.3403 | 0.5096 | 0.0380 | 0.0137 | 0.3409 | 0.1977 | |
| | | 40000* | 0.0001 | 0.3489 | 0.5162 | 0.0374 | 0.0135 | 0.3409 | 0.1977 | |
| | | | 20000 | 0.0002 | 0.4571 | 0.4044 | 0.1787 | 0.0778 | 0.2894 | 0.1084 |

| | | | | | | | | | |
|------------|----------|--------|--------|--------|--------|--------|--------|--------|--------|
| 2.5 | 2 | 30000 | 0.0002 | 0.4633 | 0.4121 | 0.1780 | 0.0769 | 0.2894 | 0.1084 |
| | | 40000* | 0.0001 | 0.4697 | 0.4192 | 0.1775 | 0.0763 | 0.2894 | 0.1084 |
| | | 20000 | 0.0002 | 0.4814 | 0.4613 | 0.1929 | 0.0140 | 0.2905 | 0.1164 |
| | 3 | 30000 | 0.0002 | 0.4968 | 0.4712 | 0.1920 | 0.0131 | 0.2905 | 0.1168 |
| | | 40000* | 0.0001 | 0.5009 | 0.4743 | 0.1914 | 0.0126 | 0.2905 | 0.1164 |
| | | 20000 | 0.0002 | 0.5003 | 0.5026 | 0.1947 | 0.0007 | 0.3044 | 0.1171 |
| 3.5 | 30000 | 0.0002 | 0.5111 | 0.5101 | 0.1939 | 0.0006 | 0.3044 | 0.1171 | |
| | 40000* | 0.0001 | 0.5169 | 0.5137 | 0.1930 | 0.0006 | 0.3044 | 0.1172 | |

* The final case for analyses.

Chapter 7

7.1 Results and discussion.

Depending on the gap-to-diameters ratios, also the pitch distance (distance between the tandem cylinders) different type of flow regime can be gotten. Numerical simulations of flow around a single circular cylinder with gap-to-diameter ratio $G/D = (0.5; 0.8; 1)$ and $L/D = (2; 3; 3.5)$ have been performed. And the discussion will be focused on upper transition regime with high Reynolds number flows at $Re = 3.6 \times 10^6$ with $z_w = 1 \times 10^{-6}$ and $\delta/D = 0.5$. At the same time the numerical results will be affirmed by matching the present numerical results for $G/D = 1$ at $L/D = 2$ with both numerical results obtained by [29]. The present study comprises a discussion of the observed flow features connected to the creation of vortex shedding. The interplay between $G/D = 0.8$ and 0.5 at $L/D = 2; 3$ and 3.5

have previously not been mindfully investigated.

The numbers of C_D versus G/D and L/D at $Re = 3.6 \times 10^6$ with $z_w = 1 \times 10^{-6}$ and $\delta/D = 0.5$ are shown in figure 7.1.

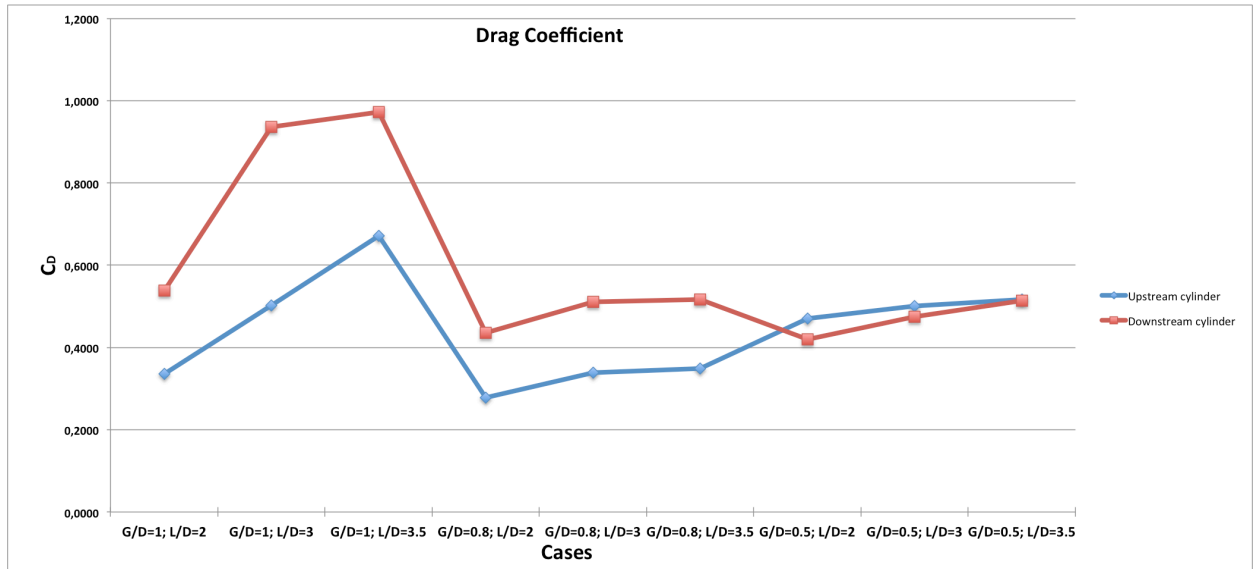


Figure 7.1 Time-averaged drag coefficients versus G/D and L/D

As seen in figure 7.1 the drag coefficient C_D increases as pitch distance L/D increase, as well with decreasing gap-to-diameter ratio the drag coefficient decreases. But with smaller gap-to-diameter ratios significant fluctuations of drag coefficients in comparing with $G/D = 1$ case have not observed. The downstream cylinder has a small coefficients values, in comparing with the upstream cylinder coefficients, however for gap-to-diameter ratio $G/D = 0.5$ the downstream cylinder given larger coefficients in comparing with the upstream cylinder. Due to the fact small distance between the plane wall and both cylinders and located the downstream cylinder in the vicinity of the upstream cylinder. These parameters created conditions for a worse drag force for upstream cylinder and positive drag force for the downstream cylinder, also, a value of gap-to-diameter ratio is equal to boundary layer thickness for this case, and during such conditions, most of the load

assumes the downstream cylinder. In contrast to the single cylinder case where with increasing gap-to-diameter ratio the drag coefficient increases too, here a different dependence are observed. About cases with $G/D = 1$, earlier published results from [29] shows a mild impact of the wall [29]. According to [29], the presence of the plane wall and decreasing of the gap-to-diameter ratio reduces the values of the mean flow parameters. This effect is obviously seen from the figure 7.1. In the present study, small pitch ratios are considered. In all three cases, the shear layer liberates from the upstream cylinder is awaited to attach to the downstream cylinder.

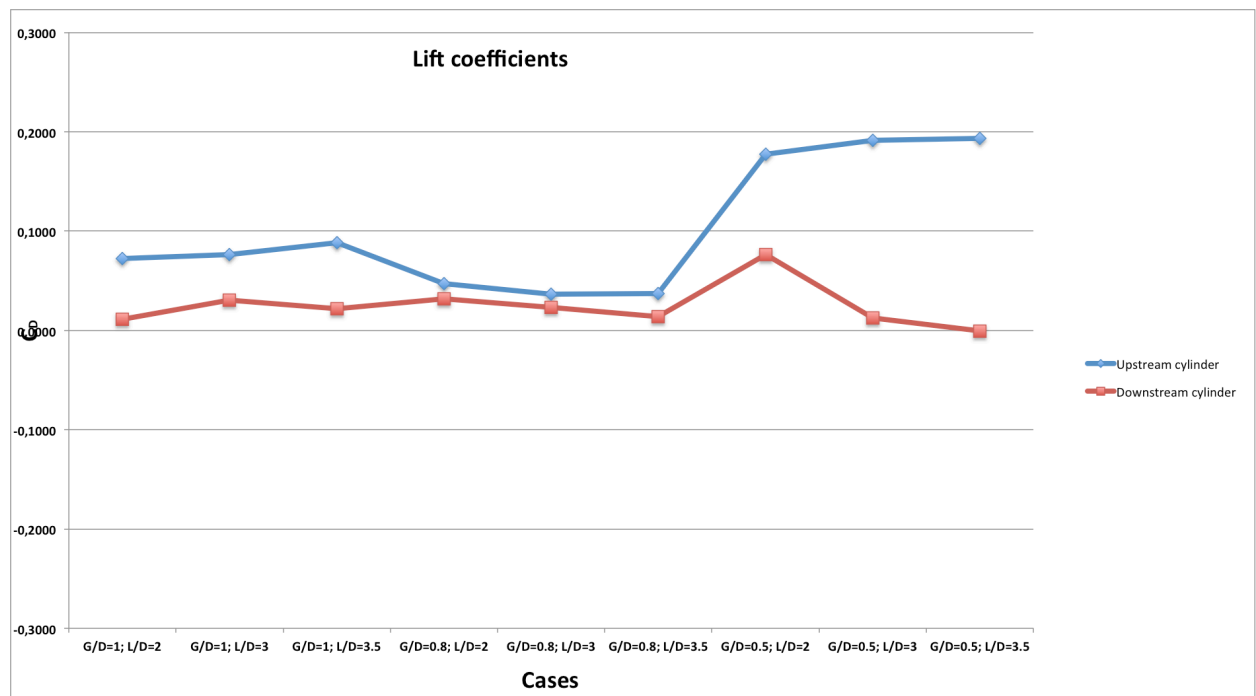


Figure 7.2 Time-averaged lift coefficients versus G/D and L/D

The lift coefficients C_L versus G/D at $Re = 3.6 \times 10^6$ with $\delta/D = 0.5$ are depicted on figure 7.2. Nearly all cases small values of lift coefficients for downstream were observed. It appears that only pitch distance affects on lift coefficient. In comparing cases by gap-to-diameter ratios, large fluctuations of lift coefficient have not been observed. But with changing pitch distance lift

coefficient changes too. The large C_L difference between the upstream and the downstream cylinders have been observed in $G/D = 0.5$ case only. This can be explained by the fact that with decreasing distance between the plane wall and the cylinder side, in this space large velocity region creates, hence the pressure decrease (see figure 7.6). And when pitch distance increases, lift coefficients difference increases it is explained by the fact that in a space between two cylinders vortex shedding occurs and affects on the lift force. Due to a high-velocity region as a consequence low-pressure region is formed in the smaller gap height in comparing with cases with a higher gap.

The Strouhal number versus depending on pitch and gap-to-diameter ratios at $Re = 3.6 \times 10^6$ with $z_w = 1 \times 10^{-6}$ and $\delta/D = 0.5$ are shown in figure 7.3. It appears that for $G/D = 1$ and 0.8 cases with increasing pitch distance the Strouhal number values for upstream cylinder increase, but for downstream cylinder decrease. This can be explained by the fact that both pitch distance $L/D = 2$ and 3 insufficient for the vortex shedding is developing from a free stage to a not-fully-developed stage as the influence of the bed is increasing. For $G/D = 0.5$ case situation is different; the Strouhal number increases slightly as pitch distance increases, proposing that vortex shedding is developing from a free stage to a not-fully-developed stage as the influence of the bed is growing.

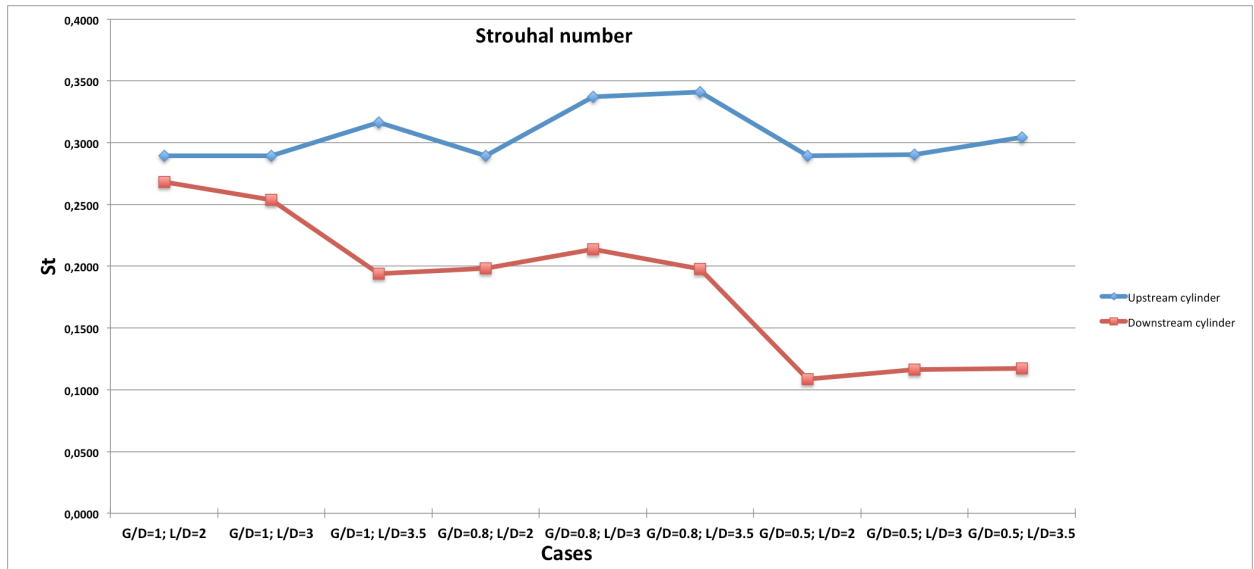


Figure 7.3 Time-averaged Strouhal numbers versus G/D and L/D

The pressure distribution ($C_p = \frac{p_c - p_\infty}{0.5\rho U_\infty^2}$) around cylinder body close to the plane wall with same values of Reynolds number, roughness and δ/D for various values of G/D and L/D are demonstrated on figures 7.4; 7.5 and 7.6. Where C_p is the pressure coefficient at the circumferential angle of the cylinder. The angle θ was measured by clockwise from the front point on a horizontal axis of the cylinder for lower shear layer only. As reported earlier the pressure change in the upper layer is not observed, therefore, for simplification, only the lower shear layer have been taken.

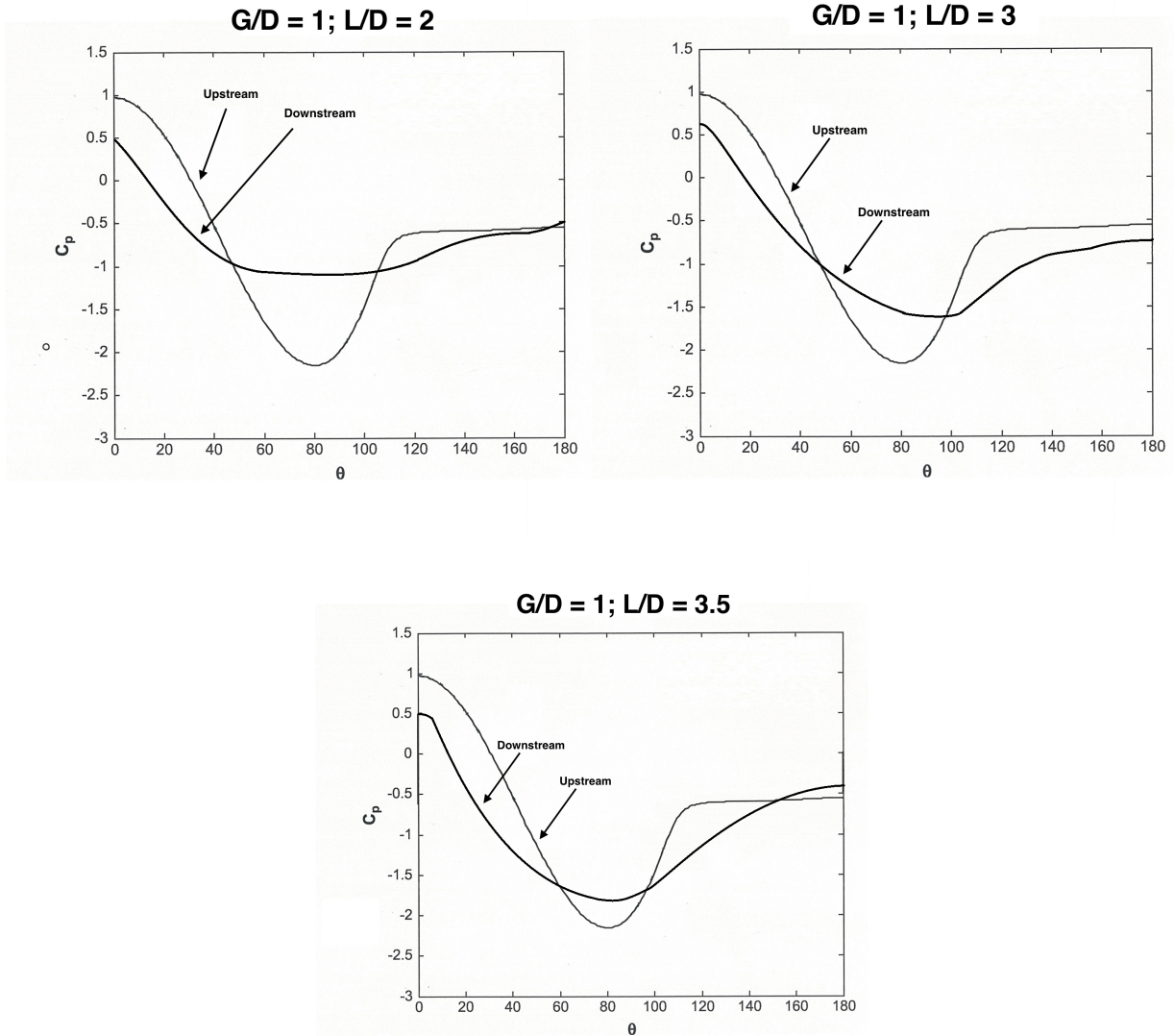


Figure 7.4 Mean pressure coefficients around the tandem cylinders at $G/D = 1$ for $Re = 3.6 \times 10^6$ with $z_w = 1 \times 10^{-6}$ and $\delta/D = 0.5$

At figures 7.4; 7.5 and 7.6 is shown that the sensitivity of the upstream cylinder drag to the peak region is more pronounced than that of the downstream cylinder, albeit some discretion is yclept for given the limited integration time. This instability can be interpreted as matching the heightened sensitive to a span-wise determination of the transition process and structural features in the shear layer separating from the upstream cylinder and the impact nascent from that place

on the flow around the area of that cylinder. A contributory factor may be a thin, quite weak, impact of the downstream cylinder on the upstream cylinder wake that demands a high level of solution.

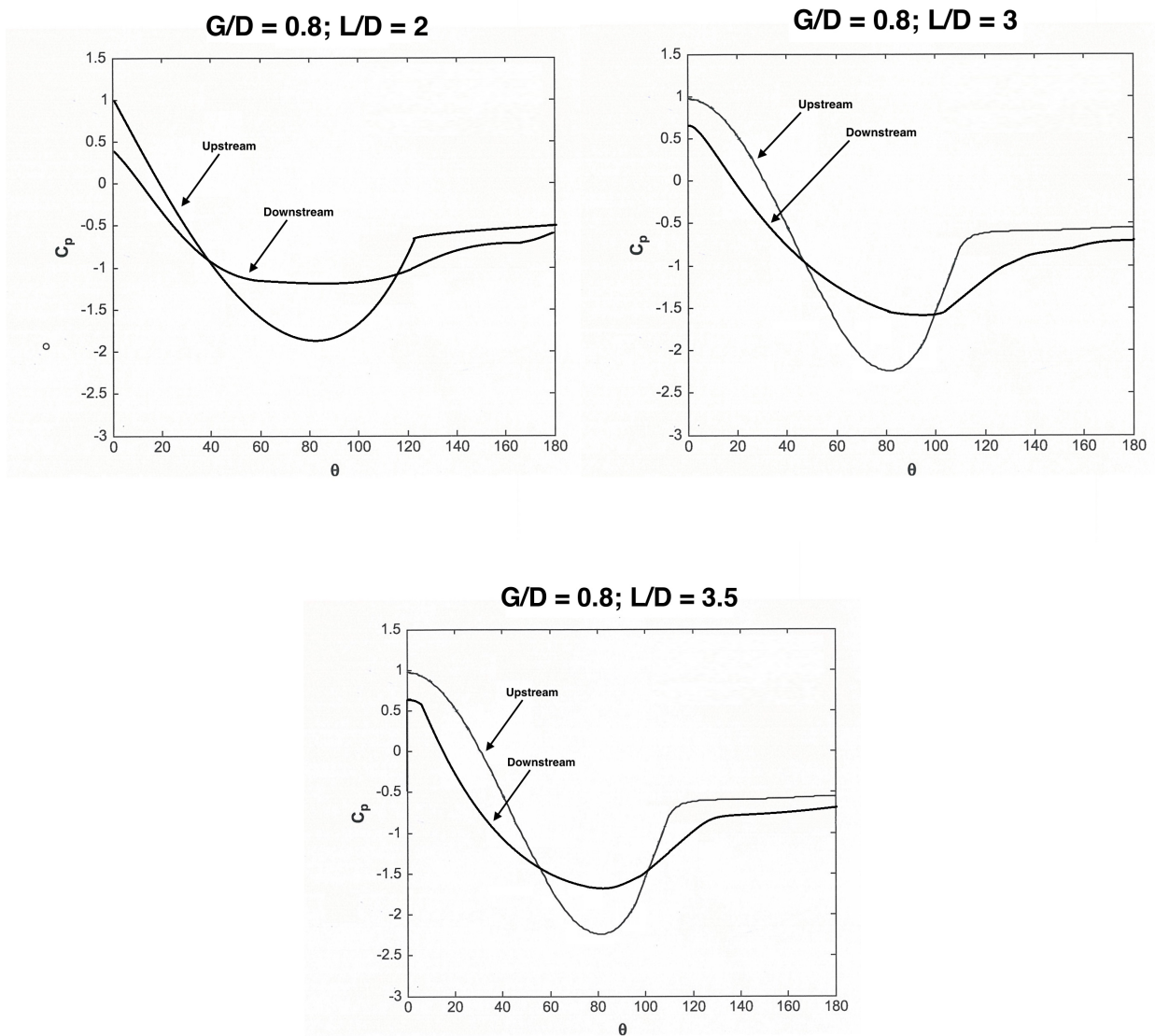


Figure 7.5 Mean pressure coefficients around the tandem cylinders at $G/D = 0.8$ for $Re = 3.6 \times 10^6$ with $z_w = 1 \times 10^{-6}$ and $\delta/D = 0.5$

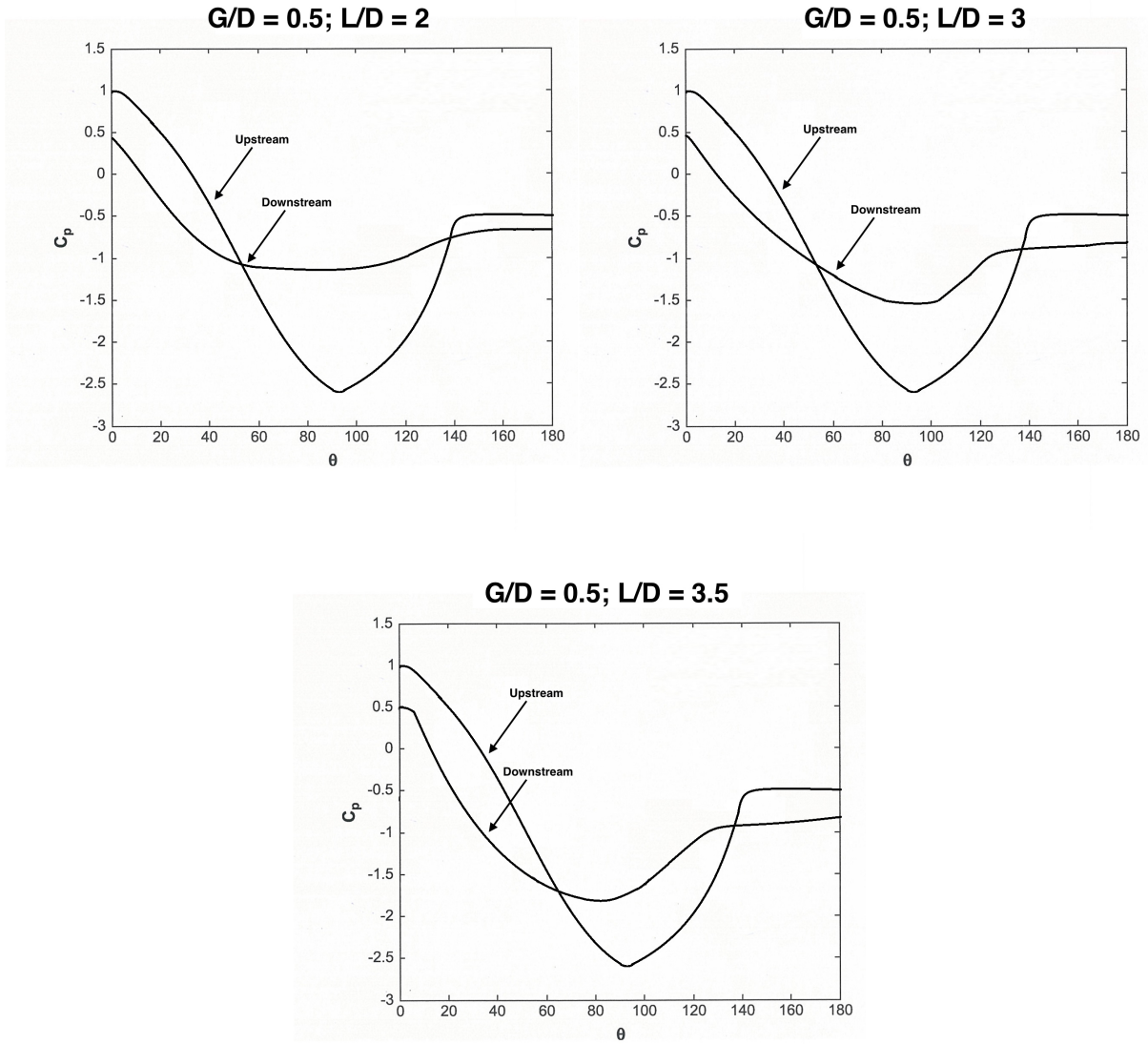


Figure 7.6. Mean pressure coefficients around the tandem cylinders at $G/D = 0.5$ for $Re = 3.6 \times 10^6$ with $z_w = 1 \times 10^{-6}$ and $\delta/D = 0.5$

7.2 Vorticity contours.

Figures 7.7, 7.8 and 7.9 show vorticity contours of flow around the tandem cylinders. All graphs have been obtained from numerical simulations by using Tecplot360, the gray scale is used to get visualizations of vorticity contours. An identical color code is applied to all graphs. The white areas designate the positive (anti-clockwise), while the black color designates the negative vorticity (clockwise). As seen from the figure 7.8 changing pitch distance changes a flow topology, the distance to where the first vortex is generated and the distance between the vertices. The pitch distance between cylinders is the main parameter influencing the vortex heights. As long as the pitch distance between the cylinders is unchanged, the character development vortex remains unchanged. With increasing the distance between the cylinders nature of the vortex formation is changing, for example, in Figure 7.8 can be compared processes appearance of vortices depending on the distance between of the cylinders. In the case at $G/D = 1$ distances between the cylinders to form a full development of vortices, therefore the flow of positive and negative zones go around the downstream cylinder and it begins the formation of vortices. These vortices are generated by the no-slip condition of the cylinder surface. The separated shear layer rolls up and fades out in the wake.

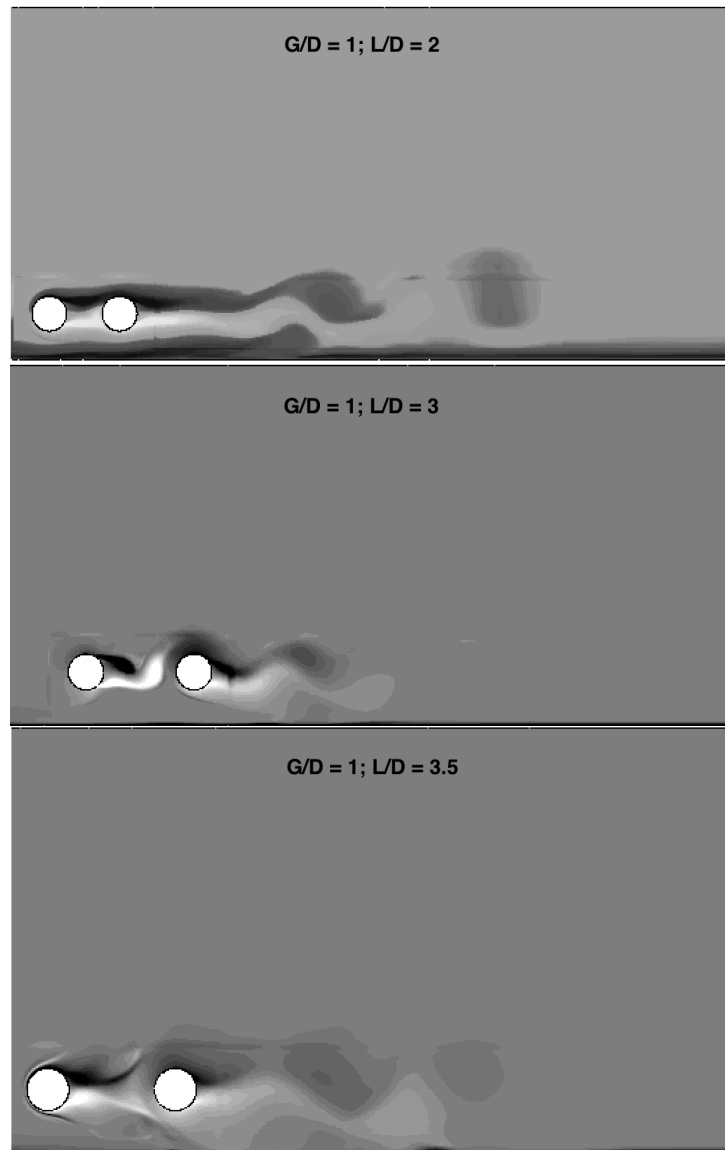


Figure 7.8. Instantaneous vorticity contours for $G/D = 1.5$ at $Re = 3.6 \times 10^6$ with $z_w = 1 \times 10^{-6}$ and $\delta/D = 0.5$

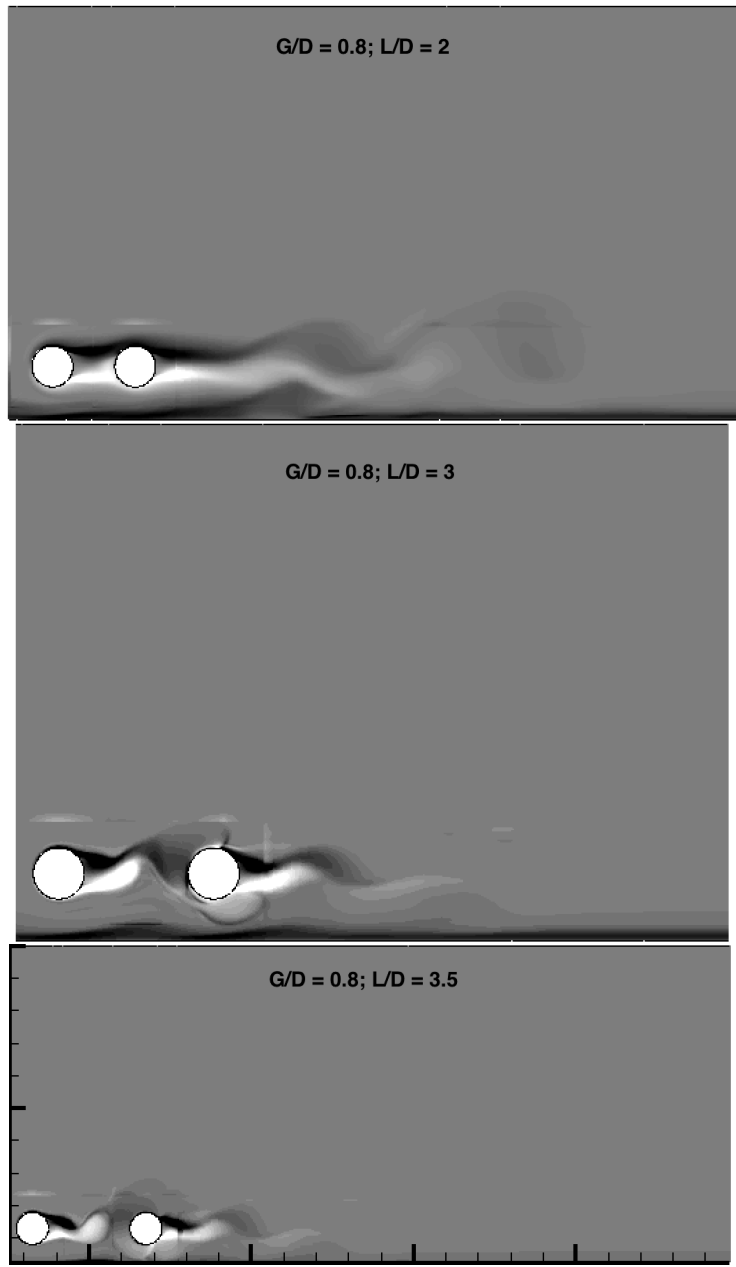


Figure 7.9. Instantaneous vorticity contours for $G/D = 0.8$ case at $Re = 3.6 \times 10^6$ with $z_w = 1 \times 10^{-6}$ and $\delta/D = 0.5$

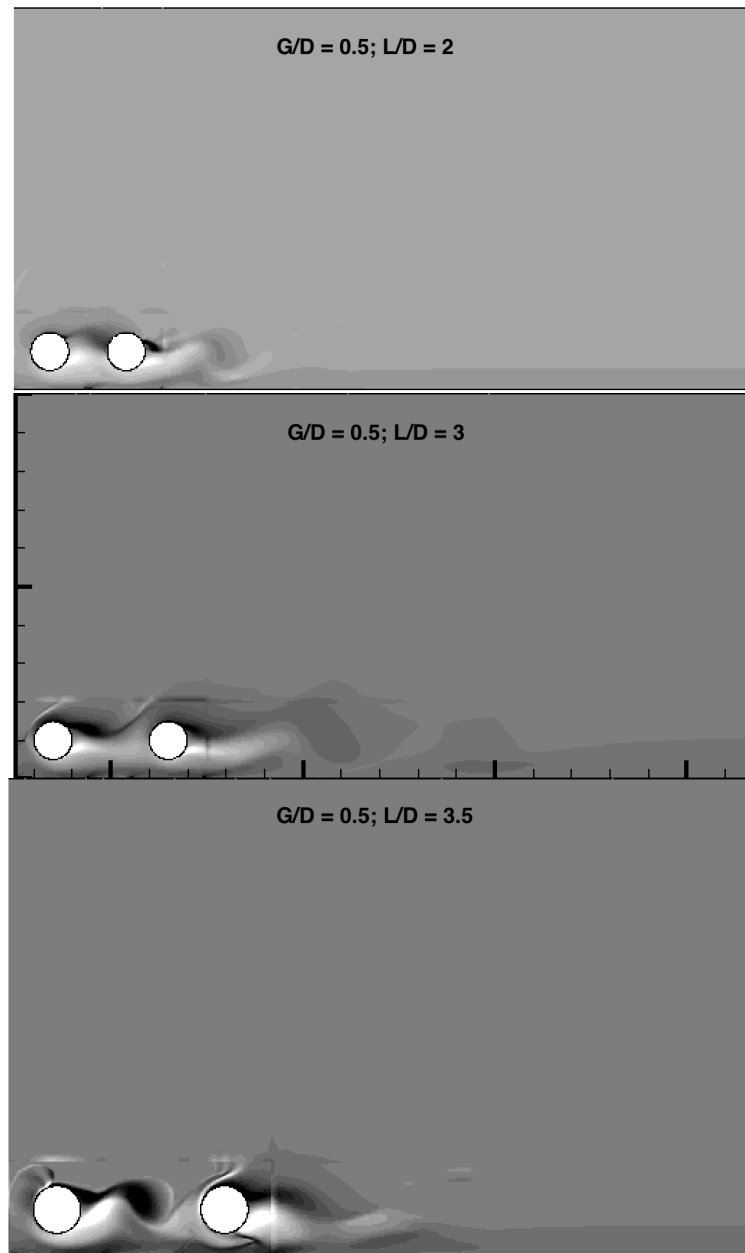


Figure 7.10. Instantaneous vorticity contours for $G/D = 0.5$ case at $Re = 3.6 \times 10^6$ with $z_w = 1 \times 10^{-6}$ and $\delta/D = 0.5$

For all pitch distance, the strongest vortex shedding's are observed at $L/D = 3$ and 3.5 , as that between cylinders so and past the downstream cylinder in both shear layers positive and negative. The vortex developing for the tandem cylinders with both gap-to-diameter ratios ($G/D = 1$ and 0.8) and pitch distances ($L/D = 2, 3$,

3.5) are close to identical. Also, the vortex shedding frequencies and the length of the vortex street are close to equal. The vortex streets of the $G/D = 0.5$ tandem cylinders are shorter of its neighboring pinch distances. Similarities to the vortex streets of the $G/D = 1$ and 0.5 cylinders are seen. But the difference is nevertheless there, it is caused by a small distance of the seabed and as a consequence of the flow from lower shear layer influence of vortices that are generated as a result of the flow from the lower shear layer and the plane wall.

7.6 Streamlines

The instantaneous streamlines depend on for $G/D = 1$ case is shown in a figure 7.11. For getting more information about streamlines see Chapter 4 (4.5 Streamlines). When considering small pitch ratios, the flow between the cylinders might become nearly stagnant [17] or governed by the quasi-static clearance eddies [30]. As mentioned earlier big flow characteristics difference between $G/D = 1$ and $G/D = 0.8$ cases have not been observed. If we observe downstream of the cylinder, we find that at the top leading edge of the cylinder, a small vortex is developed with larger vortices (flow asymmetry) in quasi-static clearance due to the presence of the wall. At $L/D = 3$ of the downstream cylinder, we can observe the impact of the plane wall. According to [17], development of symmetric wake and vortex shedding occur for both the extended body and reattachment regime behind the upstream cylinder. In our case, (see Figures 7.11 and 7.12) there are damped vortices at the bottom half of the downstream cylinder, and also there is not any existence of vortex shedding. At the downstream of cylinder, there is a separation of a wall boundary layer, which also displays the stronger influence of wall. The advancement of alternating vortex shedding and the wake flow behind

the upstream cylinder evolve due to large pitch ratio (L/D 3.5), which also display nearly symmetric time averaged wake (see Figure 7.13). Near to the area of the wall, wake flow is comparable to the one around a single cylinder and behind the leading cylinder. As we have discussed earlier, the existence of plane wall influence the vortices shed in the wake of the upstream cylinder, as well as incident flow on the downstream cylinder.

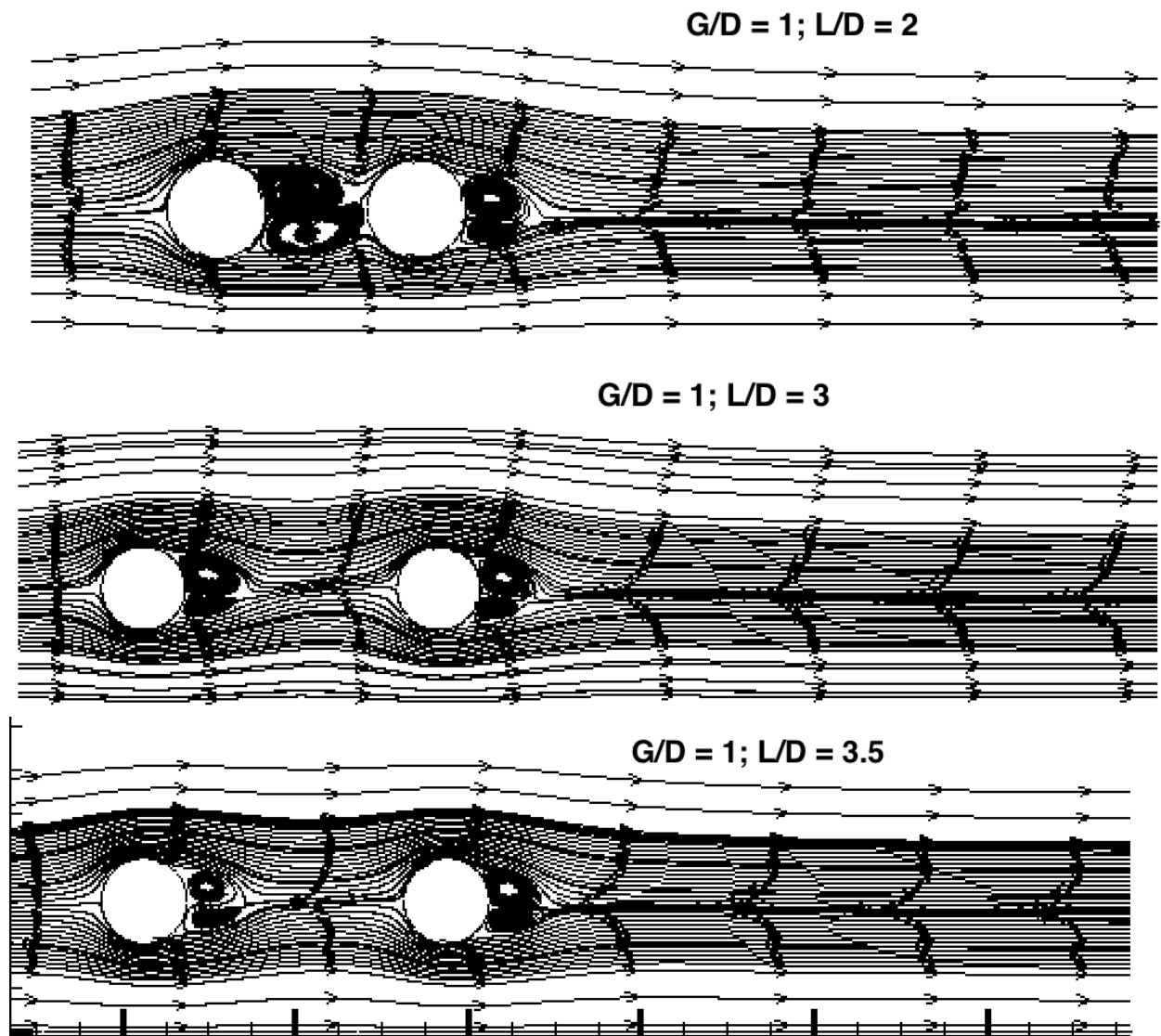


Figure 7.11. Instantaneous streamlines for $G/D = 1$ case at $Re = 3.6 \times 10^6$ with $z_w = 1 \times 10^{-6}$ and $\delta/D = 0.5$

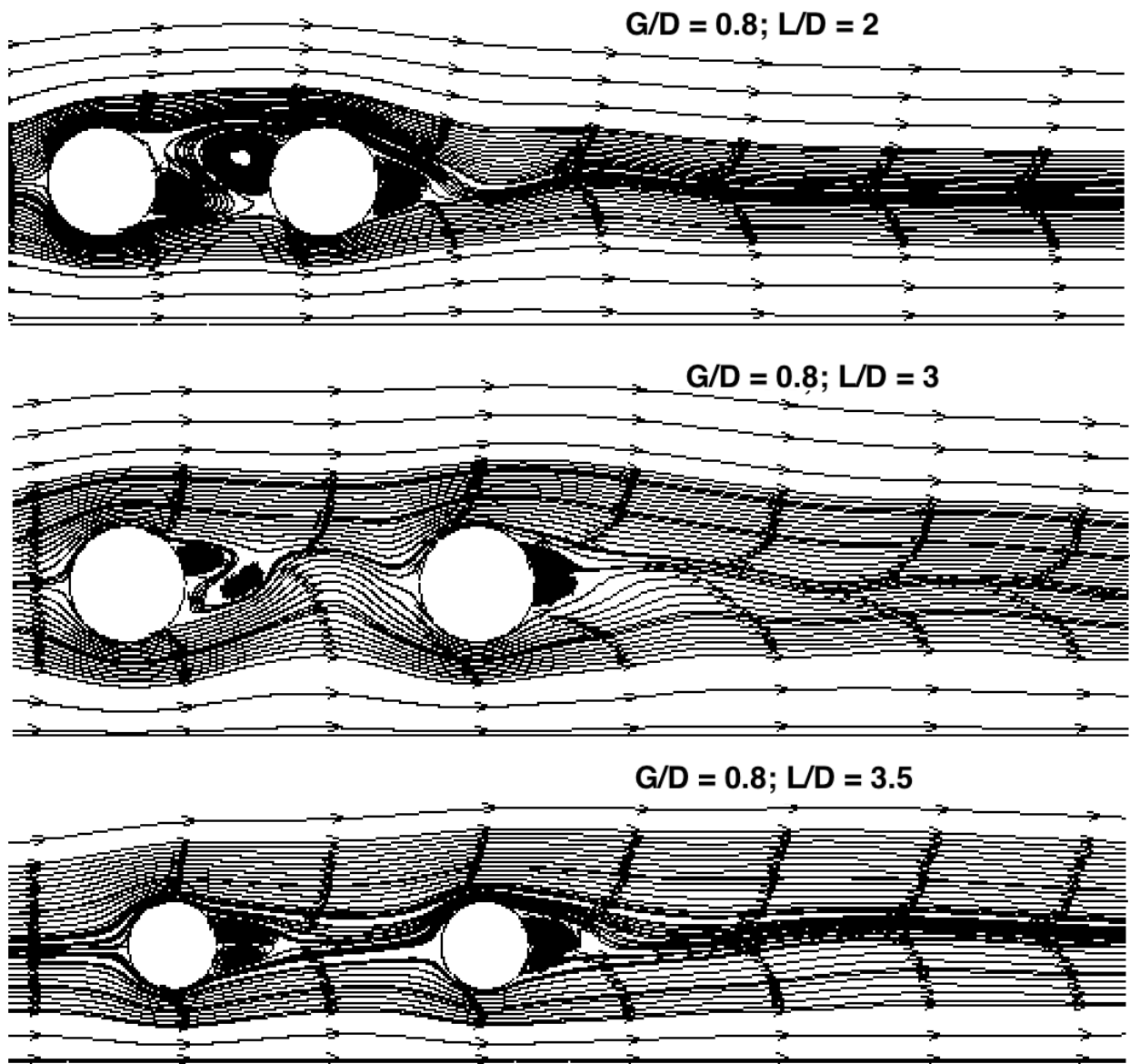


Figure 7.12. Instantaneous streamlines for $G/D = 0.8$ case at $Re = 3.6 \times 10^6$ with $z_w = 1 \times 10^{-6}$ and $\delta/D = 0.5$

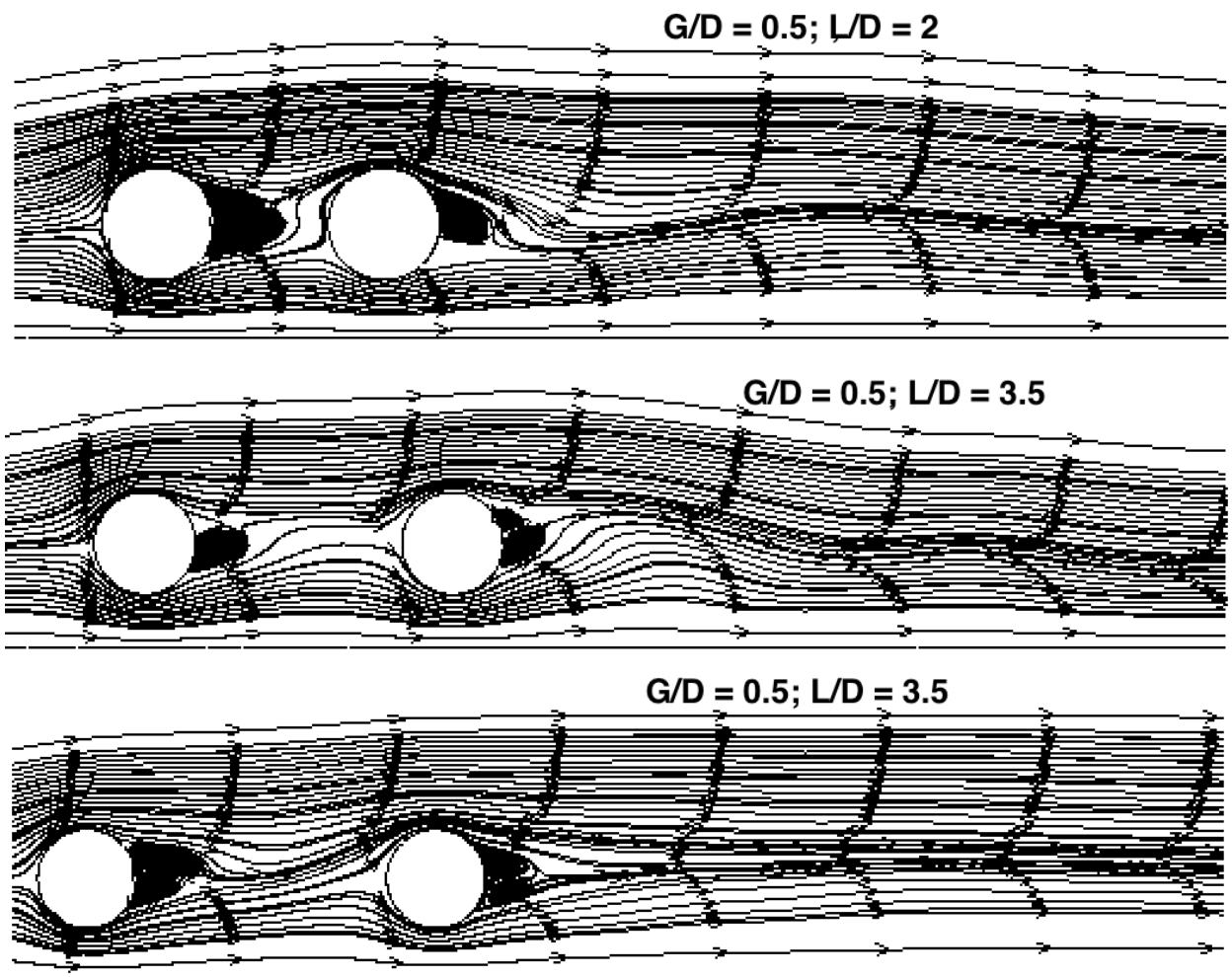


Figure 7.13. Instantaneous streamlines for $G/D = 0.5$ case at $Re = 3.6 \times 10^6$ with $z_w = 1 \times 10^{-6}$ and $\delta/D = 0.5$

Chapter 8

8.1 Conclusion for the tandem cylinders case

The flow around the tandem cylinders and located in the vicinity of the plane wall is calculated using RANS model. At $Re = 3.6 \times 10^6$ at $Re = 3.6 \times 10^6$ with $z_w = 1 \times 10^{-6}$ and $\delta/D = 0.5$, the influence of the gap-to-diameter ratio (influence of the plane wall) as well as distance between cylinders, are investigated. The drag and Lift coefficient are obtained for all cases and exerted from the second cylinder (downstream) on the mean parameters such as; drag and lift coefficients, Strouhal number and mean flow fields are considered. The main conclusions are as follows:

1. Similar to the single cylinder near to the wall case with cylinders in the tandem, at the same gap-to-diameter ratios have performed. It shows that, in the tandem arrangement, the downstream cylinder affected on the upstream and depending on the distance between cylinders main parameters increase for $G/D = 1$ and decrease for $G/D = 0.8$ and 0.5
2. The downstream cylinder affects the pressure distribution, small fluctuations for the upstream cylinder in all cases are observed. Besides, the pressure distributions are changed for downstream cylinder due to pitch distance changed. With increasing pitch distance, between two cylinders was more space to develop full vortices as a consequence pressure distribution for the downstream cylinder at $L/D = 3.5$ comparisons with upstream.
3. The flow in the wake of the tandem cylinders is turbulent. It is varying in the span-wise direction, especially at larger L/D . At the small distance between

cylinders ($G/D = 1$) is not sufficient space for full develop vortices and as a consequence full vortices development are observed past the downstream cylinder. For larger distance between cylinders ($L/D = 3$) the transition vortex formation is seen, and pitch distance $L/D = 3.5$ are sufficient to full develop vortices.

8.2 Recommendations for Further Work

The steady flow around tandem cylinders is a framework for other studies. The lack of published data for flows around tandem cylinders at $G/D = 0.8$ and $G/D = 0.5$ for pitch distance $L/D = 2; 3; 3.5$ with Reynolds number $Re = 3.6 \times 10^6$ with $z_w = 1 \times 10^{-6}$ and $\delta/D = 0.5$ have made it difficult to perform a detailed validation of the numerical model. It would be much easier to analyze this work with measurement results from laboratory experiments or other numerical results under the same boundary conditions.

As for the further work, it would be interesting to do numerical simulations using same configurations for different turbulence models, such as LES, URANS, DES and k- ω . It would also interest to estimate and investigate by the analysis of the same configuration for both, single cylinder and tandem cylinders, in 3D domain. The next step will be, by the obtained numerical results, such as the pressure and the velocity distributions, vortices formation; soil erosion below the tandem cylinders can be investigated.

In the present study values of gap-to-diameter for both single cylinder and tandem cylinders, $G/D = 0.5; 0.8; 1$ were taken as well as pitch distance $L/D = 2; 3;$

3.5 for tandem cylinders were taken only. As for the further work it would be interesting to get analysis for smaller gap-to-diameter ratios in both single and tandem cases, such as $G/D < 0.5$, and larger pitch distance in tandem case, such as $L/D > 3.5$.

References

- [1] Summer B.M. and Fredsøe, J (2006). *“Hydrodynamics Around Cylindrical Structures”*, Advanced Series on Ocean Engineering, Revised Ed, World Scientific Publishing
- [2] Summer, M. and Fredsøe, J. (1997). *“Hydrodynamics around circular cylinders”*, volume 12. World Scientific Publishing Co. Pte. Ltd.
- [3] Zdravkovich M. M.(2003), *“Flow Around Circular Cylinders”*, Vol 2: Applications. Oxford University Press Inc,
- [4] Ljungkrona L., Norberg C., and Sundén, B. (1991). *“Free-stream turbulence and tube spacing effects on surface pressure fluctuations for two tubes in an in-line.”*
- [5] Igarashi, T. (1981). *“Characteristics of the flow around two circular cylinders arranged in tandem: 1st report”*
- [6] Hori, E. (1959). *“Experiments on flow around a pair of parallel circular cylinders. Proc. 9th Japan Nat. Congress Appl. Mech”*
- [7] OpenFOAM Ltd. (2014), ‘OpenFOAM User Guide’. (Accessed 10 June 2014). URL: <http://www.openfoam.org/docs/user/>
- [8] Ferziger, J. & Perić, M. (2002), *“Computational Methods for Fluid Dynamics, 3th edition edn, Springer Berlin.”*
- [9] Schlichting, H. & Gersten, K. (2000), *“Boundary Layer Theory, 8th edition edn, Springer Berlin Heidelberg”*
- [10] Launder, B. & Sharma, B. (1974), *“Application of the energy-dissipation model of turbulence to the calculation of flow near a spinning disc, Letters in Heat and Mass Transfer”*
- [11] Yunus A. Çengel, John M. Cimbala (2010), *“Fundamentals and applications third edition. 2010”*
- [12] Sarkar S. and Sarkar S. (2010)*“Vortex dynamics of a cylinder wake in proximity*

- to a wall. Journal of Fluids and Structures” (2010).*
- [13] Yunus A. Çengel, John M. Cimbala (2010), “*Fundamentals and applications third edition. 2010*”
- [14] Ong, M.C. (2010) “*Numerical simulation of flow around a circular cylinder close to a flat seabed at high Reynolds number using a κ - ϵ model*”
- [15] Taniguchi S. and Miyakoshi K., “*Fluctuating fluid forces acting on a circular cylinder and interference with a plane wall*”, Experiments in Fluids, vol. 9, pp. 197–204, 1990.
- [16] Price S. J., Sumner D., Smith J. G., Leong K., and Paidoussis M. P. (2002), “*Flow visualization around a circular cylinder near to a plane wall*”, Journal of Fluids and Structures, vol. 16, pp. 175–191, 2002.
- [17] Zdravkovich, M.M. (1985) “*Forces on a circular cylinder near a plane wall*”, Applied Ocean Research, vol. 7, pp. 197–201, 1985.
- [18] Zdravkovich, M. M. (1997). “*Flow around circular cylinders: fundamentals*”, volume 1. Oxford University Press, United States.
- [19] Frei, W. (2013). “Which turbulence model should I choose for my CFD application?” Retrieved 2015-02-19, from <http://www.comsol.com/blogs/which-turbulence-model-should-choose-cfd-application/>
- [20] Versteeg, H. & Malalasekera, W. (2007), “*An Introduction to Computational Fluid Dynamics: The Finite Volume Method (2nd Edition)*”, Prentice Hall.
- [21] Ong, M.C. (2009) “*Applications of a Standard High Reynolds Number κ - ϵ model and A Stochastic Scour Prediction Model for Marine Structure*”. Doctoral thesis at Norwegian Technical NU.
- [22] Majumdar S. and Rodi W. (1985). “*Numerical calculation of turbulent flow past circular cylinder.*” 7th Turbulent Shear Flow Symposium, Stanford, USA

- [23] Utnes T. (2008). "A segregated implicit pressure projection method for incompressible flows." *Journal of Computational Physics*.
- [24] Cengel, Y. A. and Cimbala, J. M. (2010). "Fluid Mechanics - Fundamentals and Applications. McGraw-Hill, 2nd edition."
- [25] Bakker, A. (2006), "Lecture 7 - Meshing, lecture notes distributed in Computational Fluid Dynamics (ENGS 150)" at Dartmouth College, accessed 10 June 2014, <http://www.bakker.org/dartmouth06/engs150/07-mesh.pdf>.
- [26] Utnes T. (2008). "A segregated implicit pressure projection method for incompressible flows." *Journal of Computational Physics*.
- [27] Rodi W. (1993). "Turbulence models and their application in hydraulics.". Rotterdam, Netherlands.
- [28] Zdravkovich, M. M. (2003). "Flow around circular cylinders: Applications", volume 2. Oxford university press, New York.
- [29] Mia Abrahamsen Prsic, Ong M.C., Bjørnar Pettersen and Dag Myrhaug (2015). "Large Eddy Simulations of Flow Around Tandem Cylinders Close to a Horizontal Wall" *International Journal of Offshore and Polar Engineering*.
- [30] Lin J.C., Yang Y. and Rockwell D. (2002). "Flow past two cylinders in tandem: Instantaneous and average flow structure." *J Fluids Struct*, 16(8), 1059-1071.